Experimental and numerical Investigation of the continuous Glass Fiber Drawing Process

Quentin CHOUFFART

Department of Aerospace and Mechanical Engineering

University of Liège

A thesis submitted for the degree of

Doctor of Philosophy

February 2018

Members of the Examination Committee

HEINRICHS, Benoît - **President** - Professor at the University of Liège

TERRAPON, Vincent E. - **PhD Advisor** - Professor at the University of Liège

PONTHOT, Jean-philippe - Professor at the University of Liège

GILET, Tristan - Professor at the University of Liège

NOELS, Ludovic - Professor at the University of Liège

SCHEID, Benoit - Research associate FNRS at the Free University of Brussels

CONRADT, Reinhard - Emeritus professor of the RWTH University of Aachen and president of the German Society of Glass Technology.

WAUCQUEZ, Christophe - 3B-The Fibreglass company

Abstract

The manufacturing process of continuous glass fibers used for the reinforcement of composite materials consists in drawing and quickly cooling free jets of molten glass into fibers using a winder. Despite a long practical experience in producing glass fibers, the process is still not fully optimized. The main challenge stems from the high sensitivity of the process to numerous disturbances that can cause the fibers to break during their drawing. These frequent breaks lead to a significant loss of raw material, higher energy consumption and reduced production throughput. Nonetheless, devising new strategies for improving the overall process efficiency requires a detailed knowledge of the phenomena involved. The underlying physics is complex, including fluid and solid mechanics, heat transfer, rheology, chemistry, material science, fracture mechanics, explaining why it is still poorly understood.

The overall goal of this thesis is thus to better understand the underlying physics, which can be then leveraged for improving the fiber drawing process. In particular, the main objectives are *i)* to extend the current understanding of the physics involved in the glass fiber drawing process and the fiber break, *ii)* to provide a physical model for the drawing of a single fiber that includes all relevant physics, *iii)* to leverage numerical solutions of this model to suggest strategies for improving the process, and *iv)* to derive a probabilistic model of the break rate that uses inputs from the physical model. As the problem is extremely complex, the scope of this thesis is restricted to a single fiber and to the "liquid" region between the bushing plate and glass transition.

The methodology relies on a combined theoretical, computational and experimental approach. On the experimental side, a test facility has been built to investigate the drawing of a single fiber. Although the process conditions slightly differ from those in production, measurements of several macroscopic quantities provide useful data for the validation of the numerical models. Additionally, statistics of several fiber break tests are gathered to calibrate the break rate model. From the theoretical and numerical point of view, a two-dimensional axisymmetric model for the liquid region of a single fiber has been developed, which accounts for all relevant physics. Additionally, a simplified one-dimensional model has been derived. As this model leads to a semi-analytical solution, it is computationally less expensive and provides a very useful tool to better understand the link between several global parameters. The influence of the different physical contributions, key parameters and

material properties are extensively analyzed through sensitivity analysis. A particular emphasis is placed on heat transfer, including internal radiation and cooling by the surrounding air flow. Then, these physical models are used to characterize the process operating window by focusing on a key performance indicator, the axial stress. The impact of the production parameters, glass composition, design of the bushing,... are thus investigated. Furthermore, the unsteady behavior of the process is analyzed in order to determine the critical parameter values that lead to instability. Although the approach does not rely on a formal linear stability analysis, it provides a first estimation of the stability limit of the process and highlights the key trends. Finally, a first attempt at modeling the break rate is presented. This break rate model is based on a weakest-link assumption. It relates the stress computed from the physical models to a probabilistic description of the strength, that is assumed to follow a Weibull distribution. As this model needs to be calibrated, an experimental measurement strategy is developed and discussed.

This work confirms several results from the literature and provides new insight. It is shown that heat transfer is the most important factor that determines the final axial stress in the fiber. In particular, a faster cooling in the initial region close to the tip, where heat transfer is dominated by radiation, increases the stress. Moreover, it is found that the main effect of internal radiation is to increase the heat flux through the fiber surface, increasing thus the cooling rate. As internal radiation is extremely complex to model and implement, a simpler approach is to consider the fiber as an opaque medium and to represent the increased cooling by internal radiation through an effective emissivity. Regarding the convective cooling, it is demonstrated that the empirical correlation for the convective heat transfer coefficient that is widely used in the literature is not accurate. A new correlation specific to the glass fiber drawing process or a detailed representation of the surrounding air flow is required to predict more accurately heat transfer by convection. In terms of process optimization, the physical models indicate that, for a given target fiber radius, the final axial stress can be reduced by increasing the tip temperature. This can be achieved either by increasing the drawing velocity, which leads to a higher flow rate, or by reducing the tip radius to maintain the flow rate constant. Nonetheless, this strategy is limited by the drawing instability that occurs at high tip temperature. On the other hand, the stress can be reduce by playing on the glass composition. In particular, a lower surface tension decreases the stress and limits the occurrence of this instability. For multi-filament bush-

ing, another strategy is to ensure a bushing temperature as homogeneous as possible, as temperature inhomogeneity can lead to large variations in stress across fibers. Finally, experimental results of break tests confirm that the fiber strength, at constant process conditions, follows a Weibull distribution. However, they also demonstrate that the strength depends on the process conditions. In particular, the strength seems to increase when the stress increases. This suggests that minimizing the stress might not be the best strategy for reducing the break rate.

These results represent important new insight into the continuous fiber drawing process and its related physics. They also provide a useful basis for devising new process optimization strategies. Nevertheless, many questions remain open and much work is still required.

Acknowledgements

I would like to thank my advisor, Professor V. E. Terrapon, for his precious support, the quality of his advice and his availability during this work. I wish to express my deep gratitude to 3B-the fibreglass company and to the Walloon region which have funded and supported this thesis. In particular, P. Simon and D. Laurent deserve my special thanks for their support, time and encouragement during all these years. I am also grateful to the R&D team of 3B for the enthusiastic and motivating work environment. A special thank to S. Klenkerbeg, L. Charlier, F. Wey, and F. Van Hoof for their technical support.

I also thank Professor Y. Jaluria for having hosted me in his research group at the university of Rutgers and for his technical help in modeling radiation.

I am also grateful to the professors B. Heinrichs, J.P. Ponthot, T. Gilet, L. Noels, B. Scheid, R. Conradt and C. Waucquez for agreeing to serve on my PhD the committee. Finally, I would like to specially thank A. Guissart and V. Kempenaer for their encouragements, my family, and all of my friends for their patience.

Contents

Chapter 1

Introduction

This thesis investigates both numerically and experimentally the manufacturing process of continuous glass fibers that are used for reinforcement of composite materials. The overall objective is to better understand the underlying physics of the glass fiber drawing process, and to identify and quantify the key global parameters that control the final characteristics of the fibers. This knowledge is then used to better understand the root causes of fiber breaking that is repeatedly observed in production and strongly limits the efficiency of the manufacturing process. The long-term goal is to devise new optimization strategies to increase production while reducing the break rates. Note that this research has been conducted in close collaboration with 3B-the fiberglass company, which has provided financial, scientific and logistic support.

The present chapter first describes the context and general scope of this study. In particular, the overall manufacturing process of glass fibers and the problem of fiber breaks are described. The second section provides a brief review of the literature and highlights the current limitations of the state-of-the-art. It is followed by the description of the objectives of the thesis and general methodology used to achieve them. Finally, the overall structure of the thesis is presented, including its main contributions.

1.1 Context and scope

Glass fibers can be divided into three main categories according to their end application. Their respective characteristics, and, thus, their corresponding manufacturing process significantly differ:

- *Glass wool* is used for insulation. It corresponds to an agglomeration of non-continuous fibers whose diameter is about 5 μm. The fibers are produced with a rotating spinneret, from which the glass melt is continuously ejected through small

orifices by centrifugal force. The melt is then transformed into non-continuous fibers with an air jet.

- *Optical fibers* are used for signal transmission in telecommunication. Their diameter is much larger (~ 300 μm). Additionally, their core is made out of glass whose composition differs from that used for their envelope in order to obtain the required optical properties. The manufacturing process consists in continuously and simultaneously drawing the two melts with a winder in a thermally controlled environment.

- *Glass fibers* for material reinforcement are used in composite materials, similarly to carbon fibers. Although fiberglass has slightly lower mechanical properties than carbon fibers, it is less expensive to produce, explaining its widespread use. In this case, glass fibers have a diameter typically varying between 10 and 30 μm. The manufacturing process consists in continuously drawing the melt into thousand parallel fibers that are quickly cooled down.

This thesis focuses solely on the third category, i.e., glass fibers for material reinforcement, and the corresponding fiber drawing process. The following sections provide an overview on the typical glass composition, the final form of the fibers and the manufacturing process.

1.1.1 Continuous glass fibers for reinforced materials

Since the late 1940s composites have seen a rapid and continuous growth driven by the demand for materials with improved mechanical properties. Some of the key properties of fiberglass include high strength-to-weight ratio, resistance to corrosion, resistance to fatigue, resistance at high temperature, and many others. In 2017, the largest groups on the worldwide global glass fiber market are Owens Corning and Jushi with 18% of total production, NEG with 12%, CTG and CPIC with 8%, while 3B the fibreglass company represents 3% of the total market[1]. Fiberglass is found in a very large range of applications and in many sectors, such as automotive, transportation, civil engineering, electrical engineering, wind energy, aerospace, etc.

1.1.2 Typical glass composition

The choice of glass composition is not only driven by the required properties of glass fibers, but also by economical, environmental, regulatory and manufacturability constraints. Several families of glass composition are typically used in fiberglass. They

[1]These figures are estimated from the marketing management team at 3B-the fiberglass company [1].

are denoted by a letter, such as for instance E, A, S. Each family is related to a specific property or application (e.g., corrosion, high modulus, dielectric properties). E-glass, originally developed for electrical applications, is the most widespread commercial glass composition. Its major constituents are SiO_2 (52-56%), Al_2O_3 (12-16%), B_2O_3 (5-10%), CaO (16-25%), MgO (0-5%), Fe_2O_3 (0-0.8%), B_2O_2 (0-10%), and additional small quantities of other oxides [2]. E-CR glass is a specific composition in which B_2O_2 is absent (often for cost or environmental reasons). Other families, such as S-Glass (high strength), A-Glass (high alkaline content) or D-Glass (improved dielectric properties) have better properties, but are more difficult to produce and are thus more expensive. They are typically used in the high-added-value market (for military or aeronautic applications for example) [2]. This thesis mostly focuses on a commercial E-CR glass called Advantex© that has been developed by Owens Corning and is currently commercialized by Owens Corning and 3B-the fiberglass company.

1.1.3 Types of E-CR glass products

The glass fibers can have different forms (see Fig. 1.1) and sizes (i.e., fiber diameter) depending on the application and customer requirements:

- Direct roving (DR): the fibers are *continuously* wound around a spool. Their diameter generally ranges between 17 and 24 μm, but can be as low as 10 μm. A typical application is that of wind turbine blades.

- Chopped strands (CS): the fibers are *chopped* just after the winder into strands with a length of a few millimeters. Their diameter usually varies between 10 and 13 μm. Applications are mainly found in the automotive industry.

- Continuous filament mat (CFM): the fibers are deposited spirally to form a mat. Their diameter is around $17 - 24$ μm. The main application is that of boat hulls.

The manufacturing process is slightly different depending on the final form of the glass fibers. Consequently, the corresponding challenges and main manufacturing limitations also differ. For instance, the manufacturing of DR and CFM is more sensitive to the winding issues, while the production of CS is more impacted by drawing limitations. This thesis focuses mostly on the manufacturing process of fibers for chopped strand products, but many results also apply to those for direct roving and continuous filament mat products.

Figure 1.1: Typical glass fiber products that are used for material reinforcement [1].

1.1.4 Description of the manufacturing process

The overall manufacturing process of continuous glass fibers is depicted in Fig.1.2. It consists in the continuous mixing of the raw materials that are then melted in a furnace. The molten glass then flows through channels to the forehearth and the different bushing positions, where it is continuously drawn and rapidly cooled into several thousands fibers.

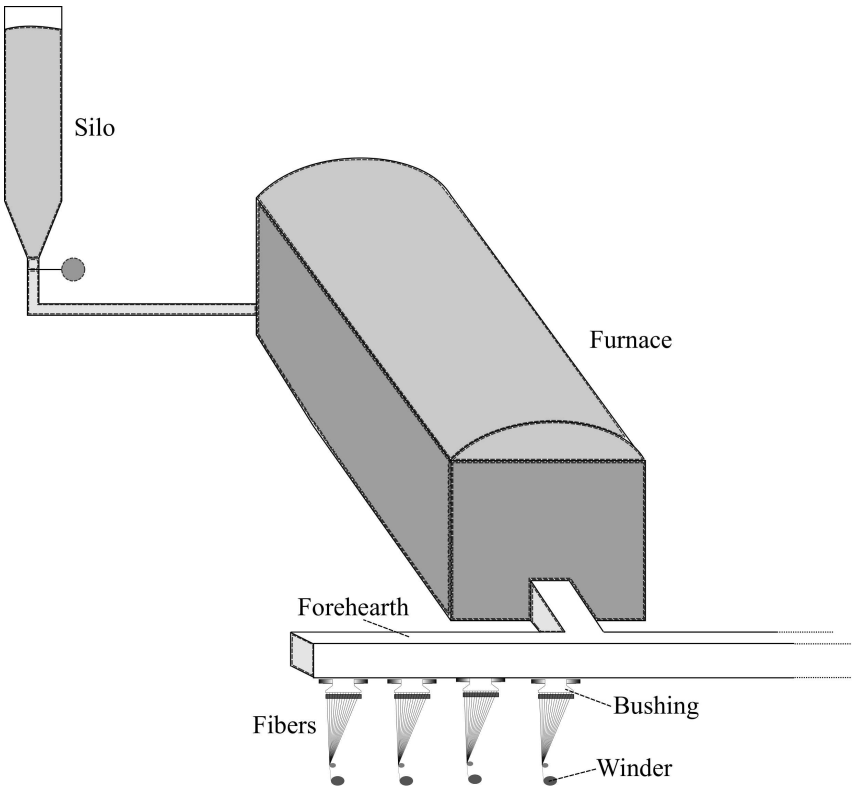

Figure 1.2: Schematic of the continuous manufacturing process of glass fibers.

Mixing and melting process

The first step corresponds to mixing in the right proportion the different raw constituents that are stored in large silos in a powder form. The resulting batch is then continuously injected at its rear of a furnace, in which it is melted into liquid glass. A schematic of the cross-section of a furnace is shown in Fig. 1.3. At the rear the injected raw material forms a layer floating above the molten glass, which is called the batch blanket. The high glass temperature, up to 1400°C, is achieved through burners installed in the furnace crown above the melt and through electrical heaters within the glass bath itself. The raw material must be melted for a sufficiently long time to ensure homogenization: it takes on average a full day for the raw material to go through and leave the furnace. Homogenization is further promoted by creating convection flows in the bath. This is typically accomplished with bubblers that inject large air bubbles in the melt. The homogenized melt then passes the throat and flows through channels to the forehearths (or frontend). The melt temperature in the channels is maintained by small burners above the liquid free surface. At the different forehearths the molten glass is then delivered to the bushing positions just below.

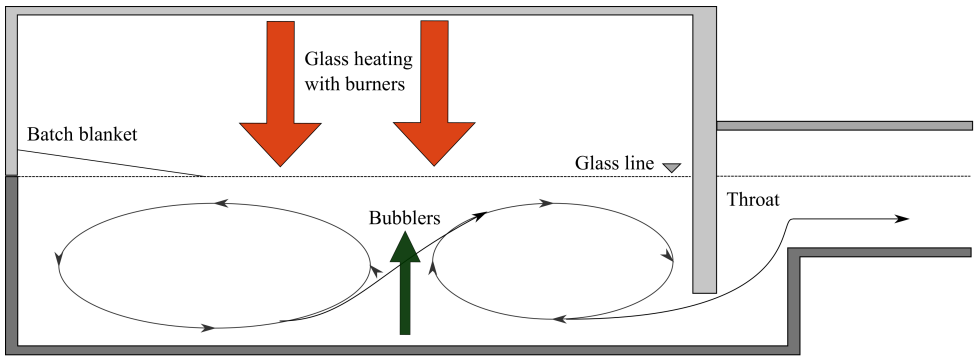

Figure 1.3: Schematic view of a longitudinal cross-section of a furnace.

Fiberization process

At the bushing position the molten glass is divided into thousands of free jets that are quickly cooled and continuously drawn into fibers by a winder (Fig. 1.4). The individual fibers form when the melt flows through the bushing, i.e., a metal container with thousand orifices on its lower surface. These holes are tube-shaped with an internal diameter of about 1-2 mm, and are thereafter referred to as tip. A bushing before its installation in the production line is shown in Fig. 1.5. The number of tips, and thus of fibers, can reach up to 6000-8000 per position. The bushing is made out of a platinum-rhodium alloy to withstand the high temperatures and avoid the erosion caused by the glass flow.

Additionally, this material can be electrically heated to precisely regulate the global glass temperature. Electrical power is provided through clamps at the bushing ears (i.e., the small curved plates at the end of the busing in Fig. 1.5). The target bushing temperature, about 1350°C for the glass considered here, is controlled through a thermocouple on the side at mid-height of the bushing.

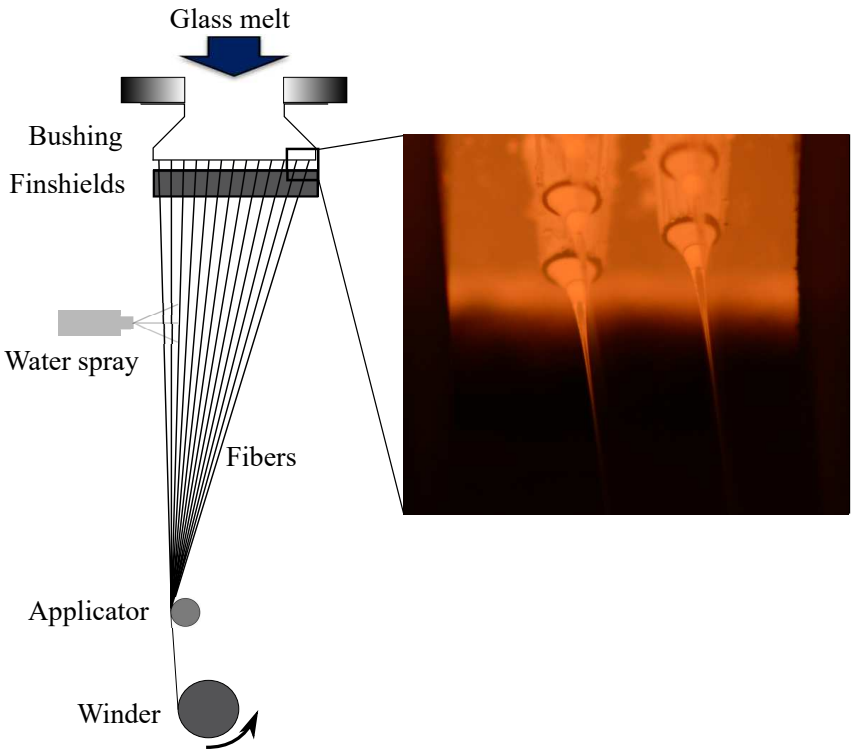

Figure 1.4: Overall schematic view of a bushing position (left) and detailed view of four tips and the corresponding forming fibers (right).

After exiting the tip the molten glass is quickly cooled to reach the glass transition and drawn at high velocity by the winder. The rapid acceleration of the melt induces strong radius attenuation, as illustrated by the cone shape of the glass just below the tip (see right part of Fig. 1.4). The cooling of the glass is initially mostly achieved by radiation, before convection takes over further away from the tip. As discussed later, the cooling history plays a key role in the process. Moreover, the tip temperature must be maintained in a very precise range to achieve the adequate glass viscosity. In order to partially control the radiative heat transfer, water-cooled copper blades, called finshields and shown in Fig. 1.6, are inserted horizontally between rows of fibers a few millimeters below the bushing plate (see Fig. 1.5). The position of the finshield blades is clearly indicated by the space between two rows of tips in Fig. 1.7. During production the finshields can be moved vertically to modify the radiative cooling of the fibers and the heat pattern of the bushing plate, although the exact mechanism is still not well understood. Finshields are

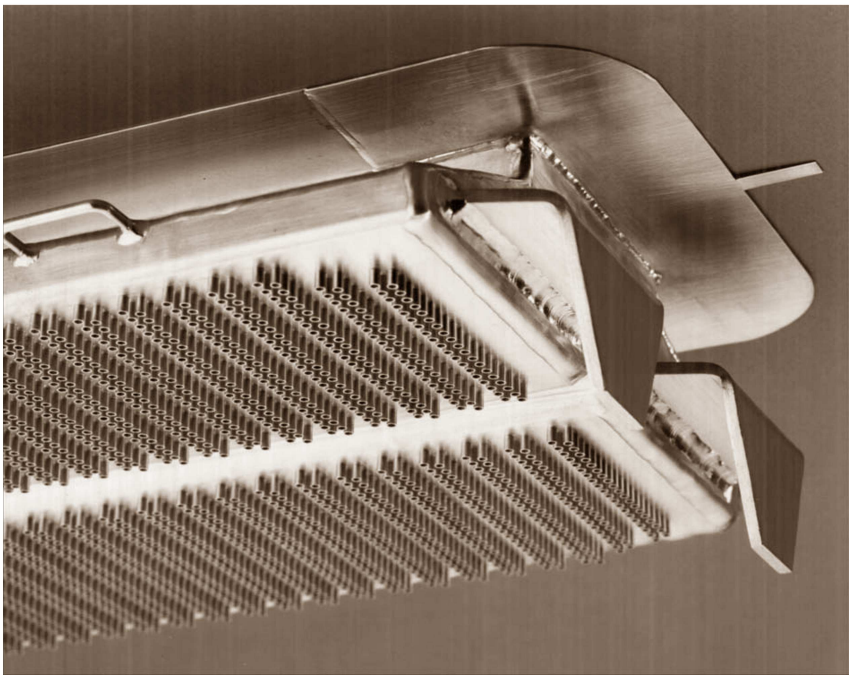

Figure 1.5: Bushing with several thousand tips. The curved trapezoidal-shaped plates at the end of the bushing plate are the ears, at which clamps can be attached to provide electrical power for global temperature regulation. Reproduced with permission of Heraeus Deutschland GmbH & Co [3].

the only on-line mechanism available for adjusting locally the temperature distribution of the bushing plate. Additional cooling is provided by water sprays further away from the bushing.

Finally, sizing is applied through an applicator to protect the fibers and improve their adhesion in the composite. Fibers are then brought together into a strand that is either wound or chopped. The final diameter of the resulting fibers depends on both the winder velocity and the glass flow rate at the bushing. It typically varies between 7 and 34 μm, depending on the product.

1.1.5 Fiber break as major challenge

Because of the low added-value of fiberglass and the high manufacturing costs (infrastructure, energy consumption, raw material,...), profit margins in glass fiber manufacturing are small. There is thus a strong need for reducing costs and improving the process efficiency.

One of the major limitations in process efficiency and production rate increase stems from the frequent break of fibers during the drawing process. A break occurring in a given fiber generally leads to the failure of the entire bushing position, which then needs

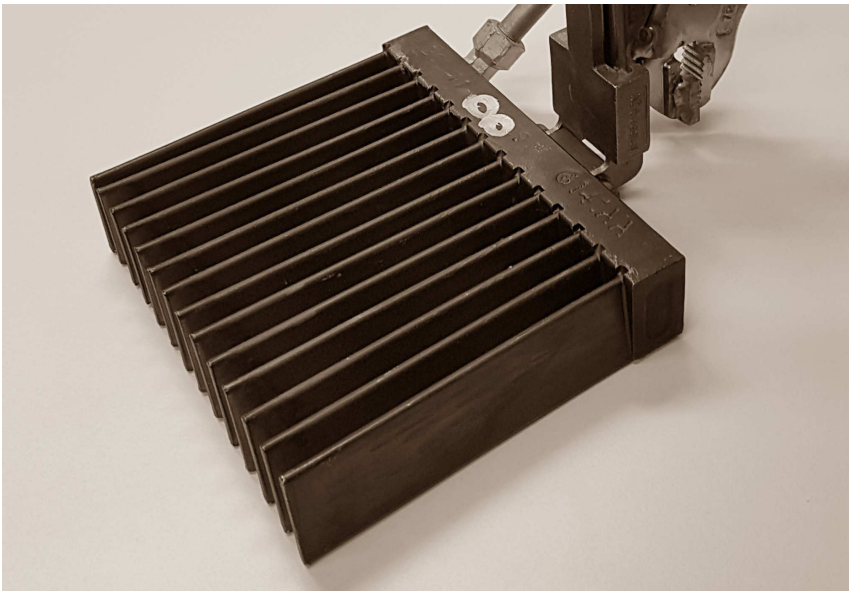

Figure 1.6: Picture of one set of finshields (2, 4 or 8 sets are typically used per bushing depending on the number of tip rows).

Figure 1.7: Half of a bushing in operation viewed from below. The finshields between each two rows of fibers are clearly visible.

to be manually stabilized by an operator. The restart of the bushing position takes several minutes, during which the glass flow cannot be stopped. A large quantity of glass, which can amount up to 15% of the total production, is thus lost. Recycling this glass waste would require an expensive treatment, which is currently not profitable. Besides costs generated by the material loss, this has also a negative impact on the environment. Furthermore, fiber breaks induce other indirect costs linked to energy losses, additional equipment wear and constraints in the bushing design and process. Figure 1.8 shows a typical daily break rate over an entire year. The break rate is expressed in number of breaks per bushing operating hours (B/BOH) and has been averaged over ~ 40 bushing positions of one furnace. In this example, the break rate averaged over the entire year is 0.71 B/BOH, which means that the bushing positions were stopped for five minutes per hour on average. This corresponds to an active production of 94% and about 600 kg per hour of wasted glass for one furnace. Note that the large break rate peaks observed in Fig. 1.8 were caused by melting issues in the backend.

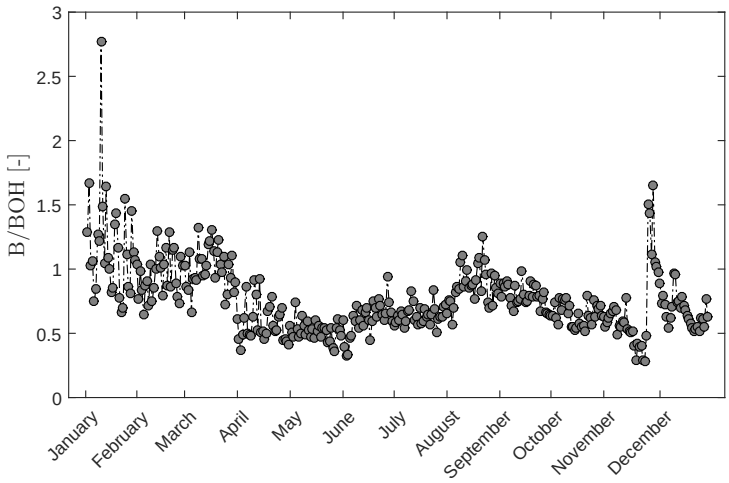

Figure 1.8: Time evolution of the fiber break rate averaged daily over ~ 40 bushing positions, expressed in number of breaks per bushing operating hours (B/BOH) for the year 2015.

The origins of the breaks are multiple: impurities, such as stone from refractories or dust convected by the HVAC cooling flow, gas bubbles in the melt, partial melting of the raw materials, thermal effects at the bushing plate,etc. Three main categories of break can be defined based on the vertical position below the tip where they occur. In the first region close to the tip, the glass is still at high temperature and liquid. In this case the broken jet forms a viscous drop since the pulling force has ceased, as depicted in Fig. 1.9. The analysis of the shape and content of the bead, i.e., the cooled drop, can provide information on the cause of the break. In addition, the break can also occur due to an

instability of the fiber surface called draw resonance. This instability typically occurs when the temperature of the tip and of the initial conical region of the fiber becomes too high and, thus, imposes an upper limit to the operating window of a bushing. On the other hand, if a break occurs further below, but before the applicator, the broken fiber becomes free to move and typically comes into contact with other fibers, leading to the rapid failure of the entire bushing position. In this case it is impossible to identify the reason for the break. Finally, if the fiber rupture takes place below the applicator, it is generally due to bad contact points or bad wetting.

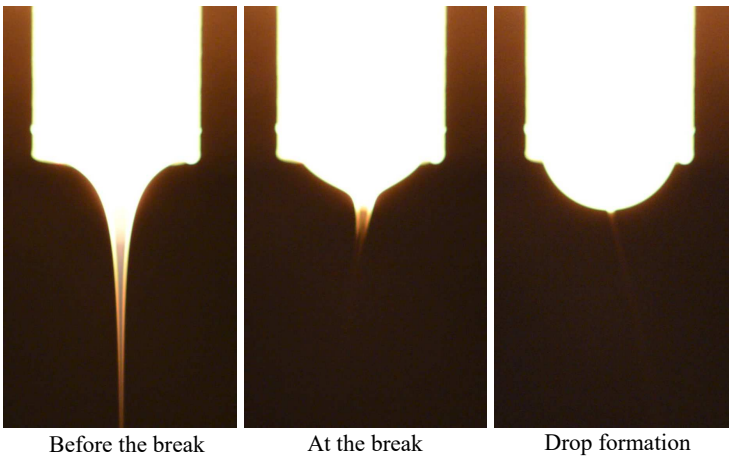

Figure 1.9: Formation of a bead after a break of the fiber close to the tip.

From these considerations it seems evident that reducing the break rate would significantly increase the production efficiency and thereby reduce costs. As many factors can impact the break, such as processes in the backend and frontend, glass composition, operating conditions, this thesis focuses on the drawing process itself. The aim is to obtain a detailed understanding of the underlying physics of the process, so as to understand the impact of operating conditions, geometric parameters or glass properties on the stress level within the fibers, and in turn on the brake rate. This fundamental knowledge could then provide leads towards new process optimization strategies.

1.2 State-of-the-art

Over the last fifty years, several authors have developed physical models to understand and predict the behavior of the fiber during the drawing process. Most of the research was funded by industrial companies or directly carried out by company scientists. As a consequence, very few results are openly available in the literature.

Some related research has been conducted in the context of fiber processing based on polymer materials. However, the corresponding physics significantly differs from the

high-temperature phenomena and rheology specific to glass fiber manufacturing, so that the results can only be partially exploited in the present context. On the other hand, some research is available regarding the drawing of optical glass fibers. Although glass is the material used in this case, the scales, the process design and the conditions are also very different. Consequently, this section solely focuses on results dedicated to the glass fiber drawing process for reinforced composites.

The first work on glass fiber drawing stems from Glicksman [4–6] in the 1960's. He derived the equations modeling the drawing of a single fiber. However, the limited computational resources and the lack of efficient numerical methods at that time prevented him from obtaining predictions for the entire fiber. He thus focused on the region where the slope of the free surface is small enough that a uniform radial profile of pressure and temperature can be assumed. Based on a one-dimensional Newtonian fluid model in steady state, he investigated the forced convection coefficient in laminar and turbulent air flow around the fiber. The result of the study was compared with experimental data and good agreement was found, providing credit to the one-dimensional assumption for the central region.

In the beginning of the 70's, Manfrè [7] studied the process both experimentally and theoretically. He found that the forming of the fiber could be separated into two main regions. On the one hand, the upper region is independent of the drawing velocity and is responsible for radial instabilities. According to his results, the forming instability occurs for a certain range of flow rate. Consequently, this part should be considered as an unsteady process in the model. On the other hand, he states that the lower part, situated around the transition point, is the region where the fiber breaks. Additionally, he demonstrated that the air drag and the variations of surface tension with temperature could be neglected.

Stehle and Brückner [8] investigated this process theoretically and experimentally in 1980. They established two different limits of the fiber drawing process: contraction and oscillation. The contraction is related to the wetting angle between the platinum, the glass and the ambient air. On the other hand, oscillations come from the instability of the free surface. According to their experiments, viscosity is a key factor that limits the process, in addition to the tip radius and cooling parameters.

A few years later, Huynh and Tanner [9] solved numerically the two-dimensional problem using a finite element method. The calculation domain included the tip and the first region of the forming fiber up to a distance of six times the length of the tip. Glass was considered as a Newtonian incompressible fluid and surface tension, body forces and air drag were neglected. The model was validated based on the experimental data from Glicksman [4]. The authors found that emissivity should be much lower than the value

usually used for glass in the solid state. Because the glass is at very high temperature in the region close to the tip exit and because of its semi-transparent nature, they argued that radiation coming from the bulk must have an important contribution. In order to account for the radiation from the bulk, they proposed to treat the radiative heat flux as a surface flux, similarly to an opaque medium, but with a modified effective emissivity. Moreover, this effective emissivity was made dependent on the fiber radius to capture the effect of the radius attenuation along the fiber. Their results largely focused on a sensitivity study based on heat transfer properties. They concluded that radiation is the dominant mode of cooling and that the value of the conductivity has an impact on the shape of the forming fiber. Finally, they emphasized that the lack of knowledge on material properties represent a major barrier to improving the accuracy of the model.

Perng *et al.* [10] took advantage of new developments in numerical methods and performed simulations of both a single and multiple fibers. The commercial software *Polyflow* was used to simulate the single fiber. The corresponding results were validated with the experimental data from Glicksman [4]. On the other hand, the simulations of several fibers were performed with the CFD software *Fluent* using a module developed specifically for this. Simulations focused on the flow of the ambient air. They included the effects of the fibers on the air flow, but did not consider the glass flow itself. The coupling was achieved through an iterative scheme.

Purnode and Rubin [11] also used a two-dimensional finite-element model with the software Polyflow in order to simulate the fiber behavior. Similarly to other works, the model was validated using data from Glicksman [4]. The model included surface tension and air drag. Their results confirmed that surface radiation is the main heat transfer mechanism near the tip exit, while convection becomes dominant further away. They have also shown that the forces involved are gravity, momentum from fiber acceleration and air drag. Unfortunately, the results are not explained in details since only a conference presentation is available. They suggested as future work studying the glass transition, the wetting of the tip and the transient aspects of the drawing process. Later, Purnode investigated this latter topic by analyzing the changes in the final fiber diameter following disturbances introduced in the tip temperature [12]. He demonstrated thus the destabilizing effect of surface tension and stabilizing effect of convection.

McKeone [13] performed experimental measurements of the air temperature and velocity around the fiber. The bushing plate was composed of nine tips. Using a thermocouple, the air temperature was measured at different locations along the vertical and horizontal coordinates. The results showed a high decrease of the air temperature along the vertical axis while horizontal variations were much lower. Additionally, it was found that the air temperature was also strongly affected by the bushing temperature and the winder

velocity. Similar trends were observed for the air velocity. However, he suggested that radiation from the bushing plate might induce errors in the measured air temperature, despite a correction model used on the data recorded. Sweetland [14] derived a model to describe the effect of water sprays on the cooling of the fiber. He found that water sprays impact the thermal boundary layer around the fiber leading to an increase of the convective cooling. According to his results, a higher amount of smaller droplets can lead to a better cooling efficiency of the water sprays.

More recently, Von Der Ohe [15] revisited the physics of the fiber glass drawing process. She developed a numerical model based on a Newtonian viscous flow to perform a parametric study of different glass compositions, process conditions and glass properties. She pointed out that the drawing speed and cooling conditions of the surrounding air are important, in particular for the final product properties. Moreover, part of her work focused on the impact of several process parameters on the viscous stress along the fiber. In particular, her results demonstrated that, at the same flow rate, higher winder velocity and higher cooling lead to a higher stress. Moreover, she concluded that the Deborah number, stress and cooling rate are linearly dependent on the winder velocity. Finally, her research pointed out the link between the tensile strength of the fiber and the viscous stress within the fiber during the forming. Nonetheless, the results were not directly oriented towards improving the industrial production.

Lenoble dedicated a part of her thesis to numerical simulations of the fiber forming process [16]. A one-dimensional model that takes into account radiation, convection, surface tension and drag was used to study both steady and unsteady effects, and in particular the process stability, such as oscillations of the fiber diameter. Results were also compared to experimental measurements for a single fiber. She identified a temperature range where stability is maximal; this range was also found to depend on the glass composition [17].

Rekhson was the first to investigate the fiber break mechanisms [18–21]. He postulated that the axial stress in the fiber was a good indicator for the break. He thus predicted breaking rates by combining stress values obtained from a one-dimensional model and a probabilistic approach. The latter relied on Weibbull statistical distributions. His predictions were then confronted to break statistics obtained on a bushing units with hundred filaments. Unfortunately, the major part of his available work does not provide scientific demonstrations of his results.

Finally, Liu [22] investigated numerically the variations of the final fiber diameter due to variabilities in the process and identified the temperature of the ambient air and of the furnace as their main cause. These findings led to the development of a control system to reduce the variations of the fiber diameter by adjusting the winder velocity.

In summary, most studies have focused on the development of a physical model for the upper region of the forming fiber, i.e., in the viscous region. The currently most advanced models assume a two-dimensional axisymmetric viscous flow. While the Newtonian constitutive equation within this region seems to be justified, the characterization of the heat transfer are not yet modeled accurately. All previous authors modeled the radiation flux as an opaque medium although glass must be considered as a participating medium for a certain range of radiation wavelengths. Internal radiation represents another contribution to heat transfer within the medium (in addition to conduction) and has never been included into any physical model for the fiber glass drawing process, although it has been suggested by several authors [9, 15, 16]. However, the mathematical modeling and the corresponding simulation of a semi-transparent fiber add major complexity, explaining the assumption of an opaque fiber used in previous works. On the other hand, convective cooling is always described through a correlation for the convective coefficient that it based on strong assumptions, i.e. a constant surrounding temperature and a constant fiber diameter. Because these two assumptions are clearly not valid in the case of glass fiber drawing, the application of this correlation is questionable. Another limitation of the current state-of-the-art is related to the rheology. As mentioned previously, the assumption of a Newtonian viscous fluid seems to be sufficiently accurate to describe the high temperature region, but it is likely to be invalid when the melt transitions into a solid glass. Although viscoelastic effects may strongly alter the prediction of the axial stress, they have not yet been taken into account. On the other hand, unsteady phenomena have been considered by some authors who highlighted their critical effects. But a rigorous stability map that includes all relevant physics has never been established. Few works have been dedicated to the experimental investigation of the process but were limited by the complexity of the measurements. Furthermore, although most results discuss the physics governing the process, they are not directed towards providing strategies for the process improvement. Finally, many questions regarding the fiber break remain unanswered: why does a fiber break? where does the break typically occur? how do the process conditions influence the break? which parameters are the most critical? how can the break rate be modeled? The main aim of this thesis is thus to address some of these limitations.

1.3 Objectives and methodology

The multi-physics and multi-scale nature of the problem makes it extremely complex and challenging from both a modeling and experiment point of view. It includes the fluid mechanics of both the glass melt and ambient air, heat transfer through conduction, convection and radiation, non-Newtonian rheology across the glass transition, unsteady

effects and instabilities,... The accuracy of any model also strongly depends on the material properties, which are very difficult to determine exactly due to the large range of temperatures involved. Moreover, a wide range of scales are involved. In particular, the axial characteristic length is of the order of 1 m while radial variations take place over very short distances, between 1 mm and 10 μm. Experimental measurements are also very difficult to perform due to the high temperatures and small scales, and involve a complex and expensive infrastructure. Finally, the industrial process typically involves several thousand of fibers at the same bushing, whose interaction compounds the problem complexity.

1.3.1 Objectives

The long-term goal of this research is to provide new strategies for improving the drawing process efficiency. As previously mentioned, a major lever is the reduction of the break rate. Because of the complexity of the problem, this can only be achieved through a better understanding of the physical processes involved and a model that includes all this physics. Moreover, some simplifications are required. In particular, the scope of this thesis is limited to the initial phase of the drawing process, i.e., it only considers the fiber from the tip until the transition point. The analysis considers neither the melt in the bushing, nor the backend processes, nor the fiber in its solid state. Additionally, it focuses only on a single fiber, and thus neglects the interaction between fibers.

In summary, the main objectives of this thesis are:

- to extend the current understanding of the physics involved in the glass fiber drawing process;
- to provide a physical model for the drawing of a single fiber that includes all relevant physics;
- to leverage numerical solutions of this model to suggest strategies for the process improvement;
- and to derive a probabilistic model of the break rate that uses inputs from the physical model.

More specifically, it aims at answering following key questions:

- What are the relevant physical phenomena?
- What is the influence of these physical phenomena?
- What are the key parameters of the process?

- What are the key indicators of the process robustness?
- How is the stress in the fiber related to the process conditions and glass properties?
- How do the key parameters influence the break rate?

The answer to these questions, and the physical and numerical models developed in this thesis are expected to provide the necessary basis for the improvement of the process. This could be achieved through several levers, such as the optimization of the operating window, the tuning of the glass composition to achieve specific material properties, and/or the improved design of the bushings, finshields, water sprays, or HVAC system. The potential impact is thus important and goes beyond increasing the production rate, but also includes reducing costs through a lower energy consumption, reduced need for expensive alloys, smaller waste amount,etc.

1.3.2 Methodology

In order to achieve the aforementioned objectives, a holistic approach is followed that includes theoretical, numerical and experimental work. The theoretical approach consists in developing mathematical models that include the relevant physics. These models are based on the well-known fundamental laws of fluid mechanics, heat transfer, thermodynamics, but also includes aspects related to material properties, glass transition, internal radiation, rheology,... It also exploits existing models available in the literature.

As these mathematical models are generally too complex to be solved analytically, numerical solutions are sought. Most of the simulations are performed with commercial software, in particular with Ansys Polyflow and Ansys Fluent, but a small in-house code has also been developed in Matlab to solve the simplest models. Numerical simulations are extensively used to assess the impact of the different parameters, level of fidelity of the physical models and material properties through systematic sensitivity analysis.

The models require several input parameters. Material properties represent one of the major inputs and sources of uncertainties. Some of their values have been obtained from the literature, but most of them from experimental measurements either sub-contracted to external laboratories or from internal measurements within 3B-the fiberglass company. Process conditions have also been provided by 3B-the fiberglass company. Additionally, numerical simulations require validation. To complement validation cases from the literature, experimental measurements on a dedicated fiberization unit have been conducted at 3B-the fiberglass company as part of this work. Because measurements are extremely challenging due to the high temperature and the limits of the measurement devices, only

a limited amount of data could be obtained. Nonetheless, it represents useful additional data for validation.

1.4 Summary by chapter

The present manuscript provides details on the work performed and summarizes the main findings. It is structured in eight chapters that each covers a specific part of the research. Chapter 2 describes the physical models and discusses their limitations. Then, the experimental measurements are presented in Chapter 3, followed by numerical aspects, and the simulation results in Chapter 4. The numerical models are subsequently used in Chapter 5 to analyze the physics of the drawing process. Chapter 6 leverages the numerical tools and the results of previous chapters to characterize the process in terms of the operating window and instabilities. Chapter 7 is a preliminary attempt to predict the break. Finally, the main conclusions are summarized and future work is suggested in Chapter 8.

Chapter 2

This chapter is entirely dedicated to the physics of the fiber drawing process and the development of a mathematical model. It begins with a brief introduction to the glass material and a description of how its rheology depends on its thermodynamic state. A two-dimensional viscous flow model for the upper region of the fiber is then derived, including the corresponding boundary conditions. Several aspects related to convective and radiative heat transfer are discussed. Subsequently, a simplified one-dimensional model is derived. As this model leads to a semi-analytical solution, it provides a very useful tool to better understand the physics and the role of the key process parameters. Its low computational cost makes it also very advantageous for sensitivity studies. A review of the molten glass properties is also found in this chapter since they are important input parameters to the model. Then, the next section presents a model to describe the flow of ambient air around the fiber, which is used to analyze the convective cooling. Finally, the last section introduces an semi-transparent radiation model to incorporate internal radiation.

Chapter 3

Chapter 3 focuses on the experimental measurements. It first describes the dedicated bushing unit that has been developed to study the drawing of a single fiber, as well as the different measurement techniques used. Then, the measurements of the fiber radius,

flow rate and external ambient temperature are presented and their limitations discussed. The development of the experimental unit, essential tool for investigating the break, and new validation data represent the main contributions of this chapter.

Chapter 4

The goal of this chapter is to present and discuss the numerical tools and methodology used to solve the different models presented in Chapter 2. The chapter discusses first the one- and two-dimensional models (i.e., finite difference and finite element methods), the radiation problem (i.e., discrete ordinate method), and the ambient air flow (i.e., finite volume method). Then, the procedure to couple simulations of the surrounding air flow and simulations of the fiber is presented. This coupling is one of the main contributions of this chapter, and leads to revisit the convective coefficient in Chapter 5 by considering the air environment around the fiber.

Chapter 5

Chapter 5 is entirely dedicated to understanding the physical mechanisms taking part in the drawing of the fiber. This analysis is based on the solution of the models developed in Chapter 2 using the numerical methods described in Chapter 4. First, the axisymmetric fiber model is investigated with respect to *i)* its sensitivity to the glass properties, *ii)* the contribution of each force and type of heat flux, and *iii)* several others parameters. The semi-transparent model is then studied including a sensitivity analysis to the radiative parameters and the impact of the model assumptions (such as grey body, opaque medium, ...). The results are also compared to those obtained with an effective-emissivity approach. Finally, a new correlation for the convective heat transfer coefficient is investigated and compared to the one classically used in the literature. The results of this chapter lead to a better knowledge of the process by characterizing which physical effects are important and must be considered, and which can be neglected. In particular, the contribution of each forces, the need for a semi-transparent model and the impact of the glass properties on the accuracy of the process are investigated in depth. A final contribution of this chapter is to highlight the limitation of the empirical correlation commonly used for the convective coefficient.

Chapter 6

In this chapter, the physical models are used to characterize the process operating window. A key performance indicator is defined to assess the impact of the production parame-

ters, glass composition, design of the bushing... Furthermore, the unsteady behavior of the process is analyzed in order to determine the critical parameter values that lead to instability. Although the approach does not rely on a formal linear stability analysis, it provides a first estimate of the stability limit of the process and highlights the key trends. The main achievement is to further improve the current understanding of the physical mechanism governing the fiber drawing and to suggest avenues for increasing the process robustness.

Chapter 7

This chapter summarizes a first attempt at modeling the break rate. It first presents the main characteristics of the break through a brief review of the literature. A probabilistic model of the fiber rupture is then derived based on several assumptions. As this model needs to be calibrated, an experimental measurement strategy is developed and discussed. Finally, preliminary results and the impact of the model assumptions are discussed in depth.

Chapter 2

Physical modeling of the fiber drawing process

In order to investigate the process and gain a more quantitative understanding of the detailed physics involved, the first step is to develop mathematical models describing this process. Optimally, these models should include both the cooling of the fiber, as the viscosity is a strong function of the temperature, and its rheological behavior, since the glass transitions from a liquid melt to a solid. Moreover, the cooling of the fiber involves the three modes of heat transfer, i.e., conduction, convection and radiation. The objective of this chapter is thus twofold: *i)* to identify the relevant physical processes, and *ii)* to describe the mathematical models used to represent them as accurately as possible.

Only a single fiber is considered here. Because most of the physical variations take place at high temperature, the modeling effort focuses on the liquid region. In particular, a two-dimensional axisymmetric model is derived, which attempts to include all relevant physics. Nonetheless, viscoelastic effects appearing during transition are not considered here. Moreover, glass is a semi-transparent medium so that radiation is not only a surface phenomenon. Internal radiation is initially neglected in the two-dimensional model but is treated in a separate section to assess its importance.

As the computational cost for solving the axisymmetric two-dimensional model is not negligible, a semi-analytical one-dimensional model based on Glicksman's model [5] is also derived. Although its solution is essentially analytical, a numerical treatment is still required to obtain the full solution. Nevertheless, it has the advantage of being much faster than the full two-dimensional model and of explicitly highlighting the influence of some physical parameters. Finally, these models rely on several material properties. As the experimental characterization of these properties of their temperature dependence is particularly challenging, they represent a major source of uncertainty, which is discussed in detail.

This chapter is organized as follows. In the first section, an overview of the characteristics of a glass material is presented including its corresponding rheological behavior. The next four sections, Section 2.2 to Section 2.6, focus on the liquid region of the forming fiber. The model of the glass flow in two dimensions is first derived in Section 2.2 including a discussion on the boundary conditions. In the next section, different approximations are applied to the model to obtain a simpler one-dimensional model. A complete review of the different glass properties is then presented in Section 2.4. This is followed by a brief description of a model for the air flow around the fiber in Section 2.5. Finally, internal radiation in semi-transparent media, not considered in the model of Section 2.2, is treated in detail in Section 2.6.

2.1 Introduction

This first section introduces the fundamental aspects of glass physics. Since the manufacturing process involves a large range of temperature from the liquid to the glassy state, the behavior of the glass for each different thermodynamic state and its corresponding rheology are described.

2.1.1 Volume-Temperature diagram of glass

Glass is a material demonstrating the same external appearance, and mechanical and thermal properties as a solid, while having the same structure as a frozen liquid, i.e. a long-range disorder [23]. One particularity of this material is the absence of a defined melting point. From the liquid to the glassy state, glass is transformed continuously without crystallization. Figure 2.1 shows the typical volume-temperature diagram for a glass material. At high temperature far above the transition, the glass is a melt in equilibrium from a thermodynamic point of view, represented by the region *ab* in the diagram. As the temperature decreases, the material follows the liquid line until point *b*. At this point (which is more a range than a well-defined temperature), the liquid may be transformed into a crystal if two conditions are met: *i)* a sufficient amount of nuclei are present, and *ii)* the cooling rate is low enough to allow the propagation of crystallization. However, if the cooling is sufficiently fast, the melt avoids crystallization and goes through a super-cooled state, as represented by line *bc*. Since the temperature decreases, molecules become less mobile leading to a dramatic increase of the viscosity.

With further cooling, the dynamic of the molecular structure becomes too slow to allow a return back to equilibrium. Consequently, the structural state tends to diverge from equilibrium and it cannot follow the initial linear volumetric decrease, as depicted by

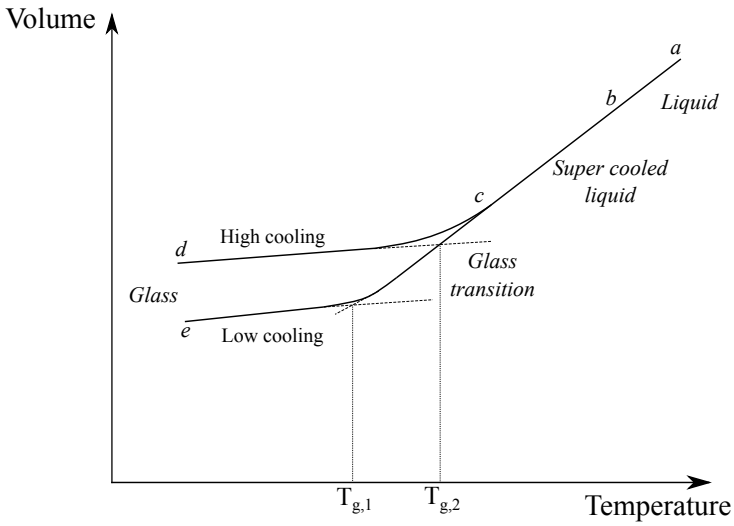

Figure 2.1: Typical volume-temperature diagram of a glass material.

the inflection of the curve at point *c*. At lower temperature, the volume decrease is again linear, but with a lower slope (point *d* and *e*). Between the super-cooled and the solid line, the curvature region is called *glass transition* and the corresponding *glass transition temperature* T_{g} is defined as the intersection of the super-cooled liquid and glassy state lines ($T_{\mathrm{g},1}$ or $T_{\mathrm{g},2}$ in the diagram). As shown in the diagram, the transition and the glassy state are strongly dependent on the cooling rate. The higher the cooling rate, the more rapidly the glass transition occurs. As a consequence, at a given temperature the (out-of-equilibrium) glass structure will depend on the cooling history (see points *d* and *e*). This dependence is quantified by a structural parameter called "fictive temperature". More precisely, the fictive temperature corresponds to the temperature at which the equilibrium melt structure would be identical to that currently existing in the glass. This implies that in the liquid region the fictive temperature is the actual glass temperature. In the solid region, the fictive temperature more or less corresponds to the glass transition temperature. This dependence of the transition and glass state on the cooling history is a characteristic of glass materials and represents a major challenge in modeling.

2.1.2 Rheology

During the drawing process, the fiber is rapidly cooled from a liquid state in equilibrium at high temperature to a solid state at room temperature, so that all thermodynamic states are involved. Correspondingly, the rheological characteristics change along the fiber. The forming fiber can thus be roughly divided into three different regions:

- The first region is defined as the part of the process where the glass is still in a liquid state. This region extends from the working point (where the viscosity is about 10^2

Pa·s) to the transition (where the viscosity has increased to about 10^{12} Pa·s). In this liquid phase, experiments have shown a linear response of the stress to a strain rate [24], characteristic of Newtonian fluids. The viscosity is thus independent of the stress at a given temperature, but strongly varies with the temperature. In particular, it increases by ten orders of magnitude between the working point and transition. Therefore, glass can be considered as a Newtonian viscous fluid with temperature dependent viscosity in this region.

- The second region corresponds to the part of the fiber where the glass passes through transition. During this step, the rheology is much more complex than in the previous region because it involves both viscous and elastic effects. In other words, glass behaves like a viscoelastic material, characterized by multiple relaxation times. In addition, the glass structure is frozen out of equilibrium, which implies a structural relaxation mechanism toward equilibrium. This relaxation is non-linear and involves relaxation times that are different from those linked to its viscoelastic behavior [25]. Furthermore, the structural relaxation is strongly coupled with the thermal history. This structural effect must be considered in addition to the viscoelastic model in order to entirely characterize the transition.

- Finally, the third and last region is defined as the region where the fiber is in a pure glassy state. The glass behaves there as a Hookean solid. Because the velocity is constant in this region, the fiber is in a state of pure translation without further mechanical deformations. Note that thermal deformation may still occur.

The boundaries between these regions are not well-defined since transition occurs continuously over a range of temperature. Viscoelastic effects begin gradually as the temperature approaches the transition temperature T_g. Following results in the literature (see Section 1.2), all variations of the physical fields are assumed to occur in the first region before transition. Therefore, the modeling effort mostly focuses on the liquid region, where glass can be considered as a Newtonian fluid.

2.2 Two-dimensional axisymmetric model

This section focuses on the development of the physical model for the upper part of the fiber forming where the glass is in the liquid phase, covering the region from the working point to the transition (from $\approx 1300°C$ to $\approx 750°C$). As mentioned in the previous section, the rheology corresponds to that of a Newtonian viscous flow. In this region, heat transfer plays a key role as the fiber is rapidly cooled, which in turn impacts its rheology,

as viscosity depends strongly on temperature. In particular, conduction occurs inside the fiber while convection and radiation at the fiber surface lead to the cooling of the fiber. Radiation dominates in the vicinity of the tip, as the temperature is high, but its contribution rapidly decreases along the fiber owing to the rapid cooling. Convective cooling is due to the cooler ambient air that is entrained by the high-velocity fiber.

The model is based on conservation laws with corresponding boundary conditions, and assumes that the fiber is axisymmetric. The formulation of the global balance equations include internal radiation, which is then neglected to simplify the discussion. Internal radiation modeling is treated separately in Section 2.6.

2.2.1 Transport equations

Because the flow is assumed axisymmetric, all field variables depend only on the radial and axial position, r and z. For a single fiber, the axial direction is typically aligned with the vertical direction. The liquid glass flow is governed by the equations of mass, momentum and energy conservation for an incompressible Newtonian fluid with variable density (i.e., density is independent of pressure but can depend on temperature):

$$\frac{\partial \rho}{\partial t} + \boldsymbol{\nabla} \cdot \rho \mathbf{v} = 0\,, \tag{2.1}$$

$$\rho \left[\frac{\partial \mathbf{v}}{\partial t} + (\mathbf{v} \cdot \boldsymbol{\nabla})\, \mathbf{v} \right] = \boldsymbol{\nabla} \cdot \boldsymbol{\tau} + \rho \mathbf{g}\,, \tag{2.2}$$

$$\rho c_p \left[\frac{\partial T}{\partial t} + \mathbf{v} \cdot \boldsymbol{\nabla} T \right] = \boldsymbol{\tau} : \boldsymbol{\nabla} \mathbf{v} + \boldsymbol{\nabla} \cdot (k \boldsymbol{\nabla} T) - \boldsymbol{\nabla} \cdot \dot{\mathbf{q}}_{\mathrm{r}}\,, \tag{2.3}$$

where $\mathbf{v} = v_r \mathbf{e_r} + v_z \mathbf{e_z}$ is the velocity vector, ρ the density, T the temperature, $\boldsymbol{\tau}$ the viscous stress tensor (including pressure), $\mathbf{g}$ the gravity acceleration and c_p the specific heat considered as constant in the liquid range (see Section 2.4). The heat flux within the glass is due to conduction represented by Fourier's law and a conductivity k, and the internal radiation through the term $\dot{\mathbf{q}}_{\mathrm{r}}$. The additional term, $\tau : \nabla \mathbf{v}$, corresponds to the viscous dissipation. In cylindrical coordinates, Eqs. (2.1)-(2.3) become respectively:

$$\frac{\partial \rho}{\partial t} + \frac{1}{r} \frac{\partial}{\partial r} (\rho r v_r) + \frac{\partial}{\partial z} (\rho v_z) = 0, \tag{2.4}$$

$$\rho \left[\frac{\partial v_r}{\partial t} + v_r \frac{\partial v_r}{\partial r} + v_z \frac{\partial v_r}{\partial z} \right] = \frac{1}{r} \frac{\partial (r \tau_{rr})}{\partial r} + \frac{\partial \tau_{rz}}{\partial z}, \tag{2.5}$$

$$\rho \left[\frac{\partial v_z}{\partial t} + v_r \frac{\partial v_z}{\partial r} + v_z \frac{\partial v_z}{\partial z} \right] = \frac{1}{r} \frac{\partial (r \tau_{rz})}{\partial r} + \frac{\partial \tau_{zz}}{\partial z} + \rho g_z, \tag{2.6}$$

$$\rho c_p \left[\frac{\partial T}{\partial t} + v_r \frac{\partial T}{\partial r} + v_z \frac{\partial T}{\partial z}\right] = \tau : \nabla \mathbf{v} \quad + \quad \frac{1}{r}\frac{\partial}{\partial r}\left(rk\frac{\partial T}{\partial r}\right) + \frac{\partial}{\partial z}\left(k\frac{\partial T}{\partial z}\right) + \frac{1}{r}\frac{\partial}{\partial r}\left(r\dot{q}_{\mathrm{r},r}\right) + \frac{\partial}{\partial z}\left(\dot{q}_{\mathrm{r},z}\right), \tag{2.7}$$

where $\dot{q}_{\mathrm{r},r}$ and $\dot{q}_{\mathrm{r},z}$ are the (r,z) components of $\dot{\mathbf{q}}_{\mathrm{r}}$.

Note that in the case of a single fiber in a uniform environment as considered here, the axisymmetric approximation is justified. On the other hand, the industrial process involves multiple filaments and finshields, whose relative spatial disposition induces azimuthal variations. To take into account these variations in the model requires the simulation of the air flow and heat transfer within the surrounding environment, which must be coupled to the simulation of the fiber. In addition, a three-dimensional model is needed which is computationally much more expensive. For all these reasons, angular variations are neglected.

Viscous stress

The molten glass is described as a Newtonian fluid leading to the following formulation for the stress tensor:

$$\boldsymbol{\tau} = -p\mathbf{I} + 2\eta\mathbf{D}, \tag{2.8}$$

where p is the isotropic pressure, η the dynamic viscosity and $\mathbf{D} = 1/2(\boldsymbol{\nabla}\mathbf{v} + \boldsymbol{\nabla}\mathbf{v}^{\mathrm{T}})$ the strain-rate tensor. Unlike other properties, the viscosity is highly sensitive to the temperature. Because of the rapid cooling of the fiber, it is critical to account for this temperature dependence. Viscosity is thus typically modeled with Vogel-Fulcher-Tamman (VFT) law:

$$\log_{10}\eta(T) = \log_{10}\eta_\infty + \frac{B}{T - T_{\mathrm{c}}}, \tag{2.9}$$

where η_∞, B and T_{c} are three constants that depend on the glass composition. This logarithmic dependence of the viscosity on the temperature leads to a strong coupling between the momentum and energy equation. The VFT equation is empirical and has been questioned by many authors, in particular due to the presence of a singularity at finite temperature T_{c}. As a result, the mathematical description of the viscosity is further discussed in Section 2.4.1. Unless mentioned otherwise, all results presented in this work are based on the VFT law.

Internal radiation

Glass is generally considered as a participating medium for the range of near-infrared wavelengths, so that internal radiation represents another contribution to heat transfer within the medium. Furthermore, a part of the flux from the bulk passes through the surface, which contributes to the cooling of the fiber. Accounting for the internal radiative heat flux $\dot{\mathbf{q}}_\mathrm{r}$ requires solving the radiative transfer equation, adding thereby significant complexity to the simulations. As a consequence, an entire section is dedicated to the internal radiation model (Section 2.6). The reference viscous model in the present section is assumed to be opaque for all wavelengths, grey (i.e. independent of the wavelengths) and diffuse. The internal radiative flux $\dot{\mathbf{q}}_\mathrm{r}$ is thus neglected and only surface radiation is considered. Heat transfer within the medium is consequently solely due to conduction and convection. This approximation is made in order to compare the results with previous work from the literature where internal radiation has not been considered. Moreover, the numerical treatment of the bulk radiation leads to a dramatic increase of the computing time. The impact of this simplification is discussed in Chapter 5.

2.2.2 Computational domain

The two-dimensional axisymmetric computational domain in cylindrical coordinates (r, z) is shown in Fig. 2.2. It includes the fiber up to a distance L from the tip exit and the glass flow within the tip itself. The origin of the coordinate system is located on the fiber axis just at the tip exit, and the axial direction z points downwards. The tip has a radius r_0 and a length l. The surface of the fiber below the tip is free to move and its position is a solution of the model. The surrounding air is not part of the computational domain. The ambient air flow is thus not explicitly resolved but its impact on the fiber is represented through a viscous drag force and a convective heat flux imposed as boundary conditions at the fiber surface. The axial length of the fiber domain is typically 8 cm, which is generally sufficiently long to reach a constant final radius of the fiber and simulate the entire viscous part before the transition. Nevertheless, this length is adapted for certain cases.

2.2.3 Boundary conditions

The governing equations, Eqs. (2.4)-(2.7), must be supplemented with boundary conditions to fully specify the problem. These boundary conditions include among others the surface heat fluxes responsible for the cooling of the fiber and the impact of the surrounding environment of the fiber.

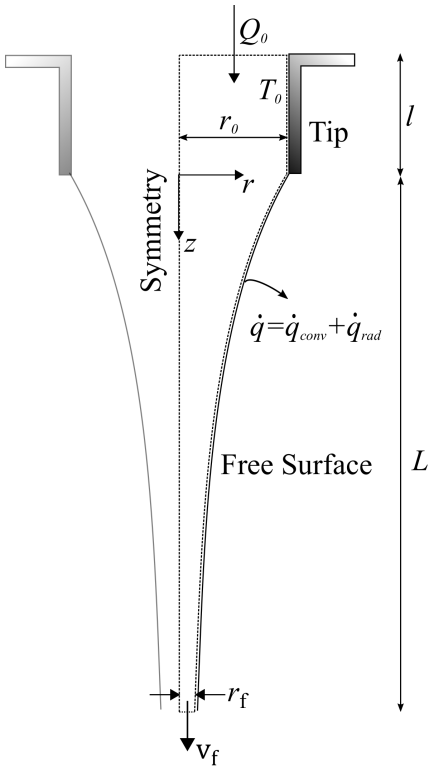

Figure 2.2: Schematic view of the tip and the forming fiber. The computational domain is delineated by the dotted line. The coordinate system and boundary conditions are also indicated.

Inlet, outlet and symmetry

At the inlet of the tip, temperature and velocity must be imposed. The glass flow entering the computational domain at the tip is driven by the hydrodynamic pressure of the glass column above it, and depends on the viscosity and the geometrical parameters of the tip. The working temperature T_0 is imposed at the inlet of the tip. Assuming a cylindrical shape of the tip, the volumetric flow rate is given by a Newtonian Poiseuille flow [26]:

$$Q_0 = \frac{\pi}{8\eta_0}\left(\frac{\mathrm{d}p}{\mathrm{d}z}\right) r_0^4 = \frac{\pi}{8\eta_0}\left(\frac{\rho g H}{l}\right) r_0^4 \,, \tag{2.10}$$

where $\mathrm{d}p/\mathrm{d}z$ is the static pressure gradient, g the gravity acceleration,, $\eta_0 = \eta(T_0)$ the inlet viscosity, and H the height of the glass column. If the tip cross-section is not cylindrical, the form of Eq. (2.10) must be modified. A list of relations for the flow rate associated to different tip shapes can be found in the work of Lowenstein [2]. The height H of the glass column, the tip radius r_0 and length l are generally imposed by the design of the bushing plate. Note that this relation is not accurate for significant temperature gradients along the tip and/or at high drawing velocity, in which case it must be adapted. Finally, at the

tip wall, a no-slip condition is imposed for the velocity.

In addition to being involved in the calculation of the flow rate, T_0 is also set as Dirichlet boundary condition for the energy equation at both the inlet and the tip wall. Defining the value of T_0 is not obvious since it is complex to measure due to the small diameter of the tip ($\approx$ 1-2 mm), limited accessibility in the production line and high temperature. Three options can be considered to estimate the value of T_0:

- By considering T_0 to be the working point, i.e., the temperature corresponding to a viscosity of 100 Pa·s.
- By deducing it from the measured flow rate. If Q_0 is known, for instance by measuring the weight of the fibers drawn during a certain time, Eq. (2.10) can be used to determine the viscosity η_0. Then, the temperature is obtained by inverting Eq. (2.9).
- By simulating the glass inside the bushing, above the tip.

The first option is usually considered in this work, unless mentioned otherwise.

The winder velocity is also a control parameter imposed in the process. At the outlet, the axial velocity is set to the velocity v_f while the tangential force is equal to zero. Although most of industrial companies use the final radius of the fiber r_f as a target, it is here an output and not an input of the model. By imposing the flow rate and the drawing velocity, mass conservation automatically determines the final fiber radius of the fiber at the outlet. Finally, because of the axisymmetric nature of the problem, a symmetry boundary condition is imposed along the fiber axis.

Free surface

Most of the interactions with the environment take place along the free surface. This includes for instance the viscous drag exerted by the ambient air and the cooling of the fiber by convection and radiation. Representing accurately these interactions is thus critical. The kinematic and dynamic interface conditions are given by

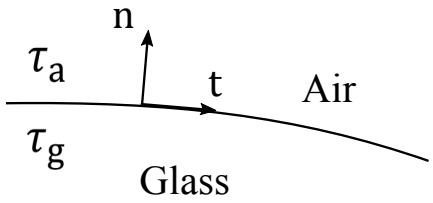

Figure 2.3: Interface between the glass and ambient air where $\boldsymbol{\tau}_\mathrm{g}$ and $\boldsymbol{\tau}_\mathrm{a}$ are the stress tensors for the glass and air, respectively, and $\mathbf{n}$ and $\mathbf{t}$ are the unit vectors that are normal and tangent to the surface.

$$\left(\frac{\partial \mathbf{x}_\mathrm{s}}{\partial t} - \mathbf{v}\right) \cdot \mathbf{n} = 0\,, \tag{2.11}$$

$$\mathbf{n} \cdot \boldsymbol{\tau}_\mathrm{g} - \mathbf{n} \cdot \boldsymbol{\tau}_\mathrm{a} = \gamma \mathbf{n} \left(\boldsymbol{\nabla} \cdot \mathbf{n}\right)\,, \tag{2.12}$$

where $\mathbf{x}_\mathrm{s}$ is the position of the free surface, γ the surface tension, $\mathbf{n}$ the surface normal, and $\boldsymbol{\tau}_\mathrm{g}$ and $\boldsymbol{\tau}_\mathrm{a}$ the interface stress tensors for glass and air, respectively. A schematic representation of the interface is shown in Fig. 2.3. The term $\mathbf{n}\cdot\boldsymbol{\tau}_\mathrm{g}$ in Eq. (2.12) represents the stress exerted by the glass on the air, which is simply obtained from the velocity field given by Eq. (2.8). The second term, $\mathbf{n} \cdot \boldsymbol{\tau}_\mathrm{a}$, is the stress from the air flow acting on the glass, typically called air drag. This latter effect is discussed further below. Finally, the term on the right-hand side of Eq. (2.12) is the force induced by surface tension, which itself depends on temperature (more details on this are given in Section 2.4).

Radiative and convective heat fluxes are imposed at the free surface:

$$\dot{q}_\mathrm{s} = \dot{q}_\mathrm{s,conv} + \dot{q}_\mathrm{s,rad}, \tag{2.13}$$

where each term is further developed below.

Velocity and thermal boundary layers

The fiber is typically drawn at high velocity. The ambient air is thus entrained by viscous forces and a boundary layer forms around the fiber surface, as illustrated in Fig. 2.4. The large velocity gradients at the surface create in turn a drag force acting on the fiber. Similarly, the ambient air is typically at a much lower temperature than the fiber. Air entrainment also creates a thermal boundary layer and the associated convective heat transfer. Note that if additional cooling through an air conditioner is used (this is typical in the industrial process), then the air flow might have not only a component parallel to the fiber, but also a transverse component.

Different theoretical works have investigated the form of these boundary layers in order to predict the drag and the convective heat transfer coefficients. The studies focused first on a filament with constant radius at rest subjected to an air flow. The attenuation of the fiber, induced by the drawdown, was later investigated. The research started with Sakiadis [28] who calculated the velocity and thermal boundary layers using the Karman-Pohlhausen integral method and assuming that the filament velocity is constant and the flow laminar. Glicksman [6] used Reynolds analogy to obtain the Nusselt number and the drag force for a filament with constant diameter. The curvature of the surface was taken into account later by Sayles [29] who found an increase of the Nusselt number in this case. Using integral techniques, Kubo [30] found that the drawdown leads to a decrease of the

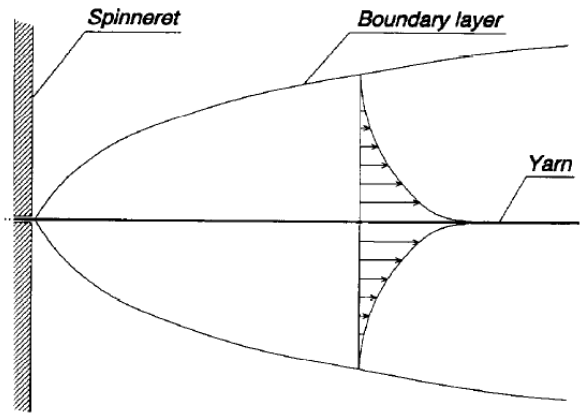

Figure 2.4: Schematic of the boundary layer developing along a filament with constant radius moving in air at rest (taken from [27]).

thickness of the boundary layer (after a short initial growth) until it reaches a constant value proportional to the filament thickness, as shown in Fig. 2.5. However, his analysis was applied to specific cases of fiber spinning and not to a general fiber drawing process. Finally, Miller [31] calculated the Nusselt number and the drag force and found the same behavior of the drag as Sayles, i.e. the drag increases with the drawdown. Nevertheless, unlike Sayles, his work shows that the Nusselt number tends to decrease due to the drawdown. His justification is based on the questionable validity of the Reynolds analogy when the drawdown is considered. Note that his work is only valid for laminar flows.

A large amount of experimental work have also focused on finding a correlation for the Nusselt number and the drag coefficient. Each work is dedicated to a range of experimental conditions expressed through the Reynolds number. In particular, a parallel and a transverse Reynolds number are defined to represent the parallel and transverse flow. They are expressed respectively as

$$\mathrm{Re}_{\perp} = \frac{v_{\perp} 2 r_{\mathrm{s}}}{\nu_{\mathrm{a}}}, \tag{2.14}$$

and

$$\mathrm{Re}_{\parallel} = \frac{v_z 2 r_{\mathrm{s}}}{\nu_{\mathrm{a}}}, \tag{2.15}$$

where $v_{\perp}$ is the transverse air velocity, r_{s} is the radius of the fiber, v_z is the axial velocity at the surface and ν_{a} the air kinematic viscosity.

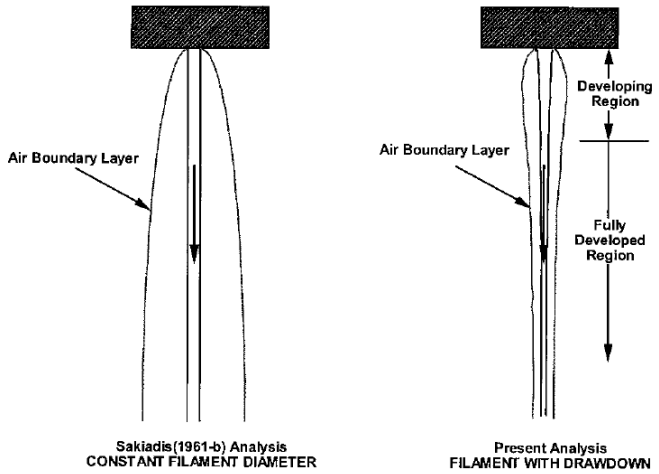

Figure 2.5: Schematic of the boundary layer in case of a constant radius filament moving in air at rest (left) and of fiber drawing (right) (taken from [31]).

Drag force

The component of the shear stress $\boldsymbol{\tau}_\mathrm{a}$ exerted by the surrounding air in Eq. (2.12) can be expressed through a friction coefficient c_f [32]:

$$\mathbf{n} \cdot \boldsymbol{\tau}_\mathrm{a} \cdot \mathbf{t} = \frac{1}{2} \rho_\mathrm{a} c_\mathrm{f} v^2 \mathbf{t}, \tag{2.16}$$

where $\mathbf{t}$ is the unit vector along the fiber and tangential to its surface, v the amplitude of the local glass velocity $\mathbf{v}$ at the surface and ρ_a the air density.

The results from the experimental and theoretical works led to an expression for c_f as a function of the parallel Reynolds number $\mathrm{Re}_\parallel$ [32]:

$$c_\mathrm{f} = a \left(\mathrm{Re}_\parallel \right)^b. \tag{2.17}$$

Different values for the parameters a and b have been found in the literature from both theoretical and experimental studies, depending on the range of Reynolds number considered. In this work, $\mathrm{Re}_\parallel$ varies between 1 and 10, depending on the final radius (17 to 10 μm), the winder velocity ($\approx$ 20 m/s) and the temperature of the surrounding air (25°C - 600°C) influencing ν_a. Note that this latter value is taken for dry air.

Unlike for the polymer spinning process, most of the works on fiber glass drawing have neglected the drag force such as Manfrè [7], Huynh and Tanner [9], Lenoble [16] or Von Der Ohe [15]. They justified this simplification by the small magnitude of this force compared to the viscous force. However, this assumption has never been quantitatively assessed. On the other hand, some authors have taken into account the air drag in their

physical model. Glicksman [6] calculated the parameters from turbulent boundary layer theory around a cylinder and found $a = 0.4$ and $b = 0.7$ within the range $\mathrm{Re}_{\parallel} < 100$. Purnode [11, 12] considered the value of $a = 0.26$ and $b = 0.734$ from the work of White and Ide [33]. A summary of the correlation parameters a and b and their range of validity is provided in the books of Beyreuther [32] and Ziabicki [26]. In the present work, the parameters from Glicksman have been chosen, but the sensitivity of the model due to variations of these values has been evaluated. Finally, no cross-flow is considered.

Convective heat transfer coefficient

The expression of the convective flux at the surface of the fiber can be written as

$$\dot{q}_{\mathrm{s,conv}} = h\left(T_{\mathrm{s}} - T_{\mathrm{ext,conv}}\right), \tag{2.18}$$

where h is the convective heat transfer coefficient and $T_{\mathrm{ext,conv}}$ is the temperature of the surrounding air outside of the boundary layer. h is typically expressed in non-dimensional form through the Nusselt number:

$$\mathrm{Nu} = \frac{h 2 r_{\mathrm{s}}}{k_{\mathrm{a}}}, \tag{2.19}$$

where k_{a} is the air thermal conductivity. Note that in the present case, because of the fiber radius attenuation, the fiber radius r_{s}, and thus the Nusselt number, are not constant but functions of z. The different studies have shown that the general form of the Nusselt number Nu can be expressed in terms of parallel and transverse air flow and is written as [32]

$$\mathrm{Nu} = c_1 \left(\mathrm{Re}_{\parallel}^2 + c_2 \mathrm{Re}_{\perp}^2\right)^{c_3}, \tag{2.20}$$

where c_1, c_2 and c_3 are fitting parameters, and $\mathrm{Re}_{\perp}$ and $\mathrm{Re}_{\parallel}$ are defined in Eqs. (2.14) and (2.15), respectively. These coefficients are obtained under different conditions based on the Reynolds numbers and experimental setup. A review of all the coefficients can be found in the book of Beyreuther [32].

The most widely used empirical correlation comes from the work of Kase and Matsuo [34]. They obtained this relation using a wire with a constant diameter of 0.2 mm subjected to an air flow at constant velocity and temperature. The correlation is given by

$$\mathrm{Nu} = 0.42 \mathrm{Re}_{\parallel}^{0.334} \left(1 + \left(\frac{8 v_{\perp}}{v}\right)^2\right)^{0.167}, \tag{2.21}$$

where v is the velocity of the filament. In the case of a single fiber considered here, the

entrained air flow is mostly parallel to the fiber [1], so that the transverse component can be neglected. This leads to

$$\mathrm{Nu} = 0.42\mathrm{Re}_{\parallel}^{0.334}, \tag{2.22}$$

for the Nusselt number, and to

$$h = 0.42\,\frac{k_\mathrm{a}}{2r_\mathrm{s}}\,\mathrm{Re}_{\parallel}{}^{0.334}\,, \tag{2.23}$$

for the convective heat transfer coefficient, where k_a is the air thermal conductivity. Note that the presence of the bushing plate and the cone shape of the free jet induce a more complex flow in the region close to the tip than the experimental setup used to obtain the correlation. Thereby, some inaccuracies can be expected in the prediction of the convective heat flux in this region. Nonetheless, in spite of the large number of available correlations, Kase and Matsuo relation (2.22) is used here as a starting approximation since it has been used in most studies on fiber glass [9, 11, 15, 19].

Figure 2.6 shows an example of the convective heat transfer coefficient as a function of the axial coordinate computed with Eq. (2.23) for typical industrial conditions (see Chapter 5). Initially, h rapidly increases because of the attenuation of the radius of the fiber and the large increase of the fiber velocity. Further down, the coefficient reaches a constant value when the forming fiber has converged to its final diameter.

The correlation (2.23) was developed for a constant radius r_s, a constant velocity and a constant surrounding temperature. Consequently, $T_\mathrm{ext,conv}$ must be constant in order to be consistent with the correlation. Nonetheless, considering a constant air temperature around the fiber is a strong approximation for both single and multi-fiber drawing. More specifically, the ambient air is generally first strongly heated in the vicinity of the bushing plate (whose temperature is around T_0) before being entrained downwards by the fiber. The temperature $T_\mathrm{ext,conv}$ seen by the fiber thus varies axially. This was highlighted by McKeone [13] who measured experimentally the air temperature both radially and axially on a nine tip bushing. On the other hand, Offermans [35] used numerical simulations to calculate the temperature profile for a complete bushing position and found that the air temperature exhibits strong gradients in both axial and radial directions around the fibers. Furthermore, the air flow was observed to be turbulent. In addition, $T_\mathrm{ext,conv}$ has been measured in this work using a bushing with a single tip. The results are detailed in Chapter 3. Based on the results of Offermans [35], McKeone [13] and the results from the experimental investigation, the convective air temperature could be approximately

[1] The air flow is much more complex in the case of a complete bushing position with multiple filaments, and one has to resort to numerical simulations of the flow to accurately predict the convective heat transfer.

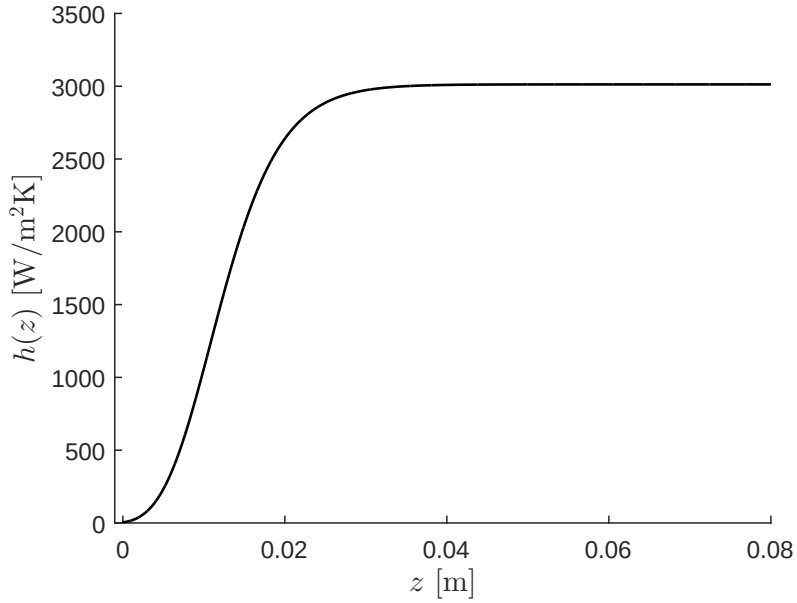

Figure 2.6: Convective heat transfer coefficient $h(z)$ as a function of the distance from the tip z predicted by Eq. (2.23). The process conditions are: $v_\mathrm{f} = 21.3$ m/s, $Q_0 = 1.677 \cdot 10^{-9}$ m^3/s, $r_0 = 0.6 \cdot 10^{-3}$ m and $T_0 = 1300$°C.

described by

$$T_{\mathrm{ext,conv}}(z) = T_\mathrm{r} + (T_\mathrm{b} - T_\mathrm{r}) \exp(-az), \tag{2.24}$$

where T_r is the room temperature at the winder, T_b the air temperature at the bushing plate and a a parameter defining how the air temperature decreases axially. The values found experimentally are presented in Chapter 3.

As the correlation for h has been developed for a constant external temperature, applying it with an axially-varying temperature $T_{\mathrm{ext,conv}}(z)$ (i.e., by assuming a quasi-equilibrium at each location z) is questionable. Therefore, unless specified otherwise, simulations hereafter have been performed using a constant average air temperature $T_{\mathrm{ext,conv}}$, which was estimated at 600°C from the simulations of Offermans [35] in case of multi-fiber bushing and at room temperature from experimental measurements in case of a single fiber bushing. This problem is further discussed in Chapter 5, where simulations with a temperature $T_{\mathrm{ext,conv}}$ that varies with z according to Eq. (2.24) are also performed.

Finally, the application of the correlation itself can be questioned considering the radius attenuation in the region close to the tip, where heat transfer is critical. Despite these deficiencies, Kase and Matsuo correlation is used here since it is the most widely used correlation in the literature. A specific section of Chapter 5 focuses on providing a more accurate representation of the convective heat flux.

Radiation

The forming fiber is here initially assumed to be an opaque and grey medium for all wavelengths, so that radiation is only emitted at the surface of the fiber, and the surface absorbs and reflects diffusely the radiation flux from the surrounding environment. In the case of multi-filament bushing, the surrounding components interacting with the fiber are the finshields, the tip plate, the fiber itself, the surrounding fibers and the room. Furthermore, all contributors influence each others and the system is fully coupled. In the case of a single filament bushing, the finshields and the surrounding fibers are not present (see Fig. 2.7).

Since the two-dimensional model is derived for an axisymmetric case, angular variations are neglected in the equations. For multi-filament bushing, the radiative contributions of the finshields and the surrounding fibers are function of the angular direction, which cannot be captured under the axisymmetry assumption. On the other hand, interaction with the tip plate can play an important role. Because of the concavity of the cone shape of the forming fiber, the plate is not seen by an element of the fiber surface in this region. When the concavity becomes smaller, the fiber surface can interact with the plate. Additionally, the concavity of the fiber induces an interaction between the upper and lower parts of the fiber. Both the interactions between the fiber and the plate, and the fiber with itself are neglected here, but the impact of this approximation is discussed in Chapter 5, where the surrounding environment is simulated.

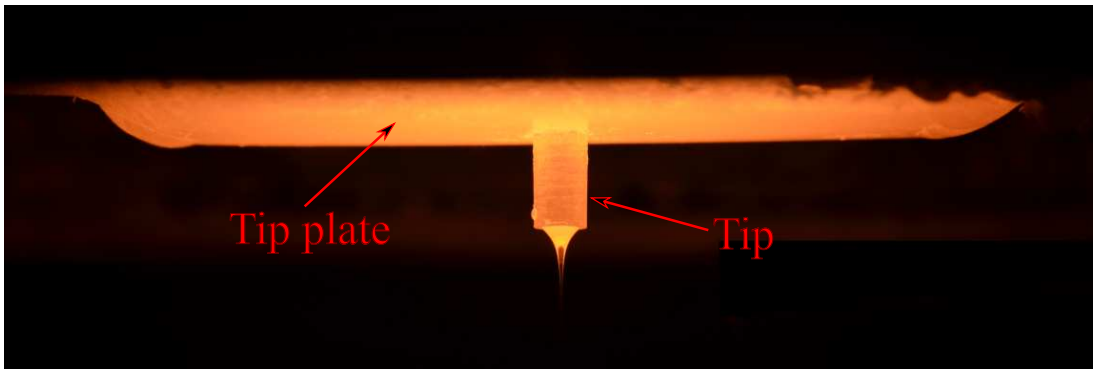

Figure 2.7: Picture of a tip plate for a single fiber bushing.

Under these assumptions, the radiative environment for the fiber is treated here as a black body, such that

$$\dot{q}_{\mathrm{rad}} = \epsilon_{\mathrm{s}} \sigma \left(T_{\mathrm{s}}^4 - T_{\mathrm{ext,rad}}^4 \right). \tag{2.25}$$

where ϵ_{s} is the emissivity of the surface, σ Stefan-Boltzmann constant, T_{s} the fiber surface temperature and $T_{\mathrm{ext,rad}}$ the temperature of the surrounding medium. In the case of single fiber bushing, $T_{\mathrm{ext,rad}}$ is the room temperature and is set at 25°C. If a multi-

filament bushing is considered, the fiber sees directly the finshields. As a result, $T_{\text{ext,rad}}$ is approximated at the average finshield temperature. This temperature is equal to 200°C, as shown by Offermans [35].

2.3 One-dimensional model

The axisymmetric model described in the previous section has the advantage of considering both axial and radial variations, and of including most of the relevant physics. However, the numerical convergence is slow due to the different length scales involved, the free surface and the non-linear viscosity law. As a consequence, simulations of many different cases is very time-consuming. For this reason, a simplified one-dimensional model has been developed based on the work of Glicksman [5], which was used later by Rekhson [18] and Lenoble [16]. Glicksman's model is based on the reduction of the dimension of the problem by considering only axial variations of all variables. Starting from these equations, this model is further simplified here by neglecting the influence of some forces leading to a semi-analytical solution. Unlike Glicksman's model, the form of the model proposed here highlights the dependency of the solution on key parameters and provides a powerful tool to understand the underlying physics. Evidently, these simplifications reduce its accuracy compared to the two-dimensional model, as discussed in Chapter 5. The one-dimensional steady-state approach of Glicksman, where only radial variations are neglected, is first presented. Based on this model, the present simplified formulation is then derived.

2.3.1 Glicksman model

Glicksman [5], followed by Rekhson [18] and Lenoble [16], considered a one-dimensional simplification of the equations described in Section 2.2. Starting from the Navier-Stokes equations written in the axisymmetric assumption, Eqs. (2.4)-(2.7), he integrated them over the cross section of the fiber in order to obtain a one-dimensional form. He assumed that the resulting equations are only valid for a region where the relative radius variation is less than one tenth, called the central region. He also neglected the influence of internal radiation, based on the low value of the optical thickness in this central region, and of viscous heating. However, he included the air drag, surface tension and gravity effects.

This led to the following set of equations:

$$\rho v_z S = \rho Q_0, \tag{2.26}$$

$$\underbrace{\rho v_z S \frac{\partial v_z}{\partial z}}_{\text{Inertia}} = \underbrace{\frac{\partial}{\partial z}\left[3\eta S \frac{\partial v_z}{\partial z}\right]}_{\text{Viscous force}} + \underbrace{\frac{\partial}{\partial z}\left[\gamma\sqrt{\pi S}\right]}_{\text{Surface tension}} + \underbrace{\rho g S}_{\text{Gravity}} - \underbrace{2\tau_a\sqrt{\pi S}}_{\text{Drag}}, \tag{2.27}$$

$$\rho v_z S c_p \frac{\partial T}{\partial z} = k\frac{\partial}{\partial z}\left[\frac{\partial T}{\partial z}\right] + \dot{q}_s, \tag{2.28}$$

where $S(z) = \pi r(z)^2$ is the cross section of the fiber along the axial coordinate, and $\dot{q}_s$ is the heat flux at the free surface given by Eq. (2.13). The detailed derivation of these equations is given in the works of Glicksman [5] and Lenoble [16]. Eqs. (2.26)-(2.28) were then solved numerically, but no comparison with a more accurate two-dimensional model was made.

2.3.2 Semi-analytical model

Although the complexity of the problem is reduced, Eqs.(2.26)-(2.28) still do not provide explicit information about the underlying physics. However, further simplifications, i.e., neglecting some forces, can be applied to obtain a semi-analytical form. In particular, Glicksman's model (and the two-dimensional model of Section 2.2) takes into account the viscous, drag, inertia, gravitational and surface tension forces acting on the fiber.

By neglecting all but viscous forces, Eq. (2.27) simplifies to

$$\frac{d}{dz}\left[3\eta S \frac{dv_z}{dz}\right] = 0. \tag{2.29}$$

This strong simplification is motivated by the fact that the viscous force has the largest contribution owing to the very large glass viscosity, as discussed in Chapter 5. Integrating Eq. (2.29) gives

$$3\eta S \frac{dv_z}{dz} \equiv F(z) = \text{const}\,. \tag{2.30}$$

In other words, considering only the viscous force implies that the tensile force $F(z)$ is equal to a constant along the coordinate z. Using Eq. (2.26), the latter equation becomes

$$3\eta \frac{Q_0}{v_z}\frac{dv_z}{dz} = F, \tag{2.31}$$

which can be integrated between 0 and z to yield

$$v_z(z) = v_0 \exp\left(\frac{F\varphi(z)}{3Q_0}\right), \tag{2.32}$$

where $v_0 \equiv v_z(z=0)$ is the velocity of the glass at the tip and φ is the fluidity, defined as

$$\varphi(z) \equiv \int_0^z \frac{1}{\eta(z')} \mathrm{d}z'. \tag{2.33}$$

Note that the viscosity also depends on z through Eq. (2.9) as $\eta(z) = \eta\left(T(z)\right)$. Evaluating Eq. (2.32) at the coordinate where the drawing force is applied, $z = z_\mathrm{f}$, one obtains

$$F = \frac{3Q_0}{\varphi_\mathrm{f}} \ln\left(\frac{v_\mathrm{f}}{v_0}\right), \tag{2.34}$$

with

$$\varphi_\mathrm{f} \equiv \varphi(z_\mathrm{f}) = \int_0^{z_\mathrm{f}} \frac{1}{\eta(z')} \mathrm{d}z' \,. \tag{2.35}$$

Equation (2.34) for F can now be used in Eq. (2.32) to obtain

$$v_z(z) = v_0 \left(\frac{v_\mathrm{f}}{v_0}\right)^{\varphi(z)/\varphi_\mathrm{f}} . \tag{2.36}$$

Using the conservation of mass, Eq. (2.26), the radius of the fiber is given by

$$r(z) = r_0 \left(\frac{v_\mathrm{f}}{v_0}\right)^{-\varphi(z)/2\varphi_\mathrm{f}} . \tag{2.37}$$

Finally, the axial stress $\tau_{zz} = F/S$ is given by

$$\tau_{zz}(z) = \frac{3}{\varphi_\mathrm{f}} v_z(z) \ln\left(\frac{v_\mathrm{f}}{v_0}\right) . \tag{2.38}$$

The integral $\varphi(z)$ represents the variation of viscosity along the fiber. Because of the temperature dependence of the glass viscosity, as given by Eq. (2.9), $\varphi(z)$ is highly dependent on the temperature field. Low values of viscosity in the high temperature region (i.e., close to the tip) represent the largest contribution to φ_f. Consequently, a small variation in the fiber temperature in this region generates a large impact on the fluidity, and thereby on the flow. The integrals $\varphi(z)$ and φ_f are the only link between the flow dynamics and the cooling process. However, these equations require solving the energy equation to obtain the temperature profile:

$$\frac{\mathrm{d}T(z)}{\mathrm{d}z} = -\frac{2\pi r_0}{\rho c_p Q_0} \dot{q}_\mathrm{s}(z) \left(\frac{v_\mathrm{f}}{v_0}\right)^{-\varphi(z)/2\varphi_\mathrm{f}} , \tag{2.39}$$

where internal radiation, conduction and viscous dissipation inside the fiber have been neglected. The solution of the one-dimensional model is not entirely analytical because Eq. (2.39) requires a numerical solution, but numerical treatment is much less time con-

suming compared to the two-dimensional model and Glicksman's model. The numerical method for solving Eq. (2.39) is presented in Chapter 4.

Although the above simplifications reduce the accuracy of the solution, the set of equations provide a useful basis to understand the underlying physics and, in turn, to identify strategies to reduce the stress. In particular, Eq. (2.38) demonstrates that the axial stress depends on three parameters: the drawing ratio v_f/v_0, the drawing velocity v_z and the final value of the fluidity φ_f. This can be used to optimize the operating window, as discussed in details in Chapter 6. Additionally, the accuracy of this simplified model compared to the axisymmetric two-dimensional model is discussed in Chapter 5.

2.4 Material properties

The equations of the viscous non-isothermal model require the properties of the molten glass such as the viscosity, the specific heat, the density, the thermal conductivity and the surface tension. The range of temperature over the region of interest is more than 500°C and consequently, the thermal variability of the properties may have an impact. Unless otherwise specified, the glass considered in this work is the commercial Advantex©. Unfortunately, material properties are very sensitive to the glass composition and measured data is not available in the literature for this glass as it is a commercial glass. As a result, measurements of all required material properties over the relevant range of temperature have been subcontracted to external laboratories. The present section describes each property and their relative variation with temperature. In particular, the viscosity is discussed in more details since it is a key property in the glass forming process.

2.4.1 Viscosity

The forming behavior of a liquid and super-cooled glass is essentially driven by the viscosity. Viscosity is a measure of the internal friction due to the relative motion of different layers of a fluid. More specifically, the viscosity η is defined as the ratio of the shear stress to the shear rate. For a Newtonian fluid, this ratio is independent of the shear rate, so that stress and shear are linearly proportional.

Since viscosity varies dramatically with temperature, it determines at which temperature the glass can be melted or produced. A typical viscosity-temperature curve is shown in Fig 2.8. In particular, the viscosity increases strongly and continuously as the temperature decreases. Different reference viscosity points are generally used in the industrial process:

Melting point ($10^1 - 10^2$ Pa·s) Viscosity in the furnace required to perform a complete

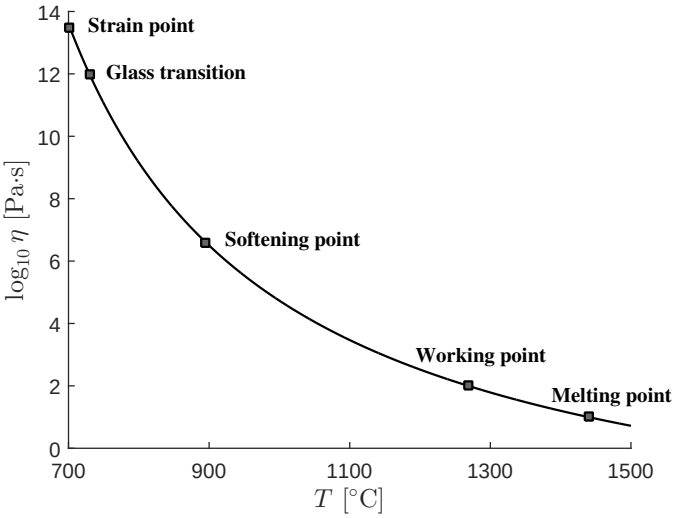

Figure 2.8: Viscosity as a function of the temperature for the Advantex© composition.

homogenization of the melt.

Working point ($10^2 - 10^3$ Pa·s) Viscosity at which the glass can be transformed into its final shape. In the fiber glass process, the working point is taken at $\eta \approx 10^2$ which more or less corresponds to the viscosity at the tip exit. For other forming processes, the working point can be around $\eta \approx 10^3$.

Softening point ($10^{6.6}$ Pa·s) Viscosity at which the glass can sustain its own weight without continuous deformation.

Transition/annealing point (10^{12} Pa·s) Viscosity value assumed for the glass transition temperature T_g. It is also called the annealing point. It is related to the relaxation of the stress, which takes several minutes at this temperature. This reference point is thus used to remove residual stresses within the glass.

Strain point ($10^{13.5}$ Pa·s) Viscosity at which the stress relaxes within a few hours.

These reference points are useful in the glass industry since they determine the temperature required at each step of the manufacturing process. The viscosity-temperature curve is essential in a glass forming process because it gives a measure of the energy required, and thus the cost of production, to melt and produce a glass. The objective is generally to obtain a glass composition with a low melting temperature.

Viscosity law

The temperature dependence of the viscosity can be expressed mathematically through different relations. Depending on the composition, the viscosity can follow different for-

mulations. As a result, Angell [36] has classified its behavior with temperature into two categories, *fragile* or *strong* glass. The fragility indicates a deviation of the viscosity behavior from Arrhenius law, given by

$$\eta(T) = A \exp\left(\frac{E_a}{RT}\right), \tag{2.40}$$

where A is a temperature-independent parameter, T the glass temperature and R the universal gas constant. Viscosity is assumed to be a thermally activated process where molecules have to jump an energy barrier in order to move [37], which is represented by the activation energy E_a. For a strong glass[1], i.e., a glass whose viscosity follows Arrhenius law, $\log_{10}\eta$ appears graphically as a straight line. However, most glass compositions demonstrate a clear deviation from this straight line, especially in the super-cooled region. A measure of this deviation around T_g is given by the fragility coefficient m:

$$m = \left.\frac{\partial \log_{10}\eta}{\partial\,(T_\mathrm{g}/T)}\right|_{T=T_\mathrm{g}}. \tag{2.41}$$

A large value of m corresponds to a large deviation from Arrhenius behavior. In the case of a fragile glass, an empirical temperature-dependent activation energy $E_a(T)$ seems more accurate to fit experimental data [38] and is given by

$$E_a(T) = E_a^* \frac{T}{T - T_\mathrm{c}}, \tag{2.42}$$

where E_a^* and T_c are two constants. This leads to the famous Vogel-Fulcher-Tamman (VFT) equation (mentioned in Section 2.2):

$$\log_{10}\eta(T) = \log_{10}\eta_\infty + \frac{B}{T - T_\mathrm{c}}.$$

This relation has been the most frequently used model in the literature for many decades and seems to be adequate in predicting the viscosity variation over the entire range of temperature from equilibrium to transition [39].

Nevertheless, the empirical nature of this relation led Mauro *et al.* [40] to propose a new viscosity law for liquid glass derived from the work of Adam-Gibbs [41] and based on thermodynamic laws:

$$\log_{10}\eta(T) = \log_{10}\eta_\infty + \frac{K}{T}\exp\left(\frac{C}{T}\right), \tag{2.43}$$

[1]Note that the use of the words fragile or strong may lead to ambiguities. Here, their meaning is related to viscosity and not to the brittleness of the material when a stress is applied.

called the Mauro-Yue-Ellison-Gupta-Allan (MYEGA) law. In Eq. (2.43), η_∞, K and C are parameters which are derived from thermodynamics. However, in practice, these parameters are fitted with experimental measurements. The value of η_∞ should be, in principle, the same as in the VFT model given by Eq. (2.43) because it is the viscosity at infinite temperature. But measurements are always performed on a finite temperature range leading to different values of η_∞. The major advantage of this model is to remove the singularity at $T = T_c$ and to increase the accuracy of the viscosity-temperature law at lower temperatures [40]. Moreover, its formulation is based on thermodynamics, removing thus some of the empiricism of the VFT model.

Limitation

The formulation of the viscosity law is not trivial and many basic questions are still open as highlighted by Mauro *et al.* [40]. The main difficulty is the form of the curve for temperatures below T_g, i.e. $\eta > 10^{15}$ Pa·s. The VFT model implies an infinite viscosity at $T \to T_c$, while the singularity occurs for a temperature equal to zero for Arrehnius and MYEGA models. Some authors [42, 43] have expressed some doubts related to this singularity at finite temperature T_c. According to Mauro *et al.* [40], the MYEGA model is a strong evidence against the existence of this divergence in glass-forming liquids.

On the other hand, the glass structure is out of equilibrium near the glass transition and depends on the thermal history. Because the viscosity depends on the structure, the formulation may differ significantly from the viscosity law at equilibrium. The previous relations, Eqs. (2.40), (2.9) and (2.43), are obtained under the assumption of *equilibrium* and do not take into account the information of structural deviation from equilibrium at transition. Formulations for non-equilibrium viscosity exist [44] but are not considered in this work.

Viscosity measurements

The viscosity has been measured experimentally by a coaxial cylinder viscometer over the temperature range from 800°C to 1400°C. The sample is heated in a platinum crucible from room temperature to 1400°C over five hours. Then, measurements are performed by decreasing the temperature by steps of 50°C until reaching 800°C. Over the glass transition region, a dilatometer was used instead of the viscometer. The principle is based on the dilatation of a glass sample during a cycle of temperature variation. Viscosity can be obtained from the measurement of dilatation. The error on the measurement for the viscometer is estimated to vary between 3% at 1300°C and 6% at 800°C and the error on the dilatomer points is less than 1%.

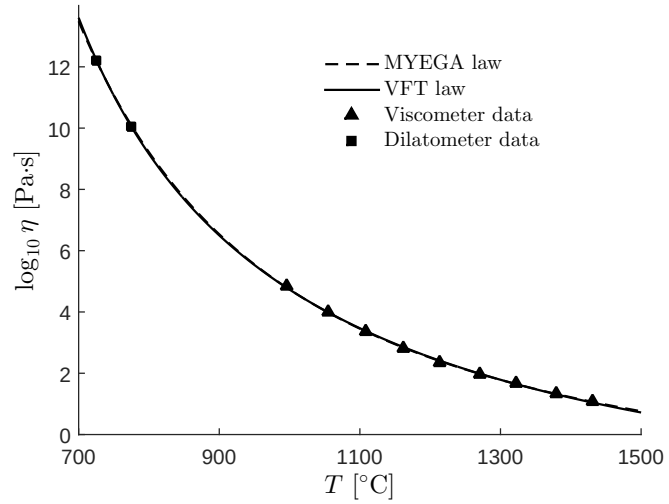

(a)

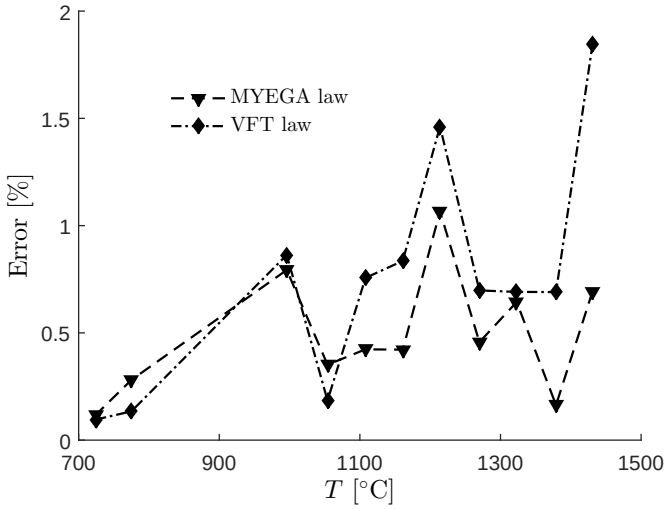

(b)

Figure 2.9: (a) Viscosity as a function of the temperature obtained by the MYEGA and VFT laws for the Advantex© composition. Experimental points from the viscometer and dilatometer measurements are also shown. (b) Relative error from curve fitting at the measurement points.

The measurement points can then be fitted to obtain the coefficients η_∞, B, T_c for the VFT law or η_∞, K and C for the MYEGA law. The fit is performed using the least square method on the log values of the viscosity.

Figure 2.9 shows the results of the regression including the relative error at the different measurement points, and Table 2.1 summarizes the temperature of the reference points. As illustrated in the figure, a gap in the measurement points is visible between 996°C and 775°C, which is due to the limitation in temperature of the two measurement devices.

Reference point	log η [Pa·s]	Temperature [°C]
Working point	2	1268
Softening point	6.6	895
Glass transition	12	730
Strain point	13.5	702

Table 2.1: Reference viscosity points and corresponding temperature for the Advantex© composition.

The VFT and MYEGA laws seem to be adequate to predict the viscosity-temperature dependence. The relative error at the measurement points show a maximal error of 2%. The lower error in the low temperature range stems from the fact that few points are available in this range. Overall, almost no difference is observed between the two laws. Moreover, the relative error is smaller than the measurement uncertainties. Therefore, all results shown in the following are based on the VFT model. Nonetheless, a specific section in Chapter 5 is dedicated to a discussion of the impact on the two viscosity laws in the case of modeling the fiber drawing process. The parameters considered for η_0, B and T_c are given in Table 2.2 further below.

2.4.2 Specific heat

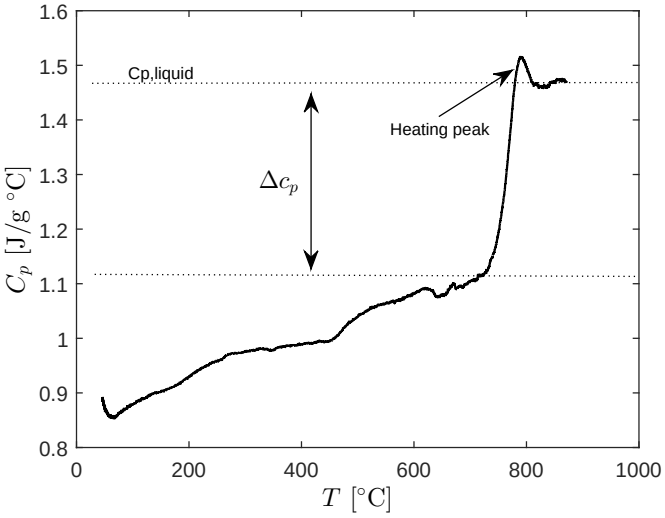

Figure 2.10: Measurement of the specific heat c_p as a function of the temperature in the glassy and transitional state for the Advantex© composition, obtained with a differential scanning calorimeter. The measurement error is approximately 3%.

The specific heat c_p measures the amount of energy required to increase the temperature of a material. The value of c_p depends on the glass composition and temperature. The measurements for temperatures above the transition were performed on a Calvet calorimeter, while a differential scanning calorimeter was used for the transition and glassy state. It has been shown that the variation of c_p with temperature is usually smaller than the precision of the measurement [45]. As a consequence, c_p is assumed to be constant within the liquid region. The value taken in this model is equal to 1.48 J/g°C with an uncertainty of 0.02 J/g°C (1.35%). However, a constant value is only valid in the liquid state since the specific heat decreases abruptly by a quantity $\Delta c_p \approx 0.324$ J/g°C during the transition and then slowly decreases with temperature in the glassy state. Figure 2.10 shows the measurements from the differential scanning calorimeter where the Δc_p is clearly visible. The measurement error was estimated to be about 3%. Note that the heating peak, as depicted in Fig. 2.10, is only a memory effect occurring when the sample is heated up from the glassy state. If the glass is cooled, the peak does not occur.

2.4.3 Density

The density ρ of a material is the mass per unit of volume. As the other properties, ρ depends on the composition and temperature. The variation of the volume with the temperature in the liquid state, i.e., the slope of the curve in Fig. 2.1, is due to [25]:

- variation of the vibrationnal mode of the molecules, denoted as α_{v},
- and variation of the structure, denoted as α_{s}.

The slope is thus written as

$$\alpha_{\mathrm{liq}} = \frac{1}{V}\left(\frac{\partial V}{\partial T}\right)_p = \alpha_{\mathrm{v}} + \alpha_{\mathrm{s}} = 4 \cdot 10^{-5}\ {}^{\circ}\mathrm{C}^{-1}. \tag{2.44}$$

where the values were measured by the beam bending method. The variation of the volume automatically gives the temperature behavior of the density, which is typically linear and can be written as

$$\rho(T) = \rho_{\mathrm{ref}}(1 - (\alpha_{\mathrm{liq}}(T - T_{\mathrm{ref}}))), \tag{2.45}$$

where $(T_{\mathrm{ref}}, \rho_{\mathrm{ref}})$ is a reference point taken at $T_{\mathrm{ref}} = 1300$°C. Additional experimental measurements of the density as a function of the temperature are thus needed within the liquid region and results are shown in Fig. 2.11. Density has been measured using Archimedes method, which is based on the determination of a weight of a platinum-rhodium sphere immersed into the molten glass at a given temperature. Fig. 2.11 includes

the linear regression from experimental data which has the following form

$$\rho(T) = a_\rho + b_\rho T \text{ Kg/m}^3, \quad \forall T > T_\text{g}, \tag{2.46}$$

where the constants a_ρ and b_ρ are given in Table 2.2. It is a reformulation of Eq. (2.45). Unfortunately, accounting for variable density in simulations would require specific numerical treatment. Therefore, all following results have been obtained assuming a constant density of 2470 kg/m^3 in all simulations.

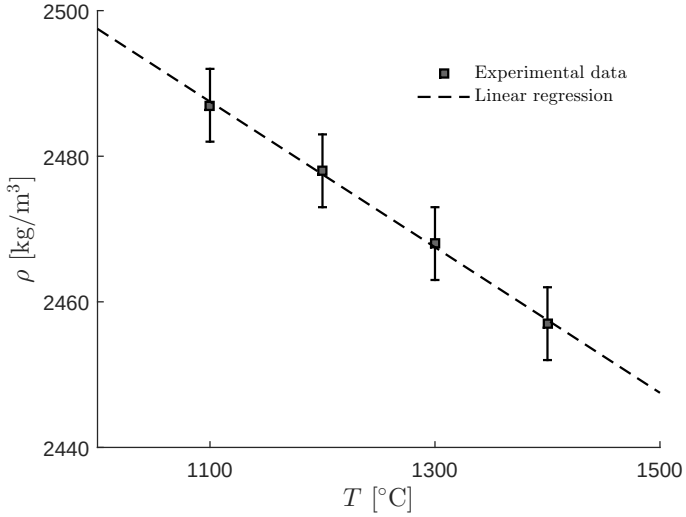

Figure 2.11: Density as a function of the temperature in the liquid state (Advantex© composition).

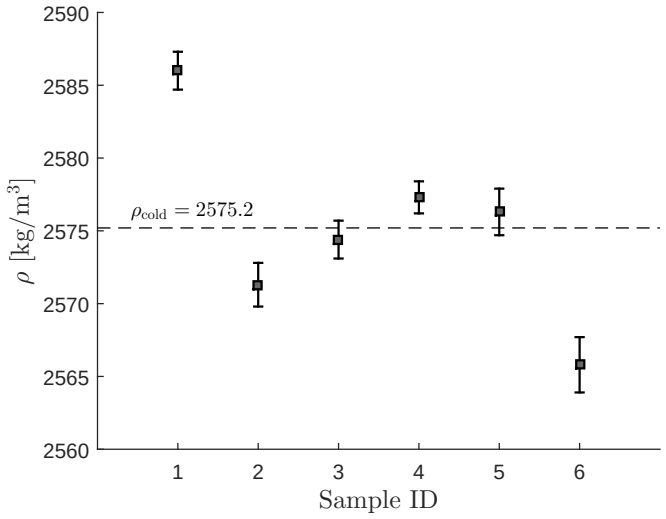

Figure 2.12: Measurement of the density of different fibers at room temperature (Advantex© composition).

The glass structure in the solid state depends on the cooling rate applied during transition. Because fiber drawing involves a much higher cooling rate ($\approx 10^5$ °C/s) compared to the usual cooling rate in laboratory (closer to 20°C/s), the density measurement at room temperature must be performed on actual fibers, rather than glass samples cooled in laboratory. Different samples have been used to capture the natural variability in cooling rates during the manufacturing process. The results are given for each sample including error bars in Fig. 2.12. The average density at room temperature is thus approximately

$$\rho_{cold} = 2575.2 \pm 6.7 \text{ kg/m}^3. \tag{2.47}$$

While the solid state value is not involved in the viscous model, this value is required for the calculation of different experimental parameters (e.g., mass flow rate), as discussed in Chapter 3.

2.4.4 Thermal conductivity

The thermal conductivity k measures the capacity of a medium to transport heat by conduction. In the molten glass, this quantity often includes the effect of internal radiation, and is called the Rosseland conductivity. However, this approximation is only valid under certain conditions, which are discussed in detail in Section 2.6. In the case of fiber drawing, the true thermal conductivity must be considered (i.e. without radiation). The only available data found for the true conductivity in the literature for a glass composition similar to Advantex© is for the E-glass. Manfrè [7] used a constant value of $k = 2.65$ W/mK, while Huynh and Tanner [9] worked with a conductivity equal to 1 W/mK. Lenoble [16] also took a constant value set at 1.8 W/mK. Similarly, Von Der Ohe [15] worked with constant values ($k = 3$ W/mK and $k = 2.2$ W/mK depending on the melt considered). Additionally, she found that the dependency on temperature is negligible in the fiber drawing process.

Fig. 2.13 shows the experimental measurements of the conductivity obtained with the flat disk method. In molten glass, the conductivity seems to increase when temperature decreases until the transition. Although the measurement uncertainty is large, the same order of magnitude is found as in the literature. The dependency with temperature between 800°C and 1350°C is calculated by a linear regression of the measured data, as shown in Fig. 2.13. The relation is expressed as

$$k(T) = a_k + b_k T \text{ W/mK}, \tag{2.48}$$

where the constants a_k and b_k are given in Table 2.2.

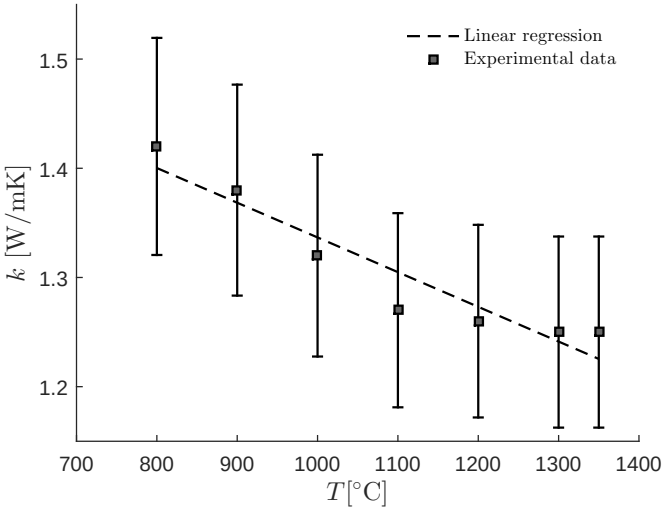

Figure 2.13: Measurement of the thermal conductivity for the Advantex© composition. The measurement error is estimated to be around 7%.

2.4.5 Surface tension

The surface tension of molten glass strongly depends on the glass composition, and more weakly on the temperature and level of OH in the melt. In addition, the chemical nature of the surrounding atmosphere may have an effect on surface tension.

In the study of the fiber glass drawing process, surface tension is often considered as a constant or even neglected. Nevertheless, Von der Ohe [15] found a temperature variation of about 0.02 N/m per 100°C based on measurements in the range of 1200°C to 1600°C, which led to the following expression: $\gamma(T) = 2 \cdot 10^{-4}T + 0.0864$, where T is in Kelvin leading to $\gamma(1145°\text{C}) = 0.37$ N/m. Similarly, Pye [45] reported a variation of the surface tension with temperature in the same range as Von Der Ohe. The error of the measurement is approximately 2%. As a consequence, the measurement has to be sufficiently accurate to capture the temperature dependency.

Some authors have studied the influence of the atmosphere on surface tension. A complete review can be found in the book of Pye [45]. Gases such as SO_2 or NH_3 are not present in the fiber drawing process, but water vapor in the atmosphere can lead to variations of surface tension. Measurements of surface tension should therefore ideally account for the air water content. Due to the difficulty of reproducing the exact conditions of the process, this effect has been neglected here, and measurements have been made in non-controlled atmosphere.

The method used is a sessile drop technique, which consists in measuring the contact angle of a drop of molten glass. The measurement is performed using image processing. However, the measurement is often dependent on the device and the error may be large.

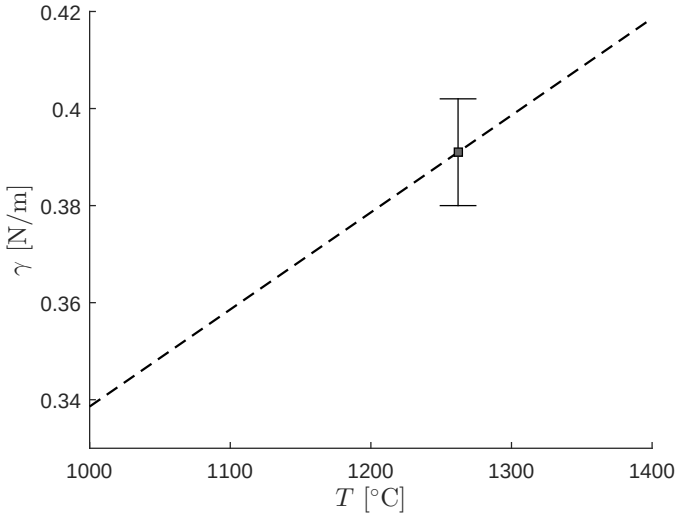

Figure 2.14: Measurement of the surface tension at 1262°C and the calculated linear dependency with temperature. The slope is equal to $2 \cdot 10^{-4}$ for the Advantex© composition.

A surface tension of

$$\gamma = 0.391 \pm 0.011 \text{ N/m} \quad \text{at } T = 1262^{\circ}\text{C}, \tag{2.49}$$

was measured. Using the temperature dependence found by Von der Ohe, the dependency on temperature is additionally modeled as

$$\gamma = a_\gamma + b_\gamma T \text{ N/m}, \tag{2.50}$$

where the constants a_γ and b_γ are given in Table 2.2. This relation is shown in Fig. 2.14.

2.4.6 Effective emissivity

The model developed in Section 2.2 assumes that the fiber is an opaque, diffuse and grey medium. The model thus involves only surface radiation as boundary condition (Eq. (2.25)). This is a strong approximation since glass is a semi-transparent medium. This topic is further discussed in Section 2.6. Nonetheless, using this approximation requires characterizing the surface emissivity ϵ_s.

The surface emissivity depends on the temperature, but also on the thickness of the medium because of the semi-transparent nature of glass. Gardon [46] in 1955 studied the emissivity for glass plates with different thicknesses. He found a decrease of emissivity from a value of 0.9 at room temperature to 0.3 at $T = 1573$ K. Moreover, the emissivity was found to decrease with thickness for a thickness below 15 cm. In the present case, the fiber thickness varies from 1-2 mm at the tip to 10 μm as final diameter. Based

on the work of Gardon, Huynh and Tanner [9] used a constant value $\epsilon_s = 0.272$ for E-Glass and Von Der Ohe [15] took a constant emissivity equal to $\epsilon_s = 0.3$. Purnode and Rubin [11] performed numerical simulations with a constant ϵ_s, but its exact value was not mentioned. Lenoble [16] used for the first time an emissivity that depends on temperature and fiber diameter r_s. The relation found is for the E-Glass composition, which is written as

$$\epsilon_s = \epsilon_0 \left(1 - e^{-\tau}\right), \tag{2.51}$$

where τ is the optical thickness of the glass, defined as

$$\tau = \left(7.774 + 5.49 \cdot 10^{-3}\, T\right) (4 r_s)^{0.175 + 2 \cdot 10^{-4}\, T}. \tag{2.52}$$

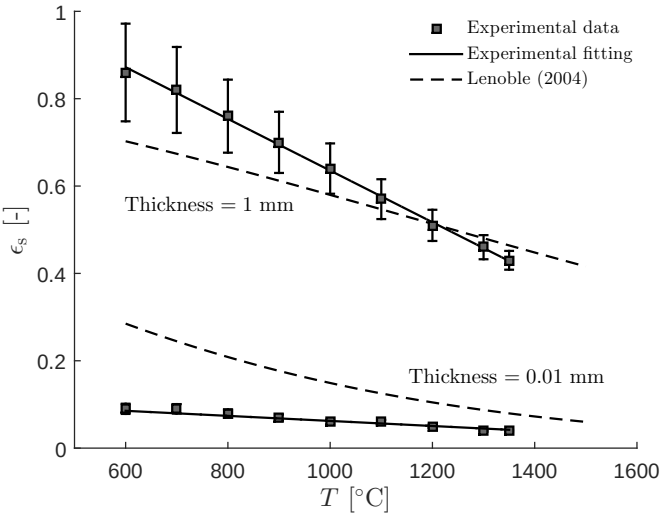

Figure 2.15: Measurement of the emissivity ϵ_s as a function of the temperature and the thickness of the medium for the Advantex© composition. The solid lines represent the fitting of the experimental data through Eq. (2.53). The relation proposed by Lenoble [16] (Eq. (2.51)) is also shown as dashed lines for comparison.

Measurements were performed on Advantex© glass for different diameters and temperatures. The fitting of the data with respect to these two quantities is achieved through the relation

$$\epsilon_s = (a_\epsilon T + b_\epsilon)\left[1 - e^{c_\epsilon r_s}\right], \tag{2.53}$$

where the constants a_ϵ, b_ϵ and c_ϵ are given in Table 2.2[1]. Results are presented in Fig. 2.15 where the experimental data is compared with Eq. (2.51) and Eq. (2.53). The interpolation function proposed here (Eq. 2.53) clearly fits much better the experimental data for

[1]The units of temperature and radius are respectively °C and m.

the Advantex© than that proposed by Lenoble (Eq. 2.51).

It is important to note that, because glass is a semi-transparent medium, measurements of surface emissivity cannot isolate the surface radiation from the radiation coming from the bulk. Such measurements should therefore be seen as measurements of an effective emissivity, rather than a pure surface emissivity.

As a result, the influence of the thickness is a consequence of the radiation from the bulk passing through the surface. The quantity ϵ_s is thus called *effective emissivity* in this work. Despite the fact that the effective emissivity clearly depends on the temperature and thickness (see Fig. 2.15), it is approximated here as a constant. Moreover, in the region where the contribution of radiation is important for cooling, i.e., from 1300°C at $z = 0$ to 1200°C at $z = 5$ mm (see Section 5.1.2), the increase of ϵ_s due to the temperature decrease is partially compensated by the decrease of ϵ_s due to the decrease of the thickness (i.e., fiber diameter). This is illustrated in Fig. 2.16, which shows the variation of the effective emissivity along the fiber, where ϵ_s was computed from Eq. (2.53) using the temperature T_s and fiber radius r_s from a simulation using the two-dimensional axisymmetric model. Averaging over the range where radiation dominates leads to a value $\epsilon_s = 0.4$. The error introduced by approximating ϵ_s as constant is thus small. The sensitivity of the results on the value of this constant and a comparison between the effective emissivity approach and the full model including internal radiation is discussed in Section 5.4.4.

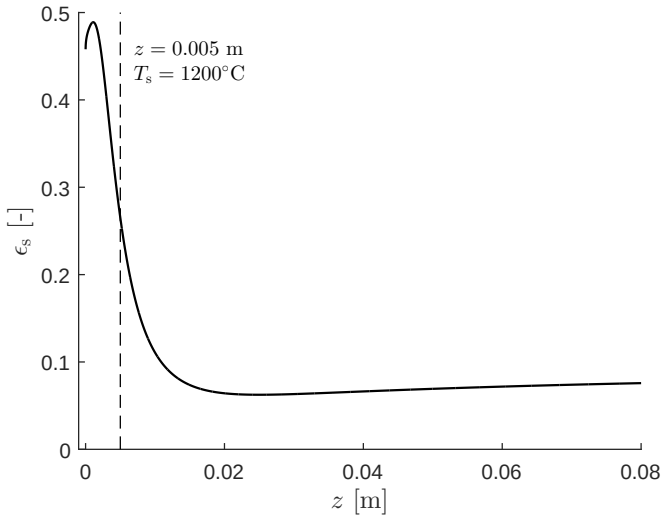

Figure 2.16: Emissivity variation as a function of the distance from the tip exit using Eq. (2.53) and the solution from Section 5.1.2. The region from $z = 0$ to the dashed line corresponds to the region where radiative cooling is dominant.

2.4.7 Summary of the material properties of glass

Table 2.2 summarizes all material properties used in the one- and two-dimensional models (i.e., molten glass) for the Advantex©. For each property, both a temperature dependence and a constant value are given. The temperature dependence is characterized by the equation used to model it, the value of the parameters obtained from fitting measurement data, and its range of validity. As some simulations neglect temperature variations of material properties, a constant value is also given, which has been defined as the corresponding property evaluated at $T = 1300°C$ (i.e., the tip temperature).

Glass properties	*Constant value*	*Temperature dependence*		
	$T = 1300°C$	Parameters	Eq.	Range [°C]
Viscosity η [Pa·s]	-	$\eta_\infty = -3.075$ $B = 5262.4$ $T_c = 402.3$	(2.9)	[725-1430]
Specific heat c_p [J/kgK]	1480	-	-	[800-1400]
Density ρ [kg/m^3]	2470	$a_\rho = 2597.5$ $b_\rho = -0.1$	(2.46)	[750-1400]
Conductivity k [W/mK]	1.27	$a_k = 1.65$ $b_k = -3.17 \cdot 10^{-4}$	(2.48)	[800-1350]
Surface tension γ [N/m]	0.39	$a_\gamma = 0.1386$ $b_\gamma = 2 \cdot 10^{-4}$	(2.50)	[800-1400]
Effective emissivity ϵ_s [-]	0.4	$a_\epsilon = -5.915 \cdot 10^{-4}$ $b_\epsilon = 1.227$ $c_\epsilon = -2.062 \cdot 10^4$	(2.53)	[600-1350]

Table 2.2: Summary of the glass properties of the melt used in the viscous models for the Advantex© composition.

2.5 Model of the surrounding air

As mentioned previously, the use of Kase and Matsuo correlation (Eq. (2.23)) to estimate the convective cooling is questionable. In order to assess its accuracy a simple model of the ambient air flow is also considered. The objective is to compute the velocity and temperature fields of the entrained air in the vicinity of the fiber. The heat flux at the surface and the corresponding convective heat transfer coefficient can then be obtained from the temperature profile in the thermal boundary layer.

As the fiber is drawn at rather large velocity, the entrained air is in a turbulent state. To limit the computational cost, a Reynolds-Averaged Navier-Stokes (RANS) approach is favored. The Mach number being sufficiently low, the ambient air is considered as incompressible.

2.5.1 Governing equations

Using Reynolds decomposition, the random turbulent velocity v_i, pressure p and temperature T fields can be expressed as the sum of a mean value and some fluctuation around this mean, i.e., $v_i = \bar{v}_i + v_i'$, $p = \bar{p} + p'$, $T = \bar{T} + T'$, respectively, where $\bar{\cdot}$ represents the averaged quantity, and $\cdot'$ the random fluctuation. Introducing this decomposition into the incompressible Navier-Stokes equations and averaging leads to the RANS equations for the mean quantities:

$$\partial_i v_i = 0, \tag{2.54}$$

$$v_j \partial_j v_i = -\frac{1}{\rho_\mathrm{a}} \partial_i p + \mu_\mathrm{a} \nabla^2 v_i - \partial_j \overline{v_j' v_i'}, \tag{2.55}$$

$$v_i \partial_i T = D_a \nabla^2 T - \partial_i \overline{v_i' T'}, \tag{2.56}$$

where μ_a is the dynamic viscosity of air, D_a its thermal diffusivity and the overbar indicating an average value has been omitted for the transported quantities to simplify the notation. The RANS equations are unclosed since the Reynolds stress $-\overline{v_j' v_i'}$ and turbulent temperature flux $\overline{v_i' T'}$ are unknown. These two terms are here modeled through an eddy viscosity and eddy diffusivity assumption using the realizable k-ϵ model, an improved version of the classical k-ϵ model [47].

2.5.2 Computational domain and boundary conditions

Similarly to the fiber, the air flow is considered axisymmetric. Figure 2.17 illustrates the computational domain. It is divided into two sub-domains: on the left the fiber itself that is computed with the axi-symmetric two-dimensional model described above, and on the

right the ambient air region in which the RANS equations are solved. It is important to emphasize that the solutions (velocity and temperature fields) in the fiber and in the ambient air depend on each other. Therefore, the two simulations, which use two different solvers as described in Chapter 4, must be coupled.

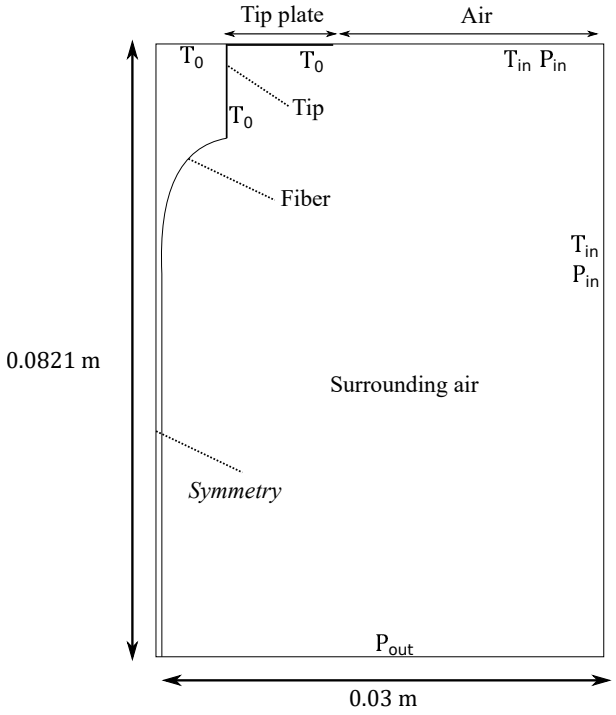

Figure 2.17: Computational domain of the surrounding air and the forming fiber.

For the ambient air domain, the upper boundary is divided into two sections, corresponding to the bushing plate and to the air inflow. The boundary representing the bushing plate has a length of 3.4 mm, which corresponds to the mono-filament bushing (see Chapter 3). It is considered as a no-slip wall at uniform temperature T_0, similarly to the tip wall. On the other hand, the inflow is set at a constant pressure p_{in} and temperature T_{in}. Similarly, the right boundary corresponds to an inflow at a constant pressure p_{in} and temperature T_{in}. The bottom boundary is considered as an outflow. To mimic the low pressure area present in the industrial process, and to ensure that no recirculation takes place across this boundary, a constant pressure $p_{\text{out}} < p_{\text{in}}$ is imposed. The continuity of velocity, stress, temperature and heat flux is imposed at the fiber surface by coupling the two simulations. The boundary conditions for the axisymmetric fiber model is thus adapted accordingly. The inflow conditions for the turbulence quantities correspond to a low level of turbulence (i.e., 5% turbulence intensity and a turbulent viscosity ratio equals to 10). As it is shown in Chapter 5, the impact of the inflow boundary conditions is negligible as most of the air velocity and temperature variations occur in a a very thin

region next to the fiber.

This model could be further improved by considering different turbulence models and more realistic boundary conditions. Moreover, the influence of other setup elements (fin-shields, air conditioning system, etc.) could also be added. Nevertheless, the aim of this model is mostly to assess the accuracy of the empirical correlation, so that the present level of fidelity is deemed sufficient.

2.6 Semi-transparent model

The models derived in Section 2.2 and Section 2.3 assume that the glass is an opaque diffuse grey medium, i.e. all radiative phenomena occur at the surface of the fiber and do not depend on the wavelength and direction. Consequently, heat transfer within the glass is only due to conduction and convection. However, molecules internal to the glass can participate to the radiation phenomenon by emitting and absorbing photons in a certain range of wavelengths. The consequence is an additional heat transfer mechanism inside the glass. Depending on the glass composition and the size of the medium, the corresponding internal radiative heat flux may be as large as the conductive heat flux. While this aspect is critical for glass furnaces, it is more ambiguous in the glass forming process because of the small dimensions of the fiber. Several studies of different glass forming processes, such as flat glass tempering [48], glass sagging [49] or optical glass fiber drawing [50], have demonstrated the importance of accounting for internal radiation to obtain the correct temperature field. In the case of the fiber drawing process, all studies have neglected internal radiation because of the small fiber dimensions and the complexity of numerical simulations. Nevertheless, some authors recognized the importance of investigating this problem, such as Glicksman [5] and Lenoble [16].

A detailed model for internal radiation is presented here. The objective is to determine quantitatively the impact of internal radiation in the fiber drawing process. This section is dedicated to describing the physical models for internal radiation in semi-transparent media, including appropriate boundary conditions and material properties. The different radiative regimes are also discussed. Results are presented in Chapter 5.

2.6.1 Radiative regimes

The convection and conduction mechanisms are local phenomena occurring at the atomic scale ($\sim 10^{-9}$ m), while the scale of radiative phenomena (i.e., the photon mean-free-path length) ranges between $\sim 10^{-9}$ and $\sim 10^{10}$ m. This scale is linked to the capacity of the medium to interact with an electromagnetic wave crossing it, which is generally a function

of the wavelength λ. As a result, the importance of internal radiation within a medium is a function of the scale and material considered.

A macroscopic quantity measuring the emission and the absorption of photons by the molecules of the medium is the absorption coefficient κ_λ. It represents approximately the inverse photon mean-free-path and is thus an inverse length scale with units m^{-1}. Its value strongly depends on the wavelength. Three different situations can occur when a medium is exposed to an irradiation:

- $\kappa_\lambda = 0$: the in-coming radiative energy is not affected when traveling through the medium, that is in this case called *transparent*;
- $\kappa_\lambda = \infty$: the in-coming radiative energy is completely and instantaneously absorbed at the surface of the medium, that is then called *opaque*;
- otherwise: the *semi-transparent* medium absorbs and emits radiation leading to a variation of the radiative energy.

Strictly speaking, all materials are semi-transparent. Opaque and transparent are only two limit cases. However, for some scales and values of the absorption coefficient, the assumption of a transparent or opaque medium is adequate, which simplifies the problem as it avoids the complex treatment of internal radiation. A common example is a glass window, which is transparent for typical thicknesses. But, if the thickness of the window increases, it becomes more and more difficult to see the light coming from the outside, until the point where the thickness is so large that the light from the outside is not visible any longer. At this point, the window can be considered to be opaque. As a consequence, the length, or the thickness, must be taken into account to determine if the medium should be treated as transparent, opaque or semi-transparent. This is measured by the optical thickness

$$\tau_\lambda = \int_0^s \kappa_\lambda ds \approx \kappa_\lambda l_{\mathrm{rad}}, \tag{2.57}$$

assuming κ_λ to be independent of the length scales considered and l_{rad} a characteristic scale. The optical thickness is thus a non-dimensional parameter that measures the ratio between a characteristic length scale l_{rad} of the medium and the average distance traveled by a photon $(1/\kappa_\lambda)$. The estimation of τ_λ thus gives an information on the radiative regime of the medium. Three main regimes can be distinguished:

Optically thin $\tau_\lambda \ll 1$: The scale is much smaller than the distance required to attenuate the in-coming radiation. This situation can occur when l_{rad} is very small, even if κ_λ is high, or for very small values of κ_λ even if the scale is large. The electromagnetic waves traveling within the medium interact only weakly with the

particles over the distance traveled. Their loss or gain of energy are very small. In the limit of a very small τ_λ, the medium can be assumed to be transparent.

Optically thick $\tau_\lambda \gg 1$: In this case, l_{rad} and/or κ_λ are very large. The electromagnetic waves interact many times with the emission and absorption of the particles of the medium over the distance traveled. The emission of the particles is rapidly absorbed by the neighbor molecules, with the consequence of a rapid attenuation of the radiative information along the path. The radiation in this regime tends towards a diffusion process, as it has been mathematically demonstrated [45, 51, 52]. In the limit of very high τ_λ, the medium can be considered to be opaque.

Intermediate $\tau_\lambda \approx 1$: The medium must be considered as semi-transparent in order to accurately characterize the radiative transfer. This situation occurs mostly in the case of glass forming processes, such as for TV panels, blow molding and many others.

2.6.2 Semi-transparent window of glass

For typical length scales involved in glass forming processes ($\sim 10^{-1} - 10^{-2}$ m), the range of wavelengths in which glass behaves as a semi-transparent medium is in the infrared. At lower λ, the glass can be assumed transparent, while at higher λ, it usually behaves as an opaque medium and radiation is modeled as surface radiation. In order to determine the radiative regime in the fiber drawing process, the absorption coefficient is first analyzed, and then the optical thickness is estimated by considering typical length scales of the forming fiber.

The absorption coefficient κ_λ, has been measured for the Advantex© glass for different wavelengths and at two temperatures. The results are shown in Fig. 2.18. Two peaks at $\lambda = 1.1$ μm and $\lambda = 2.9$ μm are visible. The first peak, occurring in the smaller wavelength region, is due to the level of Fe and Cr in the melt [53], while the second comes from OH molecules. Although the height of the first peak is much lower than the second one, it occurs at wavelengths where the emissive power of a black body is higher. Consequently, the energy of the particle emission can be important even if κ_λ is smaller. The data also shows a small influence of temperature on this coefficient. The height of the peaks decreases as the temperature increases, which was also observed by Faber [53] for borosilicate glass.

In order to determine the radiative regime in the fiber glass forming process, the scales must be considered in addition to the absorption coefficient. The forming fiber involves different length scales. The radial length, i.e. fiber diameter $2r_s$, varies from the tip

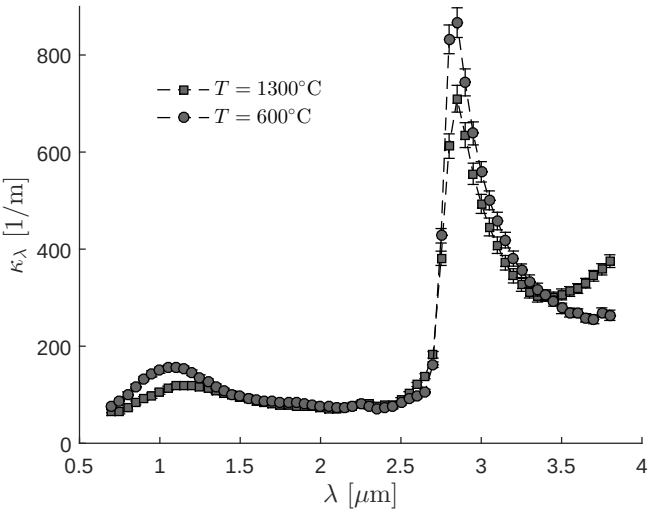

Figure 2.18: Absorption coefficient as a function of the wavelength at two different temperatures for the Advantex©. The symbols represent the measured values.

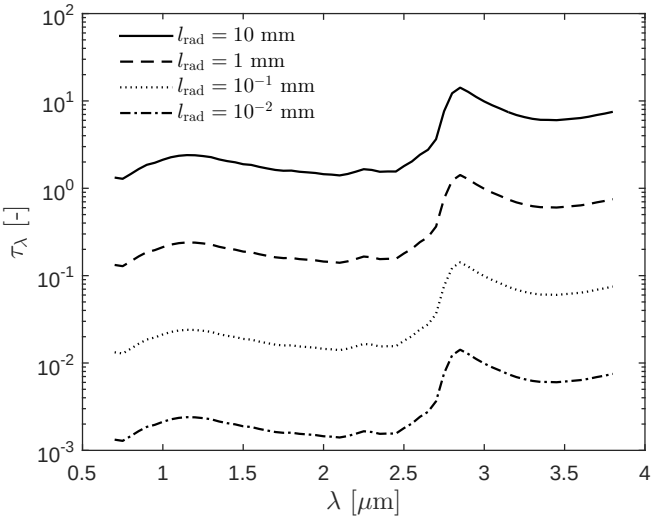

Figure 2.19: Optical thickness as a function of the wavelength at different values of l_{rad} representing both the radial length from the tip diameter (≈ 1 mm) to the final diameter ($\approx 10^{-2}$ mm), and the axial length (≈ 10 mm).

diameter (≈ 1 mm) to the final diameter ($\approx 10^{-2}$ mm). Furthermore, the axial length at the symmetry line has a magnitude of a few centimeters. Figure 2.19 illustrates the optical thickness as a function of the wavelength for these different characteristic lengths. Near the tip, $\tau_\lambda \approx 0.1-1$ for the radial direction and $\tau_\lambda \approx 1-10$ for the axial direction. In this particular region, the glass is semi-transparent according to the definition presented in the previous section. Nevertheless, as the fiber radius decreases, τ_λ becomes very small.

When the fiber reaches its final diameter, the radiative regime is close to be transparent. In conclusion, a semi-transparent model to characterize the radiation is justified for the upper region of the forming fiber, at least in this range of wavelengths. Nevertheless, the model assumes a semi-transparent in the entire region of the fiber. In particular, the radiative regime as a function of the wavelength can be modeled as follows:

- At wavelengths lower than 0.7 μm, the only remaining mechanism to emit and absorb a photon is due to the electronic excitation (i.e. change in the orbit of the electron) [53], while it is due to vibrationnal transitions in the range of $\lambda = 0.7 - 3.8$ μm. Since the energy required for electronic excitation is very high, it occurs at very short wavelengths (< 1 μm) leading to isolate vertical lines in the absorption coefficient spectrum [53][1]. However, the temperature needed to reach such an amount of energy is not available in the fiber drawing process and the black body intensity tends to zero in this range of wavelength. For these reasons, the glass is assumed transparent below this wavelength and the electronic excitation is neglected.

- On the other hand, glass tends to be opaque at larger wavelengths. In this opaque region, radiation is only considered as a flux at the surface. Like for a transparent medium, the radiative energy in the medium does not contribute to internal energy variations. An opaque emissivity $\epsilon_{\mathrm{op},\lambda}$ depending on temperature is thus used, which approximates the part of the radiative flux escaping the medium to the surrounding environment. The transition from a semi-transparent to opaque case is often considered at one wavelength, called the cutting wavelength λ_c. In reality, the transition occurs continuously when $\tau_\lambda \to \infty$. As a result, the choice of λ_c depends both on the scale and the absorption coefficient. Different cutting wavelengths for glass can be found in the literature, such as $\lambda = 6$ μm [54], $\lambda = 4.8$ μm [55] or $\lambda = 8$ μm [50]. For wavelengths above λ_c, these authors consider $\kappa_\lambda = \infty$. Unfortunately, measurements data of the absorptivity coefficient are not available for wavelengths above $\lambda = 3.8$ μm. This wavelength is thus taken as the cutting wavelength above which glass is considered to be opaque. Measurements of the opaque emissivity are shown in Fig. 2.20. In the opaque region, a constant opaque emissivity is used, which is obtained by averaging the measurement data over the wavelengths.

- Finally, the semi-transparent window is defined from $\lambda = 0.7$ to 3.8 μm.

[1]The measurements, represented in Fig. 2.18, do not provide data for the range below 0.7 μm.

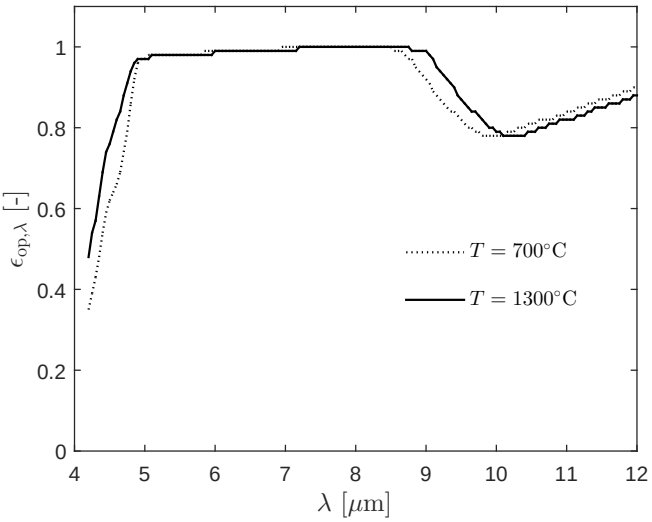

Figure 2.20: Opaque emissivity $\epsilon_{\mathrm{op},\lambda}$ as a function of the wavelength in the opaque region of the spectrum for Advantex© glass.

2.6.3 Equation of radiative transfer

Within this semi-transparent window, the divergence of the radiative heat flux $\dot{\mathbf{q}}_{\mathrm{r}}$ in the energy equation, Eq. (2.3), is non-zero. In order to calculate this flux, an additional equation is needed based on the conservation of radiative energy. This section focuses on developing this equation.

Absorption and emission

The quantity typically used to describe radiation in a semi-transparent medium is the *spectral radiative intensity* $I_\lambda(\mathbf{s})$, which is the energy at one specific wavelength λ per unit of time, solid angle and unit area normal to the ray. It depends on the direction of the ray as described by the unit vector $\mathbf{s}$. When radiation passes trough an element of a participating medium, its beam intensity is attenuated by absorption and scattering. At the same time, it can gain intensity by emission and scattering from other directions intercepting the beam. In the case of a glass material, scattering can be neglected in comparison to emission and absorption [48, 50, 55, 56].

Considering the intensity $I_\lambda(\mathbf{r}, \mathbf{s})$ at position $\mathbf{r}$, traveling in a direction $\mathbf{s}$ within an element of volume ds at constant temperature T, the energy d$I_{\mathrm{abs},\lambda}$ lost due to absorption is expressed as

$$\mathrm{d}I_{\mathrm{abs},\lambda} = -\kappa_\lambda I_\lambda \mathrm{d}s, \tag{2.58}$$

which is proportional to the magnitude of the incoming energy I_λ. The proportionality

factor κ_λ is the absorption coefficient. If only absorption is considered, the solution of this equation shows that the beam intensity decreases exponentially with the distance traveled in the medium. The higher κ_λ is, the more attenuated the beam is in the medium. A transparent medium thus corresponds to $\kappa_\lambda = 0$ while the opaque case corresponds to $\kappa_\lambda \to \infty$.

On the other hand, the gain of energy due to the spontaneous emission of the molecules in the same direction $\mathbf{s}$, $\mathrm{d}I_{\mathrm{em},\lambda}$, is proportional to the intensity of a black body $I_{\mathrm{b},\lambda}$. This is given by

$$\mathrm{d}I_{\mathrm{em},\lambda} = \kappa_\lambda n_{\mathrm{g}}^2 I_{\mathrm{b},\lambda} \mathrm{d}s, \tag{2.59}$$

where the proportionality constant involved is again the absorption coefficient κ_λ. It can be demonstrated that the proportionality coefficient is exactly the same for the absorption and emission mechanisms [51]. Additionally, n_{g} is the index of refraction of the glass, which is a function of the glass composition. Note that, in general, the index of refraction also depends on the glass structure, and thus on its thermal history during transition. However, this is not relevant here, as radiation only plays a role at high temperature in the liquid state, before transition. Finally, a dependence on the wavelengths may exist but, unfortunately, only grey and constant values have been measured for the Advantex© glass composition. The value is assumed constant in the following and equal to $n_{\mathrm{g}} = 1.56$.

Overall balance

The balance of these effects over the infinitesimal volume $\mathrm{d}s$ leads to the following relation

$$\frac{\partial I_\lambda}{\partial s}(\mathbf{r}, \mathbf{s}) = \kappa_\lambda n_{\mathrm{g}}^2 I_{\mathrm{b},\lambda} - \kappa_\lambda I_\lambda(\mathbf{r}, \mathbf{s}). \tag{2.60}$$

This equation is called the *Radiative Transfer Equation* (RTE). The intensity field within the medium is thus obtained by solving this equation for each wavelengths and directions. The radiative heat flux is then calculated by integrating the intensity over all directions and wavelengths

$$\dot{\mathbf{q}}_{\mathrm{r}} = \int_0^\infty \int_{4\pi} I_\lambda(\mathbf{r}, \mathbf{s}) \mathbf{s} \mathrm{d}\Omega \mathrm{d}\lambda, \tag{2.61}$$

where Ω is the solid angle. The heat flux is then used in Eq. (2.3) to calculate the temperature field. Because the black body intensity in Eq. (2.59) depends on the temperature, Eqs. (2.60) and (2.3) are coupled and must be solved iteratively.

From Eq. (2.60), the different radiative regimes can be highlighted and explained in more details:

Optically thin $\tau_\lambda \ll 1$: When $\kappa_\lambda \to 0$, the gradient of the intensity along a path is very small. The solution can be calculated by considering a linear variation of the

intensity in the medium. In the limit of $\kappa_\lambda = 0$, the intensity gradient is equal to zero leading to a constant flux within the medium, which is the definition of a transparent medium.

Optically thick $\tau_\lambda \gg 1$: In this cas, the intensity can be developed into a Taylor series related to the direction $\mathbf{s}$. Since $\tau_\lambda \gg 1$, only the linear term of the development is kept. The calculation of the divergence of the radiative flux leads to a diffusion form, similar to conduction. This form is called *Rosseland approximation* [57]. It is a powerful approximation since the RTE can then be replaced by an effective conductivity k_{ross} added to the thermal conductivity k in the energy equation (2.3). This is why this form is frequently used, especially in the modeling of glass furnaces. Note that the radiative conductivity k_{ross} scales with T^3. Finally, it can be shown that if the absorption coefficient tends to infinity, the rosseland conductivity tends to zero, i.e. the medium is thus opaque. In this case, the in-coming radiation is instantaneously absorbed and $I_\lambda = I_{\text{b},\lambda}$ within the medium. The divergence of the radiative flux is thus equal to zero. At the surface, the opaque emissivity represents the part of the black body intensity escaping from the medium, and its value depends on the refractive index (see Section 2.6.4).

Intermediate $\tau_\lambda \approx 1$: The full problem must be solved considering the RTE without approximation.

2.6.4 Boundary conditions

The RTE, Eq. (2.60), requires boundary conditions. In fiber drawing problems, there are two types of surface delimiting the domain: an opaque wall at the tip, and a semi-transparent interface between glass and air. Because radiation is not simply a surface phenomenon, the boundary condition at the interface, Eq. (2.25) for the energy equation (2.3), has to be modified accordingly. Specifically, the fiber is still opaque for a certain range of wavelengths, where the radiation is a surface phenomenon. The radiative flux in this range must be considered in addition to the boundary conditions of Eq. (2.60). Additionally, an insulated inlet and outlet are prescribed, while a condition of symmetry is used at the symmetry line. An overview of the boundary conditions is shown in Fig. 2.21.

Tip wall - Opaque boundary

The tip wall is considered as an opaque boundary. It emits itself radiative intensity and reflects and absorbs radiative intensity from the glass. The emission is given by the emission of a black body at the temperature of the wall multiplied by the emissivity of

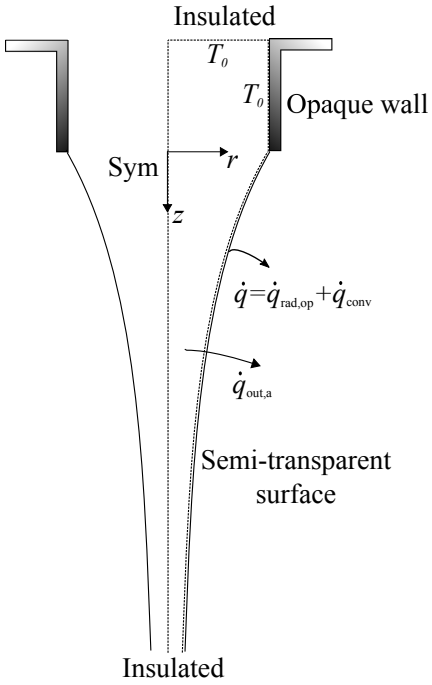

Figure 2.21: Overview of the radiative boundary conditions: radiative flux from the surface in the opaque range of wavelengths $\dot{q}_{\mathrm{rad,op}}$, and radiative flux in the bulk from the semi-transparent part of the spectrum $\dot{q}_{\mathrm{out,a}}$.

the tip surface. The surface is assumed diffuse and grey. Because surfaces are generally not polished, specular surfaces are rarely considered for glass [50, 55].

The intensity leaving the wall is equal to the sum of the reflected intensity and the intensity emitted by the wall, as shown in Fig. 2.22. The boundary condition is thus written as

$$I(\mathbf{r}_w, \mathbf{s}) = \epsilon_{\mathrm{pt}}(\mathbf{r}_{\mathrm{w}}) I_b(\mathbf{r}_{\mathrm{w}}) + \frac{\rho_{\mathrm{rf,pt}}(\mathbf{r}_{\mathrm{w}})}{\pi} \int_{\mathbf{n}\cdot\mathbf{s}<0} I(\mathbf{r}_{\mathrm{w}}, \mathbf{s}') \, |\mathbf{n}\cdot\mathbf{s}| \, \mathrm{d}\Omega', \tag{2.62}$$

where $\mathbf{r}_w$ is the vector position of the boundary and $\mathbf{n}$ the normal to the surface pointing out of the domain, and $\epsilon_{\mathrm{pt}}(\mathbf{r}_{\mathrm{w}})$ and $\rho_{\mathrm{rf,pt}}(\mathbf{r}_{\mathrm{w}})$ are the grey emissivity and reflectivity of the surface, respectively. It is assumed that the surface properties are constant along the tip wall, so that $\epsilon_{\mathrm{pt}}(\mathbf{r}_{\mathrm{w}}) = \epsilon_{\mathrm{pt}}$ and $\rho_{\mathrm{rf,pt}}(\mathbf{r}_{\mathrm{w}}) = \rho_{\mathrm{rf,pt}}$. Finally, the flux leaving the surface in all directions is calculated as

$$q_{\mathrm{out}} = n_{\mathrm{g}}^2 \epsilon_{\mathrm{pt}} \sigma T^4 + (1 - \epsilon_{\mathrm{pt}}) q_{\mathrm{in}}. \tag{2.63}$$

The first term represents the emission and the second the reflection, where the incoming flux q_{in} is given by

$$q_{\mathrm{in}} = \int_{\mathbf{n}\cdot\mathbf{s}<0} I(\mathbf{r}_{\mathrm{w}}, \mathbf{s}') \, |\mathbf{n}\cdot\mathbf{s}| \, \mathrm{d}\Omega'. \tag{2.64}$$

Note that in the case of a non-grey model (i.e. the parameters depend on the wavelength), these relations are calculated for each wavelength. The total intensity is then calculated as the integral over the spectrum of intensities.

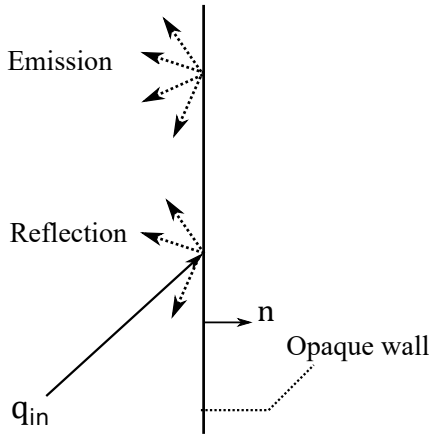

Figure 2.22: Representation of the radiative boundary condition for a diffuse opaque wall where q_{in} is the incoming flux given by Eq. (2.64). The diffuse reflection of q_{in} and emission of the wall are also represented.

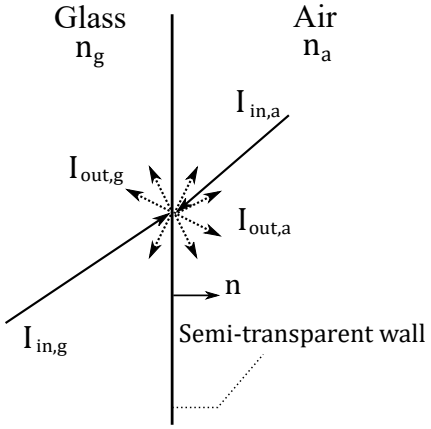

Figure 2.23: Representation of the radiative boundary condition for a diffuse semi-transparent wall. The quantities $I_{\text{in,g}}$ and $I_{\text{in,a}}$ are respectively the incoming intensity from the glass with a refractive index n_{g} and from the air, while $I_{\text{out,g}}$ is the sum of the reflected intensity from the glass and the transmitted intensity from the air. Finally, $I_{\text{out,a}}$ is the sum of the reflected intensity from the air and the transmitted intensity from the glass.

Free surface - Semi-transparent boundary

The free surface of the fiber is considered as a semi-transparent surface where a part of the bulk radiation passes trough the surface. Similarly, the radiation from the surrounding

environment can penetrate into the fiber. A schematic view of the semi-transparent boundary is shown in Fig. 2.23. As a diffuse surface is also assumed here, the interfacial reflectivity is independent of the direction **s** and is only a function of the ratio of the refractive indices of the air and the glass medium, $n_{\text{ratio}} = n_{\text{g}}/n_{\text{a}}$. The reflectivity for a diffuse internal surface to air, called $\rho_{\text{rf,g}}$, is given by [55]

$$\rho_{\text{rf,g}} = 1 - \frac{1 - \rho_{\text{rf,a}}}{n_{\text{ratio}}^2}, \tag{2.65}$$

where $\rho_{\text{rf,a}}$ is the reflectivity for a flux incident to the diffuse surface from the air medium given by Richmond [58] as

$$\begin{aligned}\rho_{\text{rf,a}} = \frac{1}{2} + \frac{(3n_{\text{ratio}}+1)(n_{\text{ratio}}-1)}{6\left(n_{\text{ratio}}+1\right)^2} &+ \frac{n_{\text{ratio}}^2\left(n_{\text{ratio}}^2-1\right)^2}{\left(n_{\text{ratio}}^2+1\right)^3}\ln\left(\frac{n_{\text{ratio}}-1}{n_{\text{ratio}}+1}\right) \\ &- \frac{2n_{\text{ratio}}^3\left(n_{\text{ratio}}^2+2n_{\text{ratio}}-1\right)}{\left(n_{\text{ratio}}^2+1\right)\left(n_{\text{ratio}}^4-1\right)} \\ &+ \frac{8n_{\text{ratio}}^4\left(n_{\text{ratio}}^4+1\right)}{\left(n_{\text{ratio}}^2+1\right)\left(n_{\text{ratio}}^4-1\right)^2}\ln(n_{\text{ratio}}).\end{aligned} \tag{2.66}$$

Assuming a surface which does not absorb the radiative flux, the transmission is deduced from Eq. (2.65) and Eq. (2.66):

$$\tau_{\text{tr,g}} = 1 - \rho_{\text{rf,g}}, \tag{2.67}$$

$$\tau_{\text{tr,a}} = 1 - \rho_{\text{rf,a}}. \tag{2.68}$$

Figure 2.24 shows the evolution of the transmissivity and reflectivity at the surface as a function of n_{ratio}. An increase of this ratio causes the decrease of the transmitted radiative flux to the surrounding air and increases the reflection. The value of the refractive index of the air is taken as $n_{\text{a}} = 1$ so that the ratio is equal to the refractive index for glass $n_{\text{ratio}} = n_{\text{g}} = 1.56$. The values for the reflectivity and transmissivity for the internal surface (glass-to-air) are given in Table 2.3.

As a result, the intensity $I_{\text{out,g}}$ leaving the internal surface into the glass is the sum of the reflective flux from $q_{\text{in,g}}$ with the transmitted flux from the air

$$I_{\text{out,g}} = \frac{\rho_{\text{rf,g}} q_{\text{in,g}} + \tau_{\text{tr,a}} q_{\text{in,a}}}{\pi}. \tag{2.69}$$

The flux leaving the free surface into the ambient air is given by

$$I_{\text{out,a}} = \frac{\rho_{\text{rf,a}} q_{\text{in,a}} + \tau_{\text{tr,g}} q_{\text{in,g}}}{\pi}. \tag{2.70}$$

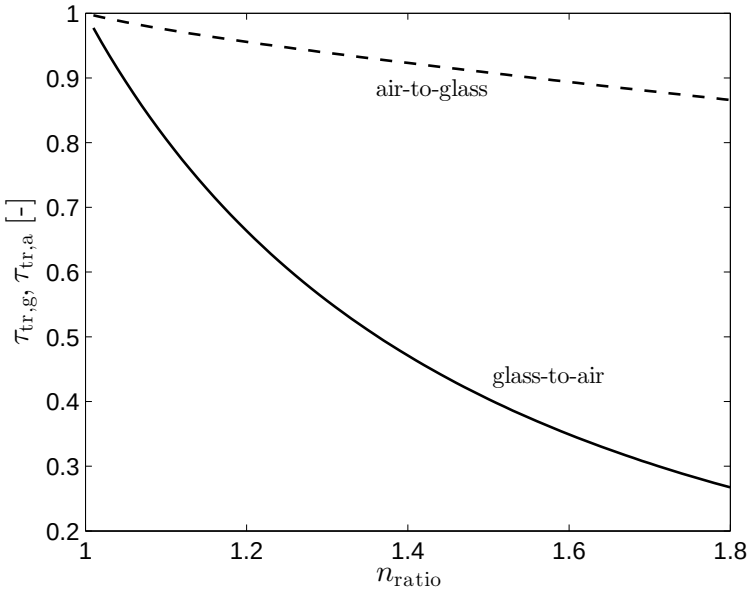

(a)

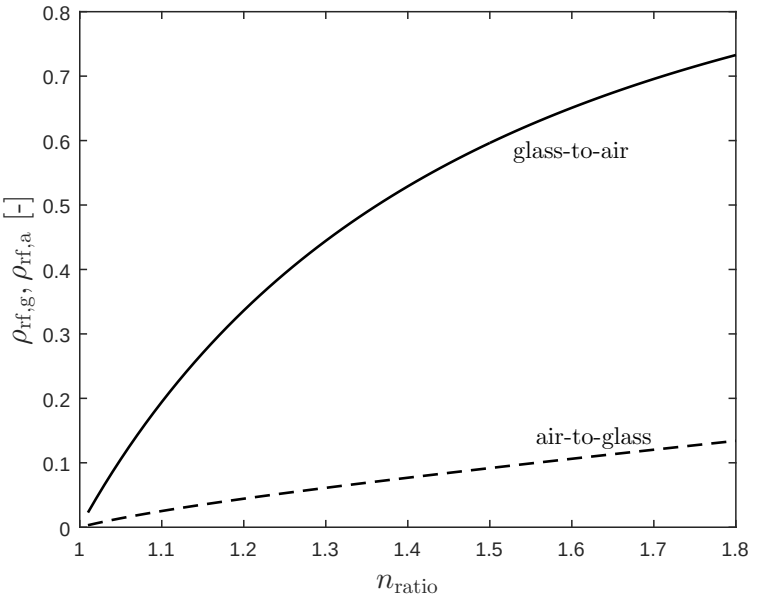

(b)

Figure 2.24: (a) Transmissivity as a function of n_{ratio} for the internal surface (glass-to-air) $\tau_{\mathrm{tr,g}}$ and the external surface (air-to-glass) $\tau_{\mathrm{tr,a}}$. (b) Reflectivity as a function of n_{ratio} for the internal surface (glass-to-air) $\rho_{\mathrm{rf,g}}$ and the external surface (air-to-glass) $\rho_{\mathrm{rf,a}}$.

In order to calculate the flux, the intensities are integrated over all relevant directions and wavelengths.

Boundary condition for the energy equation

Since the transfer of heat is modified at the free surface, the boundary condition for the energy equation presented in Section 2.2.3 must be adapted accordingly. Although the convective heat flux remains identical, the radiative flux is different when the glass is considered a semi-transparent medium. In the previous model from Section 2.2, the condition at the free surface was given by an opaque and grey radiative flux for all wavelengths

$$-k\frac{\partial T}{\partial n} = h\left(T_\mathrm{s} - T_\mathrm{ext,conv}\right) + \epsilon\sigma\left(T_\mathrm{s}^4 - T_\mathrm{ext,rad}^4\right). \tag{2.71}$$

Considering a non-grey glass with a semi-transparent window, the condition on the flux has to be modified to take into account only the opaque region of the spectrum (i.e. above $\lambda = 3.8$ μm). Note that the energy loss due to the semi-transparent part is already included when the RTE is solved by considering its adequate boundary condition. The new condition at the free surface of the fiber is written as

$$-k\frac{\partial T}{\partial n} = h\left(T_\mathrm{s} - T_\mathrm{ext,conv}\right) + \int_{\lambda_\mathrm{c}}^{\infty} \epsilon_{\mathrm{op},\lambda}\left[I_{\mathrm{b},\lambda}(T_\mathrm{s}) - I_{\mathrm{b},\lambda}(T_\mathrm{env})\right]\mathrm{d}\lambda, \tag{2.72}$$

where $\epsilon_{\mathrm{op},\lambda}$ and T_env are respectively the emissivity of the opaque part of the spectrum and the temperature of the environment if an isothermal enclosure is considered.

The opaque emissivity $\epsilon_{\mathrm{op},\lambda}$ in Eq. (2.72) is different from the value of the emissivity ϵ_s taken in Section 2.2 where the fiber is assumed opaque for all wavelengths. $\epsilon_{\mathrm{op},\lambda}$ is represented in Fig. 2.20 for the range from [4 - 12] μm. It rapidly increases to approximately reach a value of one, i.e., that of a black body. Above $\lambda = 8$ μm, the emissivity then begins to decrease, before increasing again around $\lambda = 10$. For simplicity, a constant opaque emissivity is assumed in this work. Its value is determined as a weighted average

$$\epsilon_\mathrm{op} = \int_{\lambda=4\mu\mathrm{m}}^{\lambda=12\mu\mathrm{m}} \frac{\epsilon_{\mathrm{op},\lambda} I_{\mathrm{b},\lambda}}{I_{\mathrm{b},\lambda}}\mathrm{d}\lambda, \tag{2.73}$$

where $I_{\mathrm{b},\lambda}$ is calculated at 1300°C. The integration provides a value of $\epsilon_\mathrm{op} = 0.91$. Note that, if the black body intensity is taken at $T = 600$°C, ϵ_op varies by about 0.1%, which demonstrates that the temperature used to compute the blackbody intensity has almost no influence. Assuming a constant opaque emissivity, Eq. (2.72) can be reformulated as

$$-k\frac{\partial T}{\partial n} = h\left(T_\mathrm{s} - T_\mathrm{ext,conv}\right) + \epsilon_\mathrm{op}\left[f_\mathrm{g} I_\mathrm{b}(T_\mathrm{s}) - f_\mathrm{env} I_\mathrm{b}(T_\mathrm{env})\right], \tag{2.74}$$

where the ratio f_g and f_{env} are ratios of a black body emission in the opaque spectrum to the total emission over the whole spectrum, given by

$$f_i = \frac{\int_{\lambda_c}^{\infty} I_{b,\lambda}(T_i)d\lambda}{\int_0^{\infty} I_{b,\lambda}(T_i)d\lambda}. \tag{2.75}$$

As in Section 2.2.3, the radiative environment surrounding the fiber is not uniform and

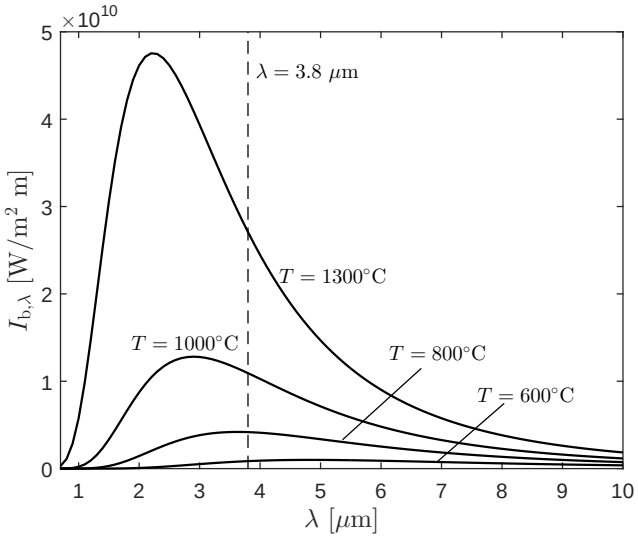

Figure 2.25: Black body emissive power as a function of the wavelength for a body at different temperatures. $\lambda_c = 3.8\mu$m is the cutting wavelength.

its modeling requires a complex treatment. Nonetheless, for the same reasons as discussed in the case of a grey opaque fiber, the environment is taken here as a black body leading to $f_{env} = 1$ and $I_b(T_{env}) = \sigma T_{env}^4$. On the other hand, the fraction f_g has to be considered and its value is a function of the temperature. The variation is large over the range of temperature, from 0.4 to 0.8. The value is set to 0.47 which is the average between 1300°C and 1000°C considered as the range of temperatures where radiation has a non-negligible contribution. It is easy to show through the black body emission, represented in Fig. 2.25, that the temperature has a strong effect on radiation. The figure shows the large decrease of emission with temperature. As a result, the term $\kappa_\lambda I_{b,\lambda}$ in Eq. (2.60) decreases leading to a lower radiative flux.

2.6.5 Band model approach

Since it is impossible to solve the RTE for a continuous spectrum, which would require an infinite number of equations, the spectrum is generally divided into different bands of approximately constant absorption coefficient. The absorption coefficient of the corre-

sponding band is then calculated as

$$\kappa_{\text{band},i} = \frac{1}{\lambda_{i+1} - \lambda_i} \int_{\lambda_i}^{\lambda_{i+1}} \kappa_\lambda \mathrm{d}\lambda. \tag{2.76}$$

This simple average of κ_λ over the range of wavelengths is the common band calculation used for glass [48, 50, 54, 55]. The number of bands chosen depends on the level of accuracy. Unfortunately, each additional band leads to an additional equation to solve, which increases the complexity of the problem. Generally, the choice of bands is made such as to specifically represent the Fe^{2+} and the OH absorption bands leading to a total of four bands. The following range has been arbitrarily chosen to take into account these two peaks[1]:

$$\kappa_\lambda = \begin{cases} 0 & \text{if } \lambda \leq 0.7\ \mu\text{m}, \\ 100.42 & \text{if } 0.7 \leq \lambda < 1.5\ \mu\text{m}, \\ 80.96 & \text{if } 1.5 \leq \lambda < 2.6\ \mu\text{m}, \\ 457.83 & \text{if } 2.6 \leq \lambda < 3.2\ \mu\text{m}, \\ 322.04 & \text{if } 3.2 \leq \lambda < 3.8\ \mu\text{m}. \end{cases} \tag{2.77}$$

These bands are represented in Fig. 2.26. At wavelengths below 0.7 μm, it is assumed that the glass is transparent. On the other hand, at wavelengths above 3.8 μm, the glass is opaque: κ_λ is not considered and the radiation is taken into account as a surface flux associated to a surface emissivity.

2.6.6 Summary of the radiative properties

The different material properties and parameters used in the semi-transparent treatment of radiation are summarized in Table 2.3.

2.7 Summary

This chapter has been entirely dedicated to the description of the physics of the fiber drawing process and to the development of the corresponding mathematical models. After a brief review of the specificities of the glass material, the two-dimensional axisymmetric model and its simplified one-dimensional version have been developed in details. This has been followed by a summary of all material properties required by these models and their experimental measurement. Finally, the models describing the ambient air flow and internal radiation have been introduced as extensions to the main axisymmetric model.

[1] A more detailed study would be required for optimizing the band limits.

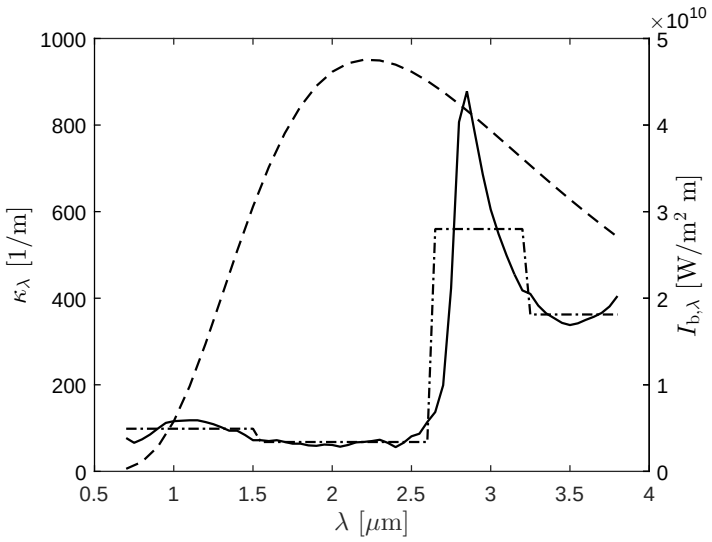

Figure 2.26: Absorption coefficient κ_λ (solid line) and emissive power of a blackbody $I_{\mathrm{b},lambda}$ (dash line) as a function of the wavelength at temperature $T = 1300°\mathrm{C}$. The dash-dotted line represents to approximation of the four bands used to represent the absorption coefficient in the band model.

As a single fiber is considered, the main, two-dimensional model is considered axisymmetric. The region of interest includes the tip (∼1300°C) and the liquid region until the transition point (∼750°C). The molten glass is assumed to be a Newtonian liquid and the effects of inertia, surface tension, drag, viscosity and gravity are included. The drag force and convective heat transfer due to the entrained air flow at the fiber surface are modeled through empirical correlations. Convective heat cooling is based on a constant air temperature, but an axially varying temperature is also considered. In its standard form, this model represents the fiber as an opaque medium whose surface is approximated as grey and diffuse with an effective emissivity to account for the semi-transparent nature of the glass. The environment is considered as a black body at constant temperature. Except for the density and the specific heat, all other material properties of the glass are considered temperature-dependent. In particular, the strong variation of the glass viscosity with temperature is modeled by the VFT law. Unless otherwise specified, the glass composition considered corresponds to that of the Advantex© glass, whose material properties have been measured experimentally. Given a flow rate and a drawing velocity, the model provides the position of the free surface, the velocity and temperature fields inside the fiber, and all other derived quantities.

A simplified one-dimensional model has then been derived by assuming that the main variations take place along the fiber. It accounts only for the viscous effects, and neglects those of inertia, surface tension, air drag and gravity. This semi-analytical model is

Refractive index glass n_{g} [-]	1.56
Refractive index air n_{a} [-]	1
Absorption coefficient [0.7,1.5] μm, $\kappa_{\mathrm{band},1}$ [1/m]	100.42
Absorption coefficient [1.5,2.6] μm, $\kappa_{\mathrm{band},2}$ [1/m]	80.96
Absorption coefficient [2.6,3.2] μm, $\kappa_{\mathrm{band},3}$ [1/m]	457.83
Absorption coefficient [3.2,3.8] μm, $\kappa_{\mathrm{band},4}$ [1/m]	322.04
Absorption coefficient (grey) κ [1/m]	207
Emissivity platinium ϵ_{pt} [-]	0.18
Emissivity opaque ϵ_{op} [-]	0.91
Black body ratio f_{g} [-]	0.47
Reflection coefficient air $\rho_{\mathrm{rf,a}}$ [-]	0.1005
Reflection coefficient glass $\rho_{\mathrm{rf,g}}$ [-]	0.6304
Transmission coefficient air-to-glass $\tau_{\mathrm{tr,a}}$ [-]	0.8995
Transmission coefficient glass-to-air $\tau_{\mathrm{tr,g}}$ [-]	0.3696

Table 2.3: Summary of the radiative properties and parameters used in the semi-transparent model for the Advantex© composition.

thus numerically much more tractable and provides a more intuitive interpretation of the relation between key process parameters.

Finally, the main two-dimensional axisymmetric model has also been extended to account for the flow of the entrained ambient air and the semi-transparent nature of glass. The air flow is obtained by solving the RANS equations coupled to the main fiber model so as to provide a more accurate estimation of the convective heat transfer at the fiber surface. On the other hand, the internal radiation model assumes that the glass is transparent for wavelengths below 0.7μm, semi-transparent between 0.7μm and 3.8μm, and opaque above. The semi-transparent window is solved using either a one- or four-band model. The fiber surface is assumed diffuse for reflection and transmission.

The numerical resolution of these models is detailed in Chapter 4. They are subsequently used to analyze the drawing process, to assess through sensitivity analysis the quantitative contribution of different modeling fidelity levels and key parameters, to characterize the process operating window, and to predict the break rate.

Although very detailed, these models are still based on several simplifications. First, they focus solely on the liquid region of a single fiber and neglect any azymuthal variation. Then, the surrounding environment is considered uniform and constant for both radiation and convection. In particular, the interaction with the bushing and other potential setup elements (e.g., finshields) is neglected. Additionally, the viscoelastic behavior expected when approaching transition is completely neglected. Finally, the wetting effect of the glass melt at the tip is not considered. These simplifications should be kept in mind when analyzing the simulation results.

Chapter 3

Experimental approach

Although the main focus of this work is on the physical and numerical modeling of the drawing of a single fiber, experimental measurements are also carried out. The objective is three-fold: *i)* to determine the value of several input parameters for the model, *ii)* to provide validation data, and *iii)* to support the investigation of the break in Chapter 7.

A dedicated fiberization unit with a single tip has been designed and built for this study. The motivation for drawing only one fiber is to eliminate interactions with other fibers and to provide easier access for measurements. Several data can be recorded, such as the flow rate, the tip temperature or the surrounding air temperature. One of the key feature of the setup is the possibility to measure the radius of the fiber meniscus. Nevertheless, the small scales involved in the process leads to measurement limitations, as discussed below.

This chapter focuses on the description of the overall apparatus and measurement equipments. The different measurements are presented, but their comparison with numerical results is postponed to the next chapters. The first section provides an overview of the device and test facility. Each type of data measurement is then described separately and in details in the subsequent sections.

3.1 Overall apparatus

A schematic of the facility is shown in Fig. 3.1. Glass cullets are melted at a temperature of up to 1450°C inside an electrically heated platinium-rhodium container. The temperature inside the furnace is monitored through three type-R thermocouples located at different heights. A regulation system is associated to the middle thermocouple in order to maintain a constant temperature of the melt in the container. The maximum height of the liquid glass in the furnace is about 8 cm. Before each experiment, the same amount of glass is put into the melter, which has previously been emptied, to ensure the same level of the

melt at the beginning of each experiment, as this level determines the flow rate at the tip exit. A single cylindrical tip is used with a diameter of 1.2 mm and a length of 4.2 mm. The forming fiber is drawn by a winder, with a drawing velocity range of $0-3000$ m/min.

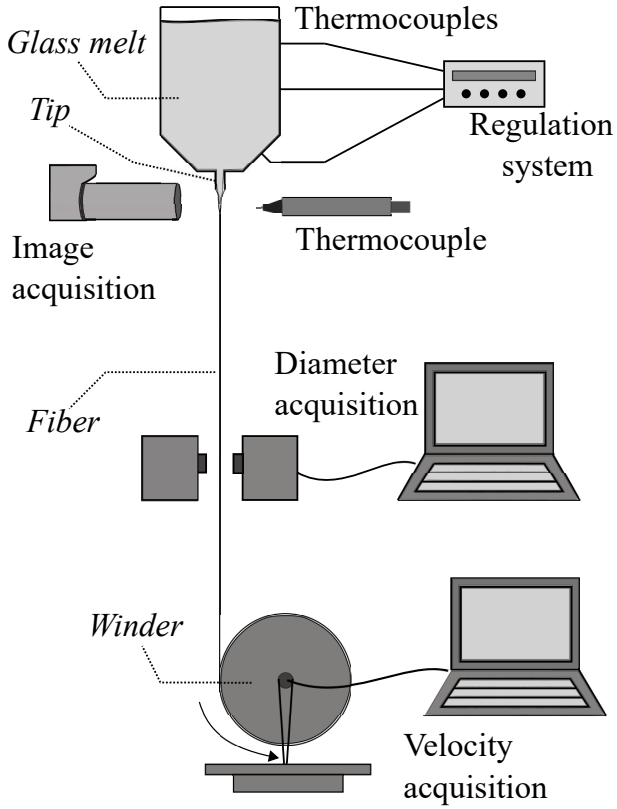

Figure 3.1: Schematic of the experimental unit.

Operating window

The operating window and the related process parameters are close to those used in the industrial production, except for the glass height, which is here lower. This results in a lower flow rate although the tip diameter is of the same order of magnitude as in a production bushing. Consequently, the winder speed is also lower in order to achieve the same range of final diameter. The device has two control parameters, the regulation temperature and the winder velocity, with which the tip temperature and the final diameter of the fiber can easily be controlled.

The temperature at the tip determines the flow rate through the viscosity, as given by Eq. (2.10), rewritten here:

$$Q_0 = \frac{\pi}{8\eta_0}\frac{\rho g H}{l} r_0^4,$$

where η_0 is the viscosity of the glass at the tip of the experimental unit. The evaluation

of the conservation of mass at the winder leads to the following relation:

$$Q_0 = \text{constant} = \pi r_\text{f}^2 v_\text{f}, \tag{3.1}$$

where r_f and v_f are the final radius of the fiber and the drawing velocity at the winder, respectively. The final radius is then obtained by

$$r_\text{f} = \sqrt{\frac{Q_0}{\pi v_\text{f}}}. \tag{3.2}$$

The choice of these two control parameters, T_0 and v_f, automatically fixes r_f (or the diameter $2r_\text{f}$, which is usually the quantity reported).

The operating window of the device is shown in Fig. 3.2. The figure intentionally focuses on lower values of the diameter $2r_\text{f}$, which are observed to be more critical in the production line. The curves are non-linear due to the temperature-viscosity dependence. In particular, the increase of the tip temperature leads to a higher flow rate and, therefore, a higher winder velocity to keep a constant final fiber diameter. The range of speeds of the winder is large so that smaller diameters (3-6 μm) can also be produced, as those are important for the study of the fiber breaking.

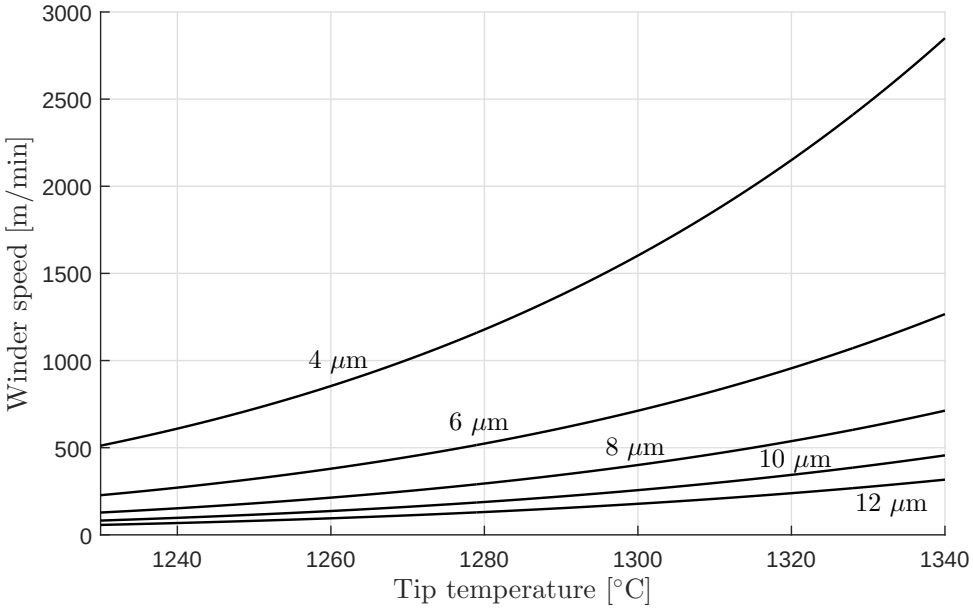

Figure 3.2: Operating window: winder velocity as a function of the tip temperature for different values of the final fiber diameter.

Measurement capabilities

The experimental approach is mainly used as a support to the physical modeling described in Chapter 2. In particular, different types of measurements have been implemented to provide boundary conditions for the model. In addition, the radius of the free surface and the final fiber diameter can also be measured for model validation. The physical quantities directly measured are:

- final fiber radius r_f,
- flow rate Q_0,
- fiber radius $r_\mathrm{s}(z)$,
- tip temperature T_0,
- air temperature $T_{\mathrm{ext,conv}}$.

Note that the winder speed is not considered as a measurement because it is a control parameter, like the regulation temperature. Moreover, for a given winder velocity v_f, the flow rate Q_0, final radius r_f and tip temperature T_0 are dependent on each other, as shown through Eqs. (2.10) and (3.1). This relationship is used below to assess the quality of the measurements and the validity of Eq. (2.10).

Additional measurements are currently technically not feasible due to the small scales of the fiber and the high temperature of the melt. Moreover, the accuracy of most experimental devices is not sufficient to capture the large spatial variations close to the tip. Similarly, glass temperature measurements are not performed either. Such measurements are typically based on the radiative emission of the glass measured by a pyrometer. This thermal radiation depends on the wavelength, the spatial scale of the fiber and its temperature. All these effects inevitably lead to large measurement errors, rendering any measurement meaningless. Finally, it should also be mentioned that the velocity field of the ambient air is not investigated experimentally, as it is typically turbulent and involves large temperature gradients.

3.2 Flow rate

The glass flow rate Q_0 flowing out of the tip is an input of the model. It is controlled by the glass height H, the tip radius r_0, and the glass temperature at the tip T_0 (see Eq. (2.10)). The flow rate can be either directly measured, or calculated from the measurement of other quantities, as described below.

3.2.1 Direct measurement

The measurement of Q_0 consists in weighting the fibers produced during a period of time Δt. The average flow rate over this time period can be deduced from their mass M through

$$Q_0(\Delta t) = \frac{M}{\rho \Delta t}. \tag{3.3}$$

This assumes that the flow rate is constant in time. However, the glass height in the furnace decreases over time, which reduces the static pressure and, thus, the flow rate. The importance of this decrease is investigated further below.

3.2.2 Indirect measurement

The flow rate can also be deduced from the final radius measurements trough Eq. (3.1), that is

$$Q_0 = \pi r_\mathrm{f}^2 v_\mathrm{f},$$

where the winder velocity, as a control parameter, is known. Similarly, Q_0 can be calculated from the measurement of the tip temperature T_0 using Eq. (2.10),

$$Q_0 = \frac{\pi}{8\eta_0(T_0)} \frac{\rho g H}{l} r_0^4,$$

where l and r_0 are fixed by the bushing design and H is assumed to be approximately constant, as discussed in the next section.

3.2.3 Pressure loss

During an experiment, the decrease of the glass height H over time causes a pressure loss at the tip, and correspondingly a decrease in the flow rate. The relation between the flow rate and the glass height can be expressed, from Eq. (2.10), as

$$Q_0(t) = \alpha H(t)\,, \tag{3.4}$$

where t is the time, and the proportionality factor $\alpha = \pi \rho g r_0^4 / 8\eta_0 l$ remains constant. On the other hand, the variation of the glass height can be estimated by conservation of mass:

$$H(0) - H(t) = \frac{1}{S} \int_0^t Q_0(t')\mathrm{d}t'\,, \tag{3.5}$$

where S is the constant cross-section area of the furnace through which the glass flows. Taking the derivative of this relation with respect to time leads to

$$\frac{\mathrm{d}H(t)}{\mathrm{d}t} = -\frac{1}{S}Q_0(t)\,. \tag{3.6}$$

By combining this expression with the time derivative of Eq. (3.4), one obtains the time dependence of the volumetric flow rate:

$$Q_0(t) = Q_0(0)\exp\left(-\frac{\alpha t}{S}\right), \tag{3.7}$$

and, consequently, the total mass of fiber produced:

$$M(t) = \rho\int_0^t Q_0(0)\exp\left(-\frac{\alpha t'}{S}\right)\mathrm{d}t'\,. \tag{3.8}$$

Experimental validation

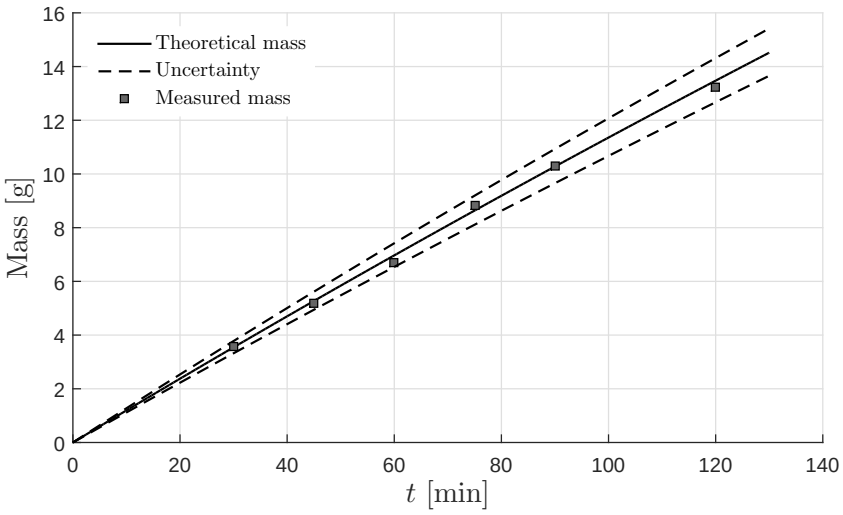

Figure 3.3: Comparison between the measured mass of fiber produced on the experimental device for several experiments of increasing duration and the prediction of Eq. (3.8) as a function of time. The dashed curves represent the uncertainty of the prediction due to the uncertainty on the tip temperature, which is about ±10°C.

In order to assess the validity of relation Eq. (3.8), the mass of fiber produced has been measured experimentally for different durations of the experiment and compared to the prediction of this equation, as shown in Fig. 3.3. The major source of uncertainty in evaluating Eq. (3.8) stems from the uncertainty on the tip temperature, which has an accuracy of ± 10°C, and leads consequently to an uncertainty on the factor α through the

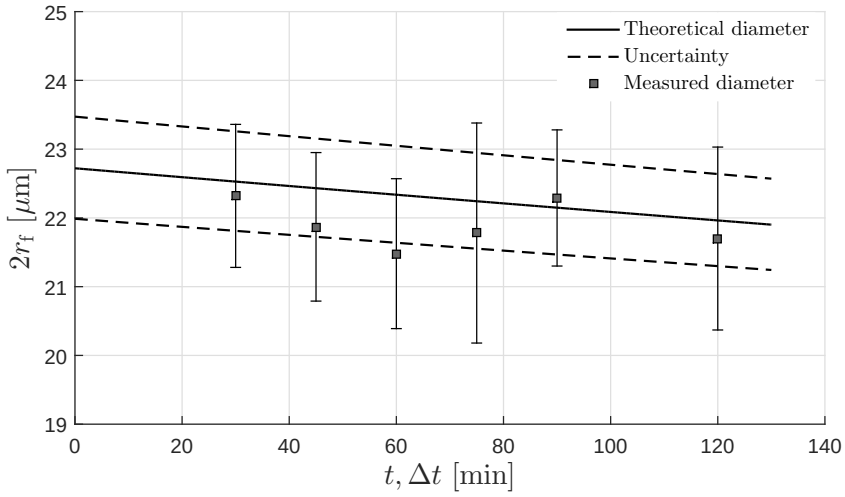

Figure 3.4: Comparison between the measured final fiber diameter for several experiments of increasing duration Δt and the diameter calculated from the prediction of Eq. (3.8) as a function of time t. Note that the measured values (symbols) correspond to an average over the experiment duration Δt and not at the instantaneous time t. The dashed curves represent the uncertainty of the prediction due to the uncertainty on the tip temperature, which is about ± 10°C.

temperature dependence of the viscosity. This uncertainty is represented by the dashed lines. As the figure shows, the measured mass follows very well the theoretical curve. Some discrepancies can be observed, which are due to the limited accuracy of the glass height measurement at the beginning of the experiment.

Figure 3.4 shows the final fiber diameter measured for several experiments of increasing duration using scanning electron microscopy (SEM) as the average and the standard deviation (error bar) of 30 samples randomly taken from the fibers drawn over the time of the experiment. Note that this measured value does not represent the fiber diameter at the end of the experiment, but rather an average over the duration of the experiment. For comparison, the diameter $2r_\mathrm{f}(t) = 2\sqrt{Q(t)/\pi v_\mathrm{f}}$ calculated by mass conservation from the prediction of Eq. (3.8) is also shown including the uncertainty on the tip temperature. Both measurements and predictions agree again very well. Moreover, it can be observed that the mass flow rate, and thus the final fiber diameter vary only slowly in time. More specifically, the final diameter decreases by less than 1 μm over a period of 2 hours, which is much less than the standard deviation.

This excellent agreement provides support to Eq. (3.8), and, consequently, to the estimation of the volumetric flow rate, Eq. (2.10). Additionally, it shows that for short duration experiments ($<$ 40 min) the decrease in flow rate over time has a negligible impact on the measured quantities.

3.3 Tip temperature

The tip temperature is involved in the physical model as a thermal boundary condition. This temperature depends on the temperature regulation, but differs from the value measured by the regulation thermocouple due to heat transfer in the glass container. Therefore, T_0 must be directly measured with a non-intrusive device. On the other hand, it can also be indirectly determined from the flow rate.

3.3.1 Direct measurement

The tip temperature T_0 is measured using a two-color pyrometer pointing towards the tip. In order to validate the measurement, three different regulation temperatures are chosen: $T = 1260°C$, $T = 1290°C$ and $T = 1320°C$. For each of those temperatures, the data from the thermocouple situated at the lower position (see Fig. 3.1), called *TC Down*, is recorded in addition to the data from the pyrometer. The error bar is related to the repeatability of the measurement over 4 experiments (which is higher than the variability observed with both devices during one experiment). Note that the absolute error on the measurement is not known. Moreover, in both cases, the temperature of the Pt-Rh container and not the glass melt is measured.

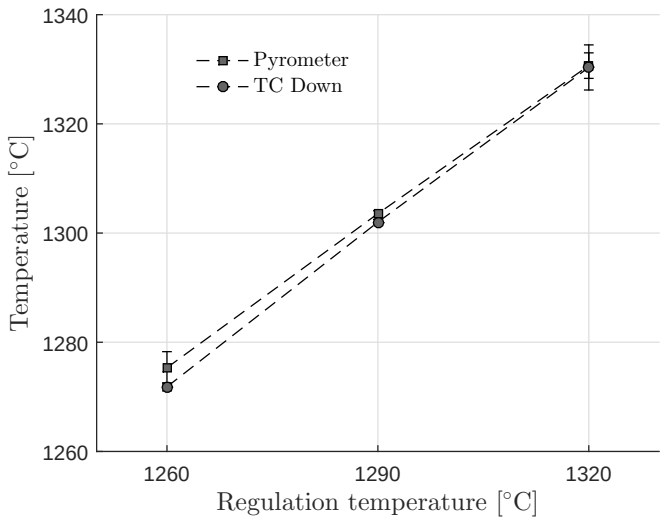

Figure 3.5: Temperature measured from the pyrometer and from the thermoucouple situated at the lower position in the bushing. The x-axis represents the temperature imposed for the regulation (i.e. measured by the thermocouple at the middle position).

These two measurements are then compared. Even if the lowest thermocouple is not located in the direct vicinity of the tip, it is the region closest to the tip where the temperature is recorded. The results are shown in Fig. 3.5 for each regulation temperature.

Excellent agreement is found at $T = 1320°C$ and $T = 1290°C$ between the two measurements, while a small variation is observed at $T = 1260°C$. It is thus assumed that the lowest thermocouple provides a good estimate of the tip temperature, although the melt temperature is probably slightly higher.

3.3.2 Indirect measurement

The temperature at the tip can also be calculated from the measured flow rate. More specifically, if Q_0 is known, the viscosity η_0 and thus the temperature T_0 can be computed from Eqs. (3.4) and (2.9), respectively. However, the direct measurement of Q_0 described in Section 3.2 provides an average value over the experiment duration. Another option is to use an indirect measurement of Q_0 based on the winder speed and the final radius. As it is shown in the next section, this radius is recorded on-line as a function of time.

3.4 Final radius

The final fiber radius is typically an output of the model. Unlike the flow rate or the tip temperature, it is thus not a required input parameter. Moreover, it does not represent a very useful quantity for validation as it depends directly through mass conservation on the flow rate and the winder velocity. Nonetheless, the measurement of r_f is rather easy and accurate, and provides data that can be used to deduce other important quantities, as already illustrated above. Therefore, the final radius is investigated experimentally using three different techniques, as described below.

3.4.1 Direct measurement

The final diameter of the fiber can be measured using three different devices:

Laser diffractometer Located 40 cm below the tip exit, the measurement of the diameter with this equipment, called Keyence, is based on the deviation of a laser beam and the measurement of the projected shadow due to the presence of the fiber. Although this equipment allows an on-line measurement, the horizontal vibration of the fiber represents a major limitation. Figure 3.6(a) illustrates a measurement over a period of 900 seconds. The sampling rate is equal to 1 Hz so that higher frequencies are not captured. Its accuracy is estimated to 0.5 μm. Unfortunately, the device is not calibrated for diameters below 8 μm.

Particle size analyzer Called Occhio, the measurement is based on imaging a sample of typically thousand of fiber pieces that have been previously cut. Although the

method is off-line, it has the advantage of providing a statistical distribution. Moreover, it does not have the resolution limitation of the laser diffractomer so that smaller diameters can be measured. An example of distribution obtained with this equipment is shown in Fig. 3.6(b). The measurement error is estimated to be about 0.3 μm.

Scanning Electron Microscope (SEM) It consists in measuring off-line the radius of a few fiber samples from a scanning electron microscope image. Although this technique has the highest measurement resolution, it requires the operator to manually identify on the screen the contour of each sample. This introduces a repeatability error of about 0.1 μm. Generally, around 30 samples per experiment can be measured compared to 5000 samples for the Occhio. This method is thus less representative of the average diameter. An example of the results is presented in Fig. 3.6(c).

3.4.2 Indirect measurement

In addition to these devices, the final radius can be indirectly obtained from the flow rate Q_0 and the winder speed, or the total mass of fiber produced. It is important to recall that the measurement of the flow rate, or the mass, represents an average value over the duration of the experiment. Thereby, the indirect measurement of the final diameter is also an average value. In other words, this approach does not yield a distribution. These different methods are now compared and discussed.

3.4.3 Comparison of the methods

The measured diameter obtained with these four methods (including the indirect one) are summarized in Tab. 3.1 and in Fig. 3.6. The test case chosen corresponds to a regulation temperature set to 1320°C and a winder speed of 120 m/min, and the experiment has a duration of 900 s. Several samples of the fiber produced are also analyzed with the particle size analyzer and the SEM. As shown, the particle size analyzer leads to the largest mean diameter of 19.9 μm, while the laser diffractometer provides a mean diameter of 18.2 μm. Both measurements have a standard deviation of 0.9 μm, which is lower than the difference between their respective averages. This discrepancy can come from the calibration of the particle size analyzer, because of its slightly larger average than the other measurements. On the other hand, the stabilization of the fiber in the laser window of the laser diffractometer is poor due to the horizontal vibrations of the fiber. Unfortunately, the magnitude of this error cannot be readily quantified.

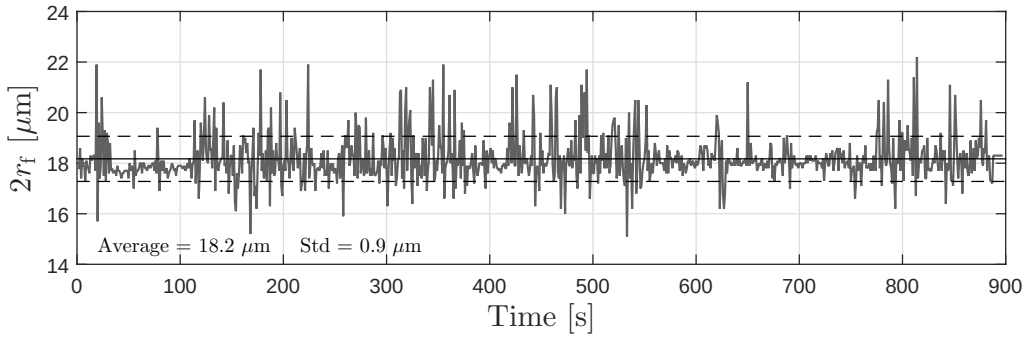

(a)

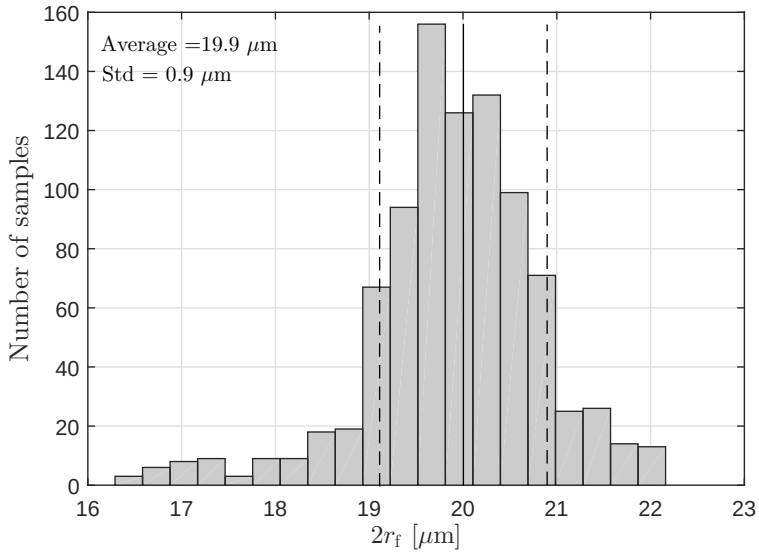

(b)

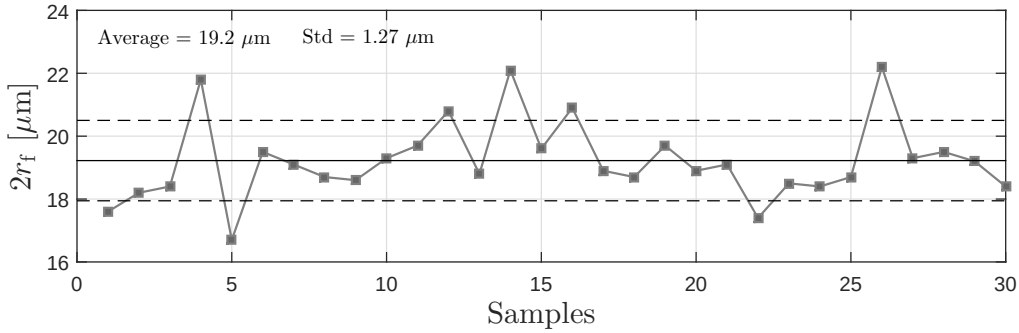

(c)

Figure 3.6: Measurement of the final diameter of the fiber $2r_\mathrm{s}$ with (a) laser diffractometer (b) particle size analyzer and (c) scanning electron microscope. The test case was performed with a temperature regulation set to 1320°C and a winder velocity of 120 m/min. The solid and the dashed lines correspond to the average and the standard deviation, respectively.

The scanning electron microscope measurements lead to a larger standard deviation compared to the two methods, which is simply due to the lower number of samples. Note that the average diameters obtained with both the laser diffractometer and the particle size analyzer fall in the standard deviation of the SEM measurements. Finally, an averaged diameter of 18.7 μm is indirectly obtained from the mass of fiber produced over the 900 s of the experiment. This value lies between those provided by the particle size analyzer and laser diffractometer devices.

Method	Average [μm]	Standard deviation [μm]
Particle size analyzer	19.9	0.9
Laser diffractometer	18.2	0.9
SEM	19.2	1.27
Weight	18.7	-

Table 3.1: Summary of the measurements of the final diameter $2r_\mathrm{s}$ using different techniques over a duration of 900 s.

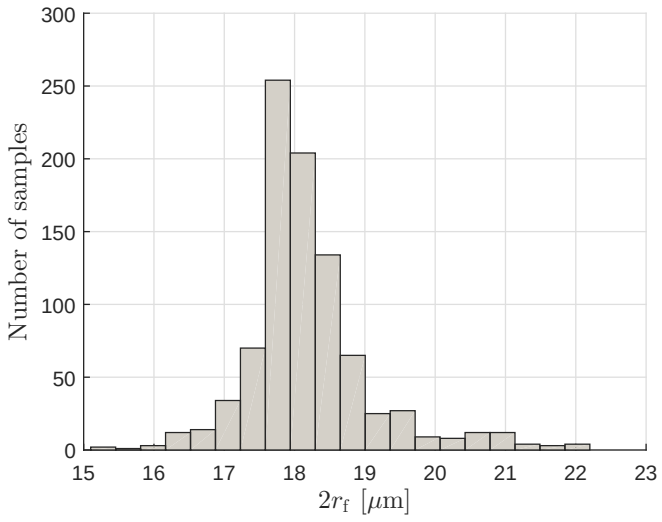

Figure 3.7: Distribution of the final diameter $2r_\mathrm{f}$ recorded by the Keyence during 900 s for the test case.

The measurements with the laser diffractometer and the particle size analyzer are both based on a sufficient number of samples to provide a relevant distribution, which is not the case of the scanning electron microscope. Figure 3.7 shows the distribution of the laser diffractometer data, which can be compared to the Occhio distribution from Fig. 3.6(b).

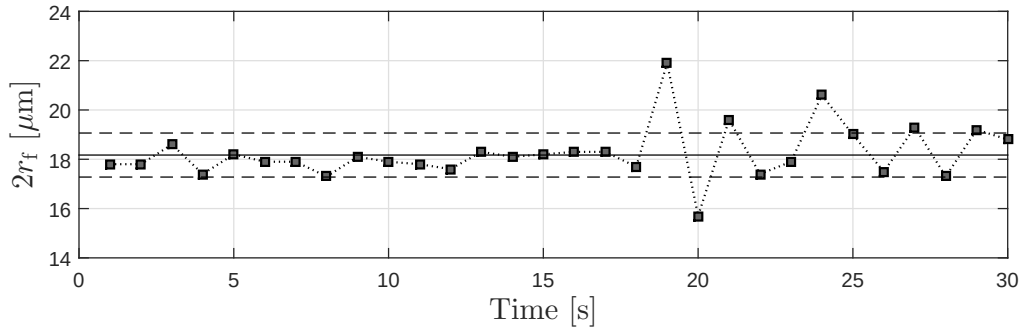

Figure 3.8: Final diameter $2r_f$ as a function of time recorded by the laser diffractometer. Only the first 30 s are shown here.

The range of variation is the same as mentioned previously, but the distribution from the Keyence is slightly narrower.

3.4.4 Discussion

The different measurements show clearly that the fiber diameter varies in time during the drawing process. All measurement techniques lead to a minimum diameter of ≈ 16 μm, while the maximum value is found to be around 22 μm. A zoom on the first 30 s of the Keyence measurement is shown in Fig. 3.8, where the data clearly suggest that the frequency of the radius fluctuations is lower than 1 Hz. For instance, the diameter varies between $t = 19$ s and $t = 20$ s by more than 6 μm over 1 s. Onofri *et al.* [17], based on the work of Lenoble [16], studied the fiber final diameter fluctuation using a laser diffractometer that they had developed for many years. They were thus able to reach a resolution of 0.02 μm (compared to 0.5 μm here[1]) and to remove the displacement effect of the fiber in the laser window. They considered E-glass and several tip temperatures between 1140°C and 1243°C. In order to keep the final diameter around 15-16 μm, the drawing velocity was increased for increasing tip temperatures. Their results show that the fluctuations of the diameter occur at frequencies between 0.69 Hz for lower T_0 and 0.96 Hz for higher T_0. They also observed a variation of about 0.3 to 0.5 μm over a duration of 3 minutes, which is lower than the 1 μm observed here. This indicates that the present process is more sensitive to fluctuations. Nevertheless, the origin of the fluctuation of the fiber radius was not found.

As the winder speed remains constant during the experiment, Eq. (3.1) indicates that this variability most likely originates in variations of the tip flow rate Q_0, which itself can be due to variations of the glass height $H(t)$ or of the tip temperature T_0 through the

[1]Note that the laser diffractomer used here is a commercial device.

viscosity η_0. As discussed in Section 3.2, the glass height continuously decreases over time and induces a slow decrease of the mean diameter. Therefore, it cannot explain the rapid fluctuations of the diameter observed here. Moreover, the duration of the experiment is too short to explain a variation of 1 μm.

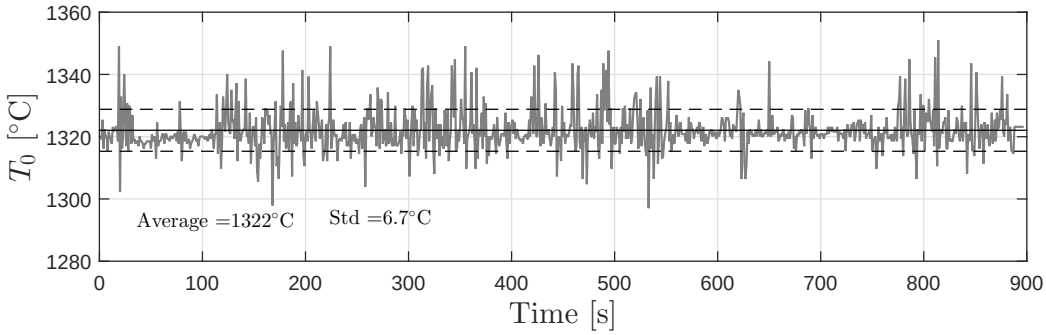

Figure 3.9: Temperature of the tip T_0 calculated from the conservation of mass based on the winder speed and the final diameter from the Keyence measurements shown in Fig. 3.6(a). The solid and the dashed lines represent the mean and the standard deviation respectively.

Consequently, the most likely explanation for these rapid diameter variations would be fluctuations in the tip temperature. Figure 3.9 shows the hypothetical time evolution of the tip temperature that would lead to the time behavior of the fiber diameter measured by the laser diffractometer (Fig. 3.6(b)), as calculated by mass conservation. The average temperature is 1322°C, while the standard deviation is 6.7°C. This result suggests that the fluctuation of 6 μm observed in the diameter could be caused by a maximal variation of about 50°C that takes place over less than 1 s. It is however difficult to verify this hypothesis. Furthermore, the tip exhibits an axial temperature gradient that can lead to variation of the flow rate calculation. Finally, the pyrometer provides a measurement of the bushing plate temperature rather than of the glass within the tip, and it cannot report fluctuations. Note that the temperature provided by the pyrometer is 1327°C, and falls within one standard deviation of the reverse temperature calculation.

Based on these considerations, it is suggested that the rapid time variations of the fiber diameter observed by the laser diffractometer are partly due to error measurements caused by horizontal vibrations of the fiber. The large variations (up to 6 μm) also observed by the other measurement techniques could be slower variations induced by time fluctuations of the tip temperature and, possibly, the slow decrease of the flow rate. Nonetheless, additional unknown factors could also play a role.

In conclusion, each measurement technique suffers limitations. In view of these results, the accuracy of the final fiber diameter is about 1 μm, which is non-negligible.

3.5 Surrounding temperature

A part of the air entrained by the fiber is first heated by the bushing plate, which is typically at a temperature of 1260 - 1320°C. In order to analyze the non-homogeneity of the ambient air temperature, it has been measured at a distance of 4 cm from the fiber for several axial locations using a thermocouple. The thermocouple measurement error is estimated to be about 1°C. However, an additional error due to the radiative emission of the bushing plate must be taken into account. The thermocouple directly absorbs this radiation and is consequently heated. The temperature recorded is thus not solely associated to the surrounding air. This effect has been demonstrated here by covering the thermocouple with a sheet of commercial aluminum. This material has a very low emissivity and thus reflects the major part of the irradiation. The temperature measurements with and without the aluminum protection are shown in Fig. 3.10. As expected, the aluminum strongly impacts the temperature measured by the thermocouple, as also reported by McKoene [13]. Furthermore, the discrepancy is larger near the bushing where the thermocouple is more exposed to radiation. Nevertheless, in both cases the axial distribution of the surrounding air temperature that is used for convection heat transfer calculations can be expressed in terms of an exponential function (Eq. (2.24)), rewritten here

$$T_{\mathrm{ext,conv}}(z) = T_{\mathrm{r}} + (T_{\mathrm{b}} - T_{\mathrm{r}}) \exp(-az).$$

The parameters are $T_{\mathrm{b}} = 106.6$, $T_{\mathrm{r}} = 31.61$ and $a = 0.449$ for the case with the aluminum protection, which is assumed to be the more representative of reality.

3.6 Free surface

The evolution of the radius as a function of the axial coordinate can be optically measured in the vicinity of the tip. Because it is the only variable of the physical model that can be experimentally measured as a function of the axial coordinate z, it is used for validation, as discussed in Chapter 5.

The measurement consists in acquiring a digital image of the forming fiber in the visible range of wavelengths. A camera with macro-lenses provides sufficient resolution to accurately capture the meniscus region, as illustrated in Fig. 3.11. Note that the major limitation is due to optical effects at the edges of the fiber, and not to the resolution. A post-processing method has been developed to extract the position of the fiber edges from the image and thus determine the fiber radius. This method is based on the canny edge detection algorithm [59].

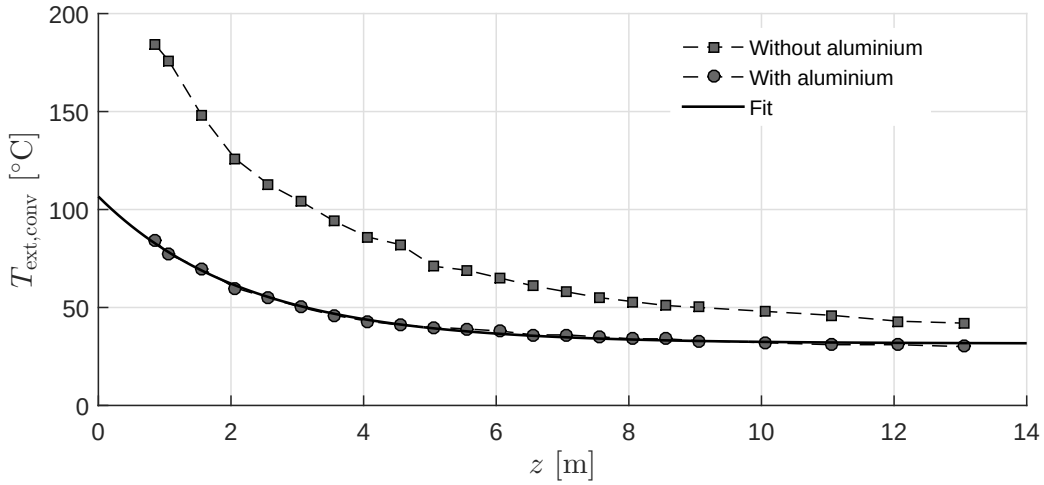

Figure 3.10: Measurements of the surrounding air temperature at a distance of 4 cm from the fiber as a function of the vertical coordinate. One data set has been obtained by covering the thermocouple with an aluminum sheet to minimize the effect of radiation. An exponential fit of the experimental data for the case with aluminum protection is also represented.

The different steps of the post-processing are the following:

1. calibrate the image by imposing an angle of rotation in order to align it with the horizontal;

2. transform the picture from RGB components into grey level;

3. calculate the contour of the free surface using the canny method;

4. identify the pixels associated to the contour;

5. transform these pixels into coordinates;

6. filter the residual noise.

The calibration is required to subsequently determine the spatial coordinates from the pixels. On the other hand, the use of a binary image (i.e. grey level) is a requirement for the canny method.

The third step consists in applying the canny edge detection algorithm. Because the edge detection can be performed using numerous methods depending on the problem and the required accuracy, several approaches have been tested (i.e., Prewitt, Sobel, Roberts and Canny). The Canny edge detection algorithm was found to yield the best results, as it is based on two detection thresholds, which leads to a better control of the method. The

grey scale intensity gradient is computed in the axial and radial directions. The location of the local maximum of the magnitude is extracted. The particularity of this method is the possibility to eliminate a certain range of maximum intensity. If the maximum is below the low threshold, it is rejected. If the value is between the two threshold values, the edge is declared as weak. Finally, if the maximum is above the high threshold, the maximum is denoted as strong. As a result, the algorithm ensures the continuity of the edge, i.e. the strong edges are maintained, while the weak edges are preserved only if they are connected with a strong edge. This technique consequently allows the choice of the level of detection. The method has been implemented in the image processing toolboox of the software Matlab®.

At the end of this step, each pixel has a value of 1 if an edge is found or 0 otherwise. However, due to radiation, the border is usually spread over a few pixels and an additional treatment must be performed to obtain a smoother contour. A specific routine has been developed based on the calculation of the continuity of the border line. It consists in calculating the distance of a pixel to its nearest neighbors. If this distance is larger than a certain threshold value, the pixel is discarded. Finally, the spatial coordinates can then be calculated based on the position of the edge pixels. In addition, a final filtering is applied to remove the residual noise if necessary.

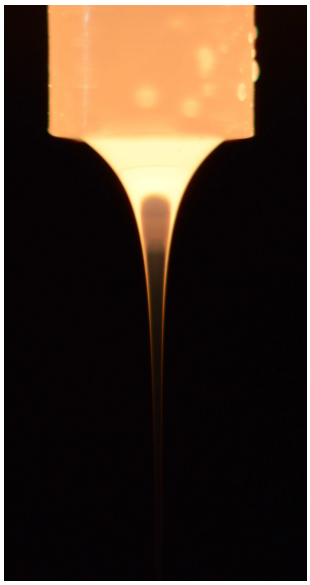

Figure 3.11: Picture of the cone meniscus including the tip obtained with a camera with macro-lenses. The regulation temperature was set to 1350°C to achieve a final diameter of 35 μm.

The variability of the fiber emissive radiation along the axial direction and the radiative edge effects limit the accuracy of the method. Since the radiation is high near the tip,

the exposure time of the camera must be short in order to avoid any saturation of the CCD captors. However, the fiber does not emit as much in the lower region, since the temperature is lower. As a result, the camera capture less light and the image is darker, but a longer exposure time for this region would be detrimental for the tip region. The compromise made here explains the lower accuracy of the edge detection in the lower region. The result of the overall method is shown in Fig. 3.12. The margin of error of about $2.4 \cdot 10^{-5}$ m is inherently present.

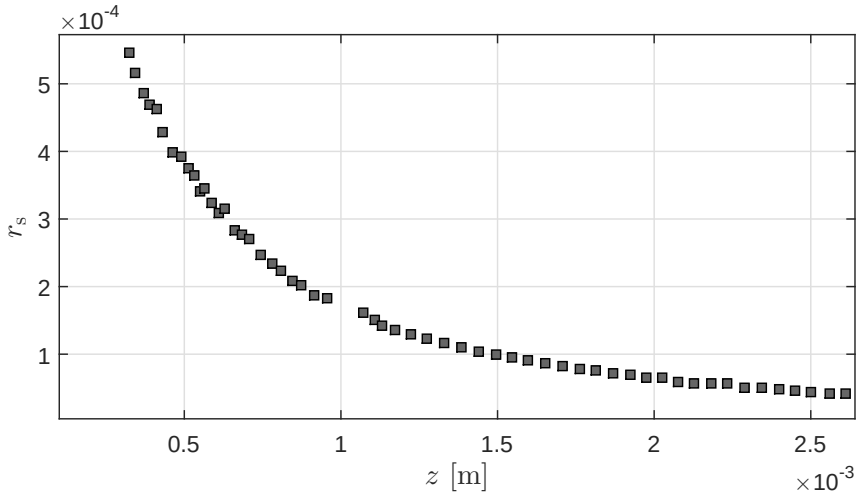

Figure 3.12: Radius r_s of the fiber meniscus as a function of z for the case $T_0 = 1350°\mathrm{C}$ and $2r_f = 35$ μm.

3.7 Summary

This chapter provided an overview of the capabilities of the single tip bushing position, which is used to support the physical modeling effort. The device can draw a single fiber from a glass melt covering a bushing temperature range from 1230°C to 1350°C, while the winder velocity can reach a maximum value of 3000 m/min. This corresponds to a fiber with a diameter 3-4 μm.

Following quantities are measured: the final fiber radius r_f, the flow rate Q_0, the tip temperature T_0, the axial variation of the ambient air temperature $T_{\mathrm{ext,conv}}(z)$, and the axial distribution of the meniscus radius r_f in the vicinity of the tip. Some of these measurements are used as input parameters for the model (Q_0, T_0, $T_{\mathrm{ext,conv}}(z)$), while others ($r(z)$, r_f) provide data for validation of the simulation results. For some of these quantities (T_0, r_f), several measurement techniques have been considered. Furthermore, the conservation of mass that relates the tip temperature, the drawing velocity and the

volume flow rate has been validated by comparing direct measurements to indirect calculations. In particular, it was shown that the decrease in flow rate over the duration of the experiments can be neglected.

The different sources of measurement errors are discussed and margins of error are provided. The limited accuracy of the measurements stems from the small scales and large temperatures involved in the process.

In conclusion, the experimental unit represents a very useful tool to support the modeling effort. Although the quantities that can be measured and their respective accuracy are limited, several assumptions of the model could be validated. Moreover, several input parameters could be determined. The validation of the numerical model with the measurements is discussed chapter 5.

Chapter 4

Numerical approach

The mathematical models describing the fiber drawing process have been presented in Chapter 2. Both the two-dimensional model, including or not the internal radiation and the air environment, and the simplified one-dimensional model are too complex to be solved analytically, and thus require a numerical solution. Numerical simulations have been performed with the two commercial software, ANSYS Polyflow and ANSYS Fluent, except for the one-dimensional model, for which an in-house code has been developed. This chapter gives a brief overview of the underlying numerical methods, discusses numerical parameters and simulation strategies, and presents convergence studies.

Section 4.1 is dedicated to the one-dimensional model. The numerical scheme based on a finite difference method, is presented including convergence tests. The next section focuses on the numerical solution of the two-dimensional model where only the fiber is considered (i.e. without internal radiation and surrounding environment). This is done with ANSYS Polyflow, which is based on a finite-element method. Section 4.3 deals with numerical and implementation aspects regarding the surrounding air flow model and its coupling with the model of the fiber, while Section 4.4 presents the specific method used to solve the internal radiation within the fiber.

4.1 Numerical solution of the one-dimensional model

The one-dimensional model, derived in Section 2.3, is based on different approximations leading to a simplified form of the governing equations (Eqs. (2.36)-(2.39)). In particular, the model involves an ordinary differential equation for the energy conservation (Eq. (2.39)), which needs to be solved numerically. This initial-value problem can be discretely integrated along the axial coordinate z using a 4th order Runge-Kutta scheme. This scheme has been chosen as it has good accuracy and stability properties, while still being explicit. Note however that the temperature along the fiber depends on the final

value of the fluidity φ_f so that an iterative procedure is required. The discretization and the iterative method are first presented, and the convergence is then discussed.

4.1.1 Numerical scheme

The energy equation, Eq. (2.39), is of the form

$$\frac{\mathrm{d}T(z)}{\mathrm{d}z} = M(T,z), \tag{4.1}$$

where M depends on the temperature T and axial coordinate z as

$$M(T,z) = -\frac{2\pi r_0}{\rho c_p Q_0}\dot{q}_\mathrm{s}(z)\left(\frac{v_\mathrm{f}}{v_0}\right)^{-\varphi(z)/2\varphi_\mathrm{f}} . \tag{4.2}$$

The computational domain is discretized from $z = 0$ to $z = L$ into N+1 points with a constant spatial spacing $\Delta z = L/N$, such that $z_n = n\Delta z$ with $n = 0, 1, 2..., N$. Knowing the temperature T_n at z_n, temperature T_{n+1} at node z_{n+1} is obtained by

$$T_{n+1} = T_n + \frac{\Delta z}{6}\left[k_1 + 2k_2 + 2k_3 + k_4\right], \tag{4.3}$$

where the Runge-Kutta coefficients k_i are

$$\begin{aligned}
k_1 &= M(z_n, T_n), && (4.4)\\
k_2 &= M(z_n + \frac{\Delta z}{2}, T_n + \frac{\Delta z}{2}k_1), && (4.5)\\
k_3 &= M(z_n + \frac{\Delta z}{2}, T_n + \frac{\Delta z}{2}k_2), && (4.6)\\
k_4 &= M(z_n + \Delta z, T_n + \Delta z k_3). && (4.7)
\end{aligned}$$

Starting from the initial condition at the tip, $T_{n=0} = T_0$, the temperature is solved for each n, until $n = N$.

In order to avoid numerical stiffness when approaching the transition region, the value of the viscosity is limited

$$\log_{10}\eta_n(T_n) = \begin{cases} \log_{10}\eta_\infty + \frac{B}{T_n - T_\mathrm{c}}, & \text{if } T_n \geq T_\mathrm{g}, \\ 12, & \text{if } T_n \leq T_\mathrm{g}, \end{cases} \tag{4.8}$$

where η_∞, B and T_c are given in Table 2.2. In other words, the viscosity increases with decreasing temperature until transition, after which it remains constant at $\eta(T_\mathrm{g}) = 10^{12}$ Pa·s (see also Section 2.4.1).

Equations (2.36)-(2.38) are evaluated as

$$v_n = v_{n=0} \left(\frac{v_N}{v_{n=0}} \right)^{\varphi_n/\varphi_N} , \tag{4.9}$$

$$r_n = r_{n=0} \left(\frac{v_N}{v_{n=0}} \right)^{-\varphi_n/2\varphi_N} , \tag{4.10}$$

$$\tau_{zz,n} = \frac{3}{\varphi_N} v_n \ln \left(\frac{v_N}{v_{n=0}} \right) . \tag{4.11}$$

The velocities $v_{n=0}$ and v_N are given by the boundary conditions

$$v_{n=1} = v_0, \tag{4.12}$$

$$v_{n=N} = v_\mathrm{f}, \tag{4.13}$$

where v_f is the winder velocity and v_0 is the velocity at the tip. The latter value is calculated using the conservation of mass, written as

$$v_0 = Q_0/\pi r_0^2, \tag{4.14}$$

where $r_0 = r_{n=0}$ is the tip radius and Q_0 is the flow rate.

The integral in the calculation of the fluidity φ_n is evaluated using the trapezoidal method

$$\varphi_n = \int_0^{z=n\Delta z} \frac{1}{\eta} dz \approx \frac{1}{2} \sum_{i=1}^{n} (z_i - z_{i-1}) \left[\frac{1}{\eta(T_i)} - \frac{1}{\eta(T_{i-1})} \right]. \tag{4.15}$$

Finally, the last quantity to calculate is the final value of the fluidity $\varphi_N = \varphi_\mathrm{f}$, from Eq. (2.35). However, its value is unknown *a priori*. Because each variable depends on this value, i.e. an integral over the entire computational domain, an iterative method is necessary. An arbitrary value for φ_f is first chosen, the problem is then solved numerically and a new guess for φ_f is computed. The procedure is repeated until convergence is reached.

4.1.2 Convergence

The spatial discretization Δz must be sufficiently small in order to obtain an accurate solution. Moreover, the iterative process should converge towards a constant solution. Simulations with decreasing values of Δz have been performed for a case with realistic process conditions on a computational domain of size $L = 0.08$ m (case B in Table 5.1,

with $T_{\text{ext,rad}} = 200°\text{C}$ and $T_{\text{ext,conv}} = 300°\text{C}$). The results are presented in terms of the

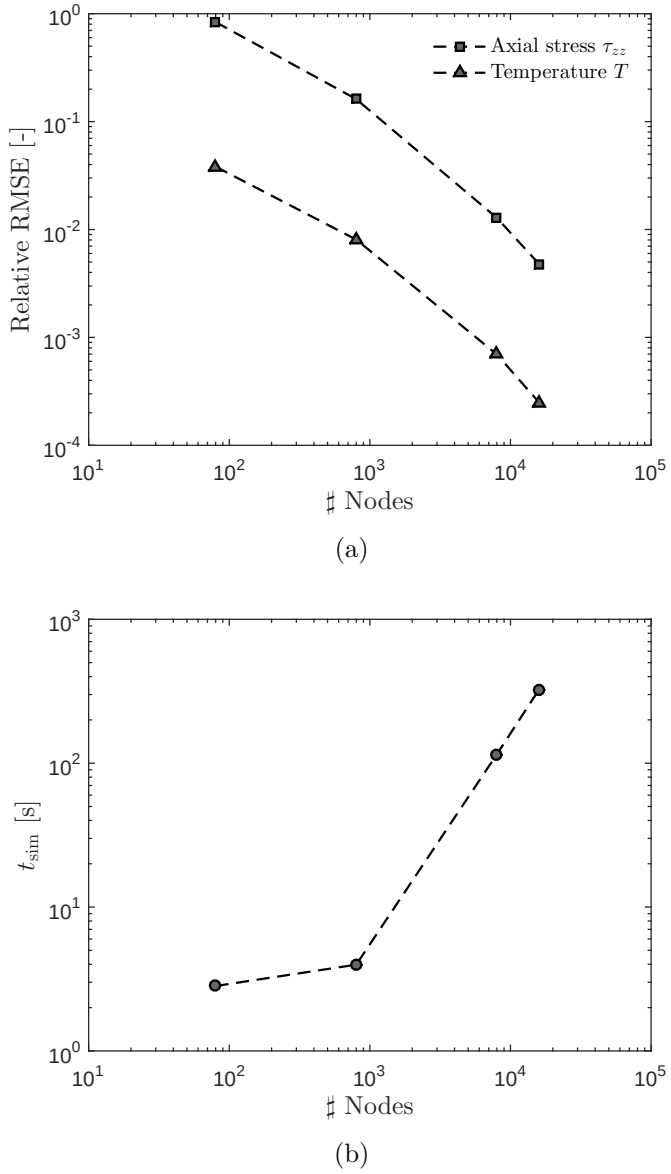

Figure 4.1: The relative root mean square error (a) and duration of the simulation t_{sim} (b) as a function of the number of nodes used for solving the one-dimensional model. The iterative process is assumed to have converged when the relative change of the solution between two iterations is below the threshold value of 10^{-6}.

axial stress because it takes into account both the drawing ratio v_{f}/v_0 and the cooling through the fluidity φ_{f}. Moreover, the stress $\tau_{zz,\text{f}}$ is the most sensitive variable due to its proportionality to $1/\varphi_{\text{f}}$. For this mesh convergence study, the iterative process is assumed to have converged when the relative change of the solution between two iterations is below the threshold value of 10^{-6}. The adequacy of this value is analyzed further below.

The absolute Root Mean Square Error (RMSE) on a variable field ϕ ($= \tau_{zz}$ here) is

calculated for each Δz, by

$$\text{RMSE} = \sqrt{\frac{\sum_{n=0}^{N} \left(\phi_n - \bar{\phi}_n\right)^2}{N}}, \tag{4.16}$$

where $\bar{\phi}_n$ should be the exact solution at position z_n. However, this solution is not know and thus is assumed to be the solution where Δz tends to zero (approximated as the solution with $\Delta z = 2.5 \cdot 10^{-6}$ m, which corresponds to $N = 32'000$ points). The relative RMSE can be evaluated by divided the absolute RMSE by the total variation of the stress $\tau_{zz,\text{f}} - \tau_{zz,0} \approx \tau_{zz,\text{f}}$ ($\tau_{zz,0} \approx 10^3$ is much lower than $\tau_{zz,\text{f}} \approx 10^7$). The results, including the required simulation time, are shown in Fig. 4.1 and summarized in Table 4.1. The relative RMSE for the temperature field has been also calculated. Both the temperature T and the stress τ_{zz} converge as Δz increases. It is interesting to notice that although the number of points is multiplied by a factor of 2, the simulation time increases by a factor 2.8 between $N = 8'000$ and $N = 16'000$, and 3.8 between $N = 16'000$ and $N = 32'000$. This is explained by the larger number of iterations required to satisfy the iteration convergence criterion. Note that the code was not optimized for CPU time.

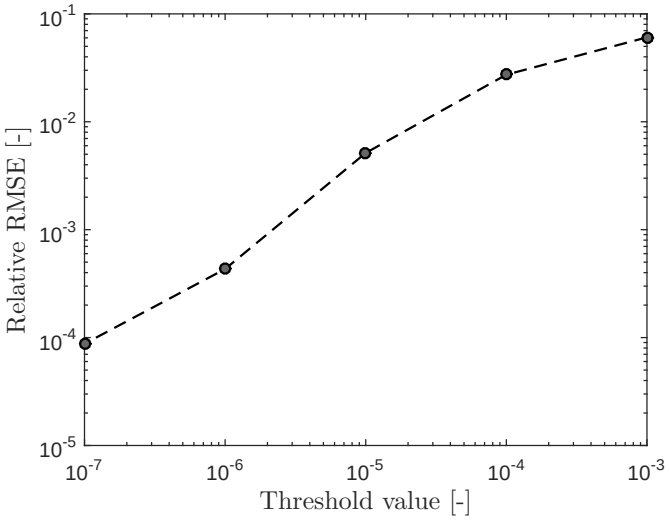

Figure 4.2: Relative root mean square error of the axial stress as a function of the convergence test used for solving the one-dimensional model.

The sensitivity of the results on the value of the threshold used as criterion to stop the iterative process is then analyzed. Several threshold values are considered, from 10^{-3} to 10^{-8}, with a mesh size $\Delta z = 2.5 \cdot 10^{-6}$ (corresponding to $N = 32'000$ grid points). The smallest value, 10^{-8}, is used as reference with respect to which the error is computed. The results are shown in Fig. 4.2. All results of the one-dimensional problem in the

Δz [m]	N	t_{sim} [s]	Relative RMSE τ_{zz}	Relative RMSE T
$1 \cdot 10^{-3}$	80	2.8	$8.4 \cdot 10^{-1}$	$3.8 \cdot 10^{-2}$
$1 \cdot 10^{-4}$	800	3.9	$1.6 \cdot 10^{-1}$	$8.1 \cdot 10^{-3}$
$1 \cdot 10^{-5}$	8000	115.3	$1.3 \cdot 10^{-2}$	$6.9 \cdot 10^{-4}$
$5 \cdot 10^{-6}$	16'000	326.2	$4.8 \cdot 10^{-3}$	$2.5 \cdot 10^{-4}$
$2.5 \cdot 10^{-6}$	32'000	1256.8	-	-

Table 4.1: Summary of the mesh convergence study for the one-dimensional model. The iterative process is assumed to have converged when the relative change of the solution between to iterations is below the threshold value of 10^{-6}.

next chapters are based on a discretization of the domain with $N = 16'000$ points and a threshold value for the iterative process of 10^{-6}. This choice provides a good trade-off between accuracy and computational cost.

4.2 Numerical solution of the two-dimensional model

The two-dimensional axisymmetric model derived in Section 2.2 is more complex, which adds new challenges to its numerical treatment:

- Because the position of the free surface is an output of the model, the geometry needs to be recalculated during the simulation.
- The high drawing ratio ($r_\mathrm{f}/r_0 \approx 10^2$) introduces large variations of length scales along the domain, which can be critical for the uniformity and the quality of the mesh.
- The viscosity law (Eq. (2.9)) is highly non-linear and the viscosity increases by ten orders of magnitude over the range of temperature considered. As a result, the numerical convergence is very sensitive to the temperature field. In particular, a small thermal variation can cause a large variation of the viscosity, and thus, has a strong impact on the flow and the position of the free surface.

The two-dimensional model is solved with the commercial software ANSYS Polyflow [60] as it is suited to deal with these challenges. Specifically developed for viscous and visco-elastic flows, this software has three main advantages: *i)* it can simulate free-surface flows, *ii)* large mesh deformations can be simulated through the evolution parameters

convergence method, *iii)* the physical properties of glass, such as the viscosity law, are already implemented. Nevertheless, the numerical convergence is still not straightforward and requires a robust methodology. This methodology is explained in Section 4.2.1. Then, the numerical method on which the solver is based is briefly presented in Section 4.2.2 with a specific focus on the numerical treatment of the free surface. Note that, since the code is commercial, the detailed implementation is not available. Finally, a mesh convergence study is discussed in Section 4.2.3.

4.2.1 Methodology

Since the final shape of the fiber is a priori unknown, an initial geometry is arbitrarily chosen. This geometry is then deformed during the calculation. Because the difference between the tip ($r_0 \approx 1$ mm) and the final diameter ($r_f \approx 10^{-2}$ mm) is large, the iterative procedure to solve the continuity equation can diverge. Figure 4.3 illustrates the evolution of the free surface from the initial guess (left) to its final shape (right) at the end of the simulation.

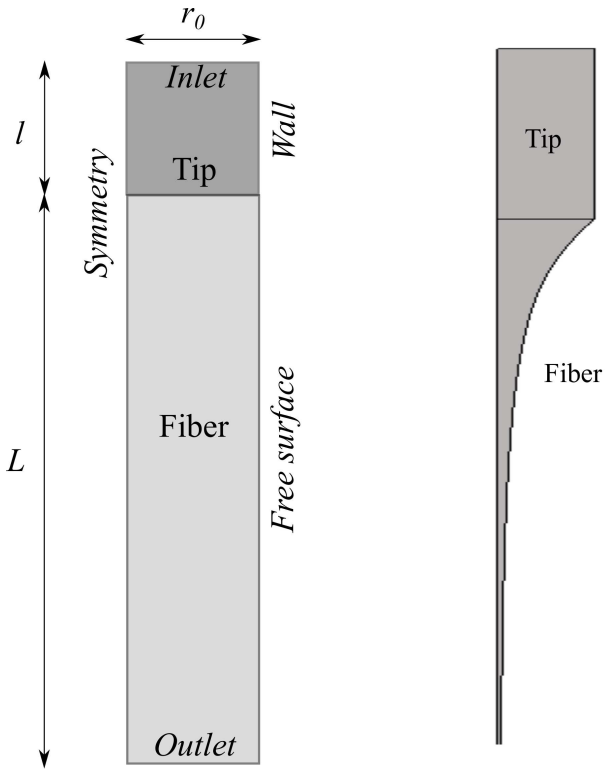

Figure 4.3: Initial geometry of the fiber before the start of the simulation (left) and final geometry of the fiber as a result of the simulation (right). Only the upper region of the computational domain is represented.

In order to facilitate convergence, a multi-step simulation strategy has been developed,

that gradually adds complexity:

1. The initial geometry is defined as a rectangle with dimensions $r_0 \times (L + l)$, as illustrated in Fig. 4.3 (left). The upper and lower part of the domain correspond to the tip (fixed domain) and the fiber (with a moving boundary), respectively.

2. The solution is then calculated for an isothermal process, providing a first deformation of the mesh. Because the ratio v_f/v_0 between the outlet and the inlet velocity is of the order of 10^3, intermediate solutions are calculated for increasing values of the outlet velocity. The starting value is $v_\mathrm{f} = v_0$ to avoid any motion of the free surface and thus, any mesh deformation. Then, a new solution is calculated for a slightly larger value of v_f where all fields are initialized with the previous solution (velocity, temperature, pressure and coordinates). This step is repeated until the required value of v_f is reached. This allows a gradual deformation of the mesh to ensure convergence.

3. From this converged isothermal solution, the non-isothermal case is computed with a temperature-dependent viscosity but without a heat flux at the fiber surface. This provides a constant temperature and viscosity field as initial condition for the next step. The main motivation is to avoid temperatures close to T_c that would lead to an infinite viscosity (see Eq. (2.9)) and large viscosity variations during the iterations of the next step.

4. The convective heat flux (i.e., the convective coefficient h) is gradually increased to avoid large mesh deformations caused by the high sensitivity of the viscosity on the temperature.

5. Finally, the radiative heat flux is also considered to obtain the final solution, as illustrated in Fig. 4.3 (right).

A converged simulation can then be used as initial guess for a new case, as long as the case parameters do not change too dramatically. In practice this is possible if the position of the free surface does not change too much. Otherwise, a multi-step strategy is also required to achieve convergence.

4.2.2 Numerical method

The solver in Polyflow is based on the finite element method (FEM) to solve the partial differential equations (2.1)-(2.3). The details of the numerical method and of its implementation are not described here, but some specific numerical aspects are briefly

summarized. The domain is divided into a certain number of elements. The differential equations are approximated into a set of algebraic equations for each of those elements. Then, all the elements are assembled leading to a non-linear matrix system of algebraic equations. The solution of the system provides the variable fields at the nodes of the elements. This method is based on shape functions, which are used to interpolate the solution between the nodes. Quadratic functions are used for the velocity and temperature, and linear functions for the pressure. This choice respects the Ladyzenskaja-Babuska-Brezzi (LBB) criterion ensuring numerical stability [61]. Furthermore, they represent a good compromise between computation time and accuracy, as the problem is two-dimensional. A Petrov-Galerkin formulation is used to relate the test and shape functions, but the Streamline Upwind Petrov-Galerkin (SUPG) method can also be chosen for the temperature field to provide upwinding for more stability. The resulting velocity-pressure formulation can be seen as an optimization problem under constraints due to the presence of the pressure, which is solved by the Lagrange multipliers. Specifically, this pressure variable is considered as a Lagrange multiplier. Finally, the solver for the matrix system is based on an Algebraic Multi Frontal (AMF) method, which is well-adapted to treat sparse matrix systems. A good review of the finite element method for fluid mechanics can be found in the book of Zienkiewicz *et al.* [62].

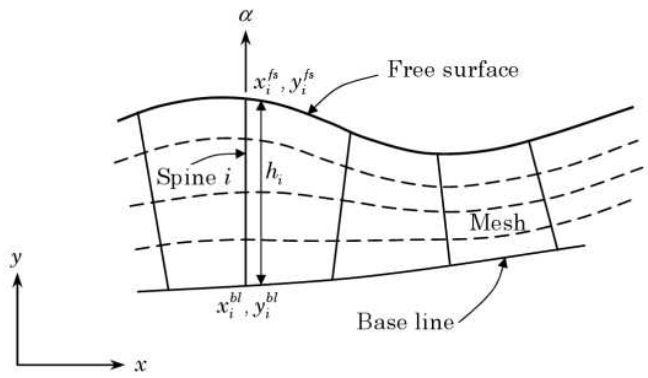

Figure 4.4: Schematic of the spines method (taken from [61]).

Because the position of the free surface is part of the solution, the initial mesh must be deformed during the computation. To account for the relative motion of the mesh, the conservation equations are expressed in an arbitrary Langrangian-Eulerian formulation [63]. Additionally, the position of the interior mesh nodes needs to be re-calculated at each iteration. For this two-dimensional problem, a structured mesh can be used. Mesh deformation is achieved through the method of spines, in which nodes are allowed to move along lines, called spines, adding thereby one degree of freedom. These spines are defined in the direction normal to the surface, as shown in Fig. 4.4. The two extremities of the

spines are the nodes (x_i^{bl},y_i^{bl}) on the base line (i.e., the symmetry axis here) and the nodes of the moving surface

$$x_i^{\text{fs}} = \alpha_{x,i} h_i + x_i^{\text{bl}}, \tag{4.17}$$

$$y_i^{\text{fs}} = \alpha_{y,i} h_i + y_i^{\text{bl}}, \tag{4.18}$$

where $\alpha_{x,i}$ and $\alpha_{y,i}$ are the directions of the spines and h_i the length of spine i. The position of the interior nodes, moving along the spines, is re-calculated proportionally to the displacement of the boundary nodes. More details about the method can be found in the book of Reddy and Gartling [61].

4.2.3 Convergence

In order to assess the mesh convergence, three different meshes with an increasing number of elements and nodes have been considered, as summarized in Table 4.2. The same case is used as for the one-dimensional model (case B in Table 5.1 with $T_{\text{ext,rad}} = 200°\text{C}$ and $T_{\text{ext,conv}} = 600°\text{C}$). Convergence is evaluated based on the temperature T_{s} and stress $\tau_{zz,\text{s}}$ evaluated at the free surface. The relative root mean square error is calculated through Eq. (4.16) (with $\phi = \tau_{zz,\text{s}}$ and T_{s}) where the reference solution has been obtained with mesh 4 as an approximation of the exact solution (see Table 4.2).

Mesh	♯ nodes	♯ elements	t_{sim} [s]	Relative RMSE T_{s}	Relative RMSE $\tau_{zz,\text{s}}$
Mesh 1	11′506	10′450	58	$1.2 \cdot 10^{-5}$	$2.7 \cdot 10^{-4}$
Mesh 2	29′504	27′645	298	$6.9 \cdot 10^{-6}$	$1.6 \cdot 10^{-4}$
Mesh 3	64′386	61′300	552	$2.3 \cdot 10^{-6}$	$8.8 \cdot 10^{-5}$
Mesh 4	251′371	245′200	4301	-	-

Table 4.2: Summary of the mesh convergence study results for the two-dimensional model.

The number of elements for this specific mesh is considered sufficiently high to reach a solution close to the exact one. The three smaller meshes are compared to the finest mesh (Mesh 4) using the RMSE. For these calculations, the convergence criterion for iterations is set to 10^{-7}. It is defined as the highest variation of the velocity, temperature and surface coordinates between two iterations over all the nodes. The results for the temperature and the axial stress are shown in Fig. 4.5. One can clearly see the overall error decreases when the mesh is refined. The calculation time is difficult to evaluate due to the different

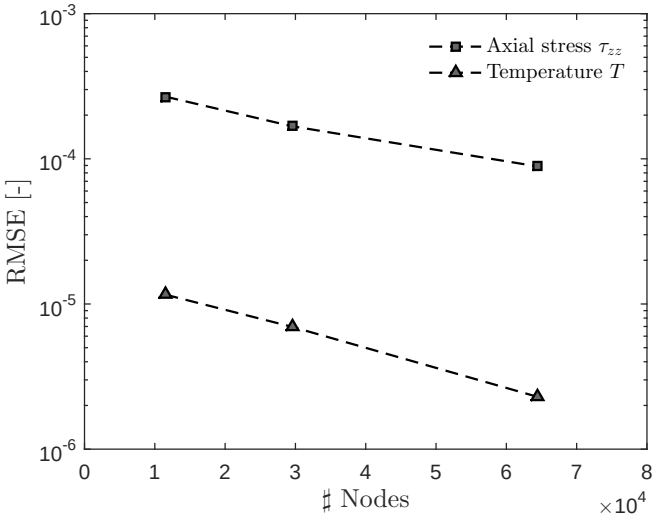

(a)

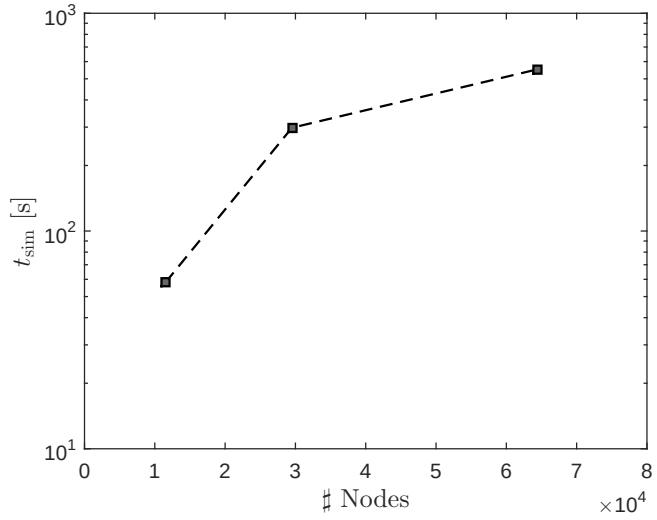

(b)

Figure 4.5: Relative root mean square error of the axial stress $\tau_{zz,\mathrm{s}}$ and temperature T_{s} taken at the free surface (a) and the computational time t_{sim} (b) as a function of the number of mesh nodes used for solving the two-dimensional model.

manual steps involved in the convergence. Nevertheless, the time considered here is the time required for the final step 5 in Section 4.2.1 so as to provide an estimate of the overall computational cost. Based on these results, the coarsest mesh provides sufficiently accurate results while keeping the computational cost affordable. Mesh 1 is thus used to solve the two-dimensional axisymmetric model in the following chapters.

4.3 Numerical implementation of the ambient air flow model

The numerical solution of the RANS equations governing the air flow around the fibers (see Section 2.5) requires a different solver than for the fiber. In particular, these simulations are performed with ANSYS Fluent, which is well-adapted for flows at high Reynolds numbers. Since the aim is to study the heat exchange between the fiber and the environment, a coupling between the fiber and the air model is necessary. However, Fluent cannot solve a free-surface problem by re-meshing. Consequently, a coupling between the two solvers Polyflow and Fluent is needed. This coupling introduces two main challenges: *i)* the meshing technique of the domain is different and cannot be used from one solver to the other, *ii)* Fluent is based on the finite volume method where the solution is calculated at the center of the mesh cells while Polyflow uses the finite element method in which the solution is defined at the mesh nodes. To overcome these challenges, an iterative approach is used that consists in solving sequentially the fiber and air flow models with their respective solver.

First, the methodology of the coupling is presented in Section 4.3.1. Section 4.3.2 then briefly describes the numerical method used by Fluent. Finally, convergence aspects are discussed in Section 4.3.3.

4.3.1 Methodology

The objective of the coupling is to determine the convective heat transfer between the fiber and the environment, avoiding thus the need for an empirical correlation. In particular, the details of the air flow, including the velocity and thermal boundary layers, are computed with Fluent. Knowing the air temperature gradients at the fiber surface directly provides the convective heat flux, from which the convective heat flux coefficient $h(z)$, can also easily be obtained. Since the convective heat flux between the fiber and the air depends on the fiber surface temperature, which itself depends on the convective heat flux, the process must be iterated until convergence. As illustrated in Fig. 4.6, the main steps of the iterative process are:

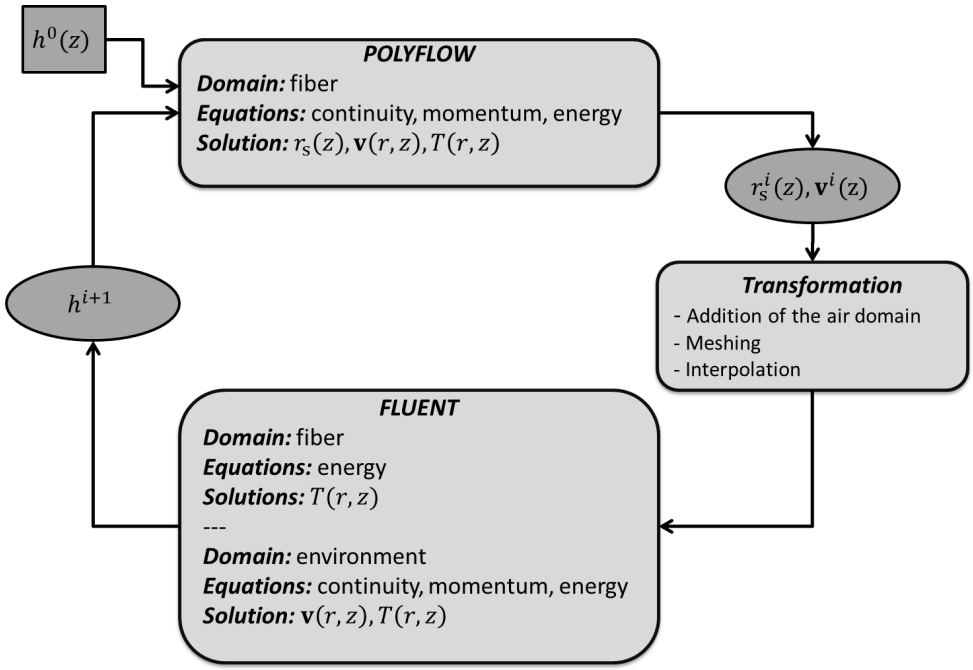

Figure 4.6: Schematics of the iterative coupling between Polyflow and Fluent.

1. The two-dimensional model of the fiber is first solved with Polyflow following the methodology described in Section 4.2. In this initial step, the empirical correlation of Kase and Matsuo, Eq. (2.23), is used to determine the convective heat transfer coefficient $h(z)$.

2. The radius of the fiber (i.e., the free surface) and the glass velocity field, but not the glass temperature field, are transferred to Fluent.

3. Since Fluent cannot deal with free surfaces, the position of the fiber surface obtained with Polyflow defines a new, fixed geometry in Fluent. The computational domain in Fluent includes thus both the fiber and the air environment. Because the shape of the fiber depends on the glass velocity field, this velocity field obtained with Polyflow is imposed in Fluent. Polyflow being node-centered, while Fluent is cell-centered, a new mesh is created in Fluent, not only for the air, but also for the fiber. The glass velocity field transferred from Polyflow must therefore be interpolated onto the Fluent mesh.

4. Fluent is then used to compute on the one hand the air flow by solving the Reynolds-averaged continuity, momentum and energy equations, and on the other hand, the glass temperature field only, by solving the energy equation in the glass phase. This step provides the convective heat flux along the fiber surface, from which an improved estimation of the convective heat transfer coefficient $h(z)$ is calculated.

5. As a change of the heat flux at the fiber surface modifies the glass velocity and temperature fields, and thus the position of the free surface, a new calculation of the fiber is performed with Polyflow using the updated value of $h(z)$ obtained from Fluent.

6. Steps 2 to 5 are repeated until convergence is reached.

4.3.2 Numerical method

Fluent solves the steady-state RANS equations based on the finite volume method, which takes advantage of the integral form of the conservation laws. Because a steady incompressible flow is considered, a projection method using a pressure-based algorithm (SIMPLE) is used to solve for the pressure and ensure a divergence-free velocity field [64]. Moreover, an iterative procedure is required to deal with the non-linearity and coupling of the equations.

The discrete solution is defined at the cell centers. The fluxes at cell faces are computed using a second-order upwind scheme for the transported quantities and a second-order scheme for the pressure. The evaluation of the different variables at the cell faces is based on a least-square approximation of the gradients.

4.3.3 Convergence

Since an iterative process between Polyflow and Fluent is required, the convergence of the coupling is first analyzed, then the mesh convergence is discussed. For these two studies, case C in Table 5.1 is chosen with $T_{\text{in}} = 300°\text{C}$ (see Fig 2.17).

Convergence of the coupling

The convergence is assessed by calculating the relative error on the convective heat transfer coefficient h between two consecutive iterations (i.e., the error at iteration k is thus given by $error_k = (h_k - h_{k-1})/h_k$). Since h is a function of z, two errors are calculated: the average over the fiber surface (mean relative error) and the error at the outlet (final relative error). Figure 4.7 shows the evolution of both errors as a function of the number of iterations. Both measures of the relative error reach about 1% after 5 iterations. Further iterations would be optimally necessary for a fully converged solution. However, the overall procedure is computationally very expensive and the convergence rate strongly decreases. This slow convergence could be due to a systematic error induced by the interpolation of the velocity field obtained with Polyflow onto the Fluent mesh. As the solution of the air

flow model only aims to assess the accuracy of the empirical correlation, the convergence level obtained after 5 iterations is considered sufficient.

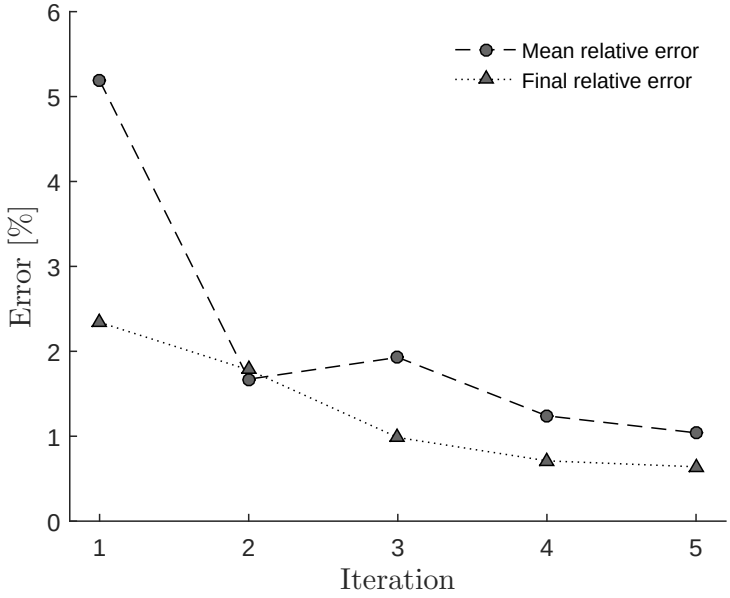

Figure 4.7: Convergence of the coupling between Polyflow and Fluent based on the convective coefficient $h(z)$. Two different relative errors are represented as a function of the number of iterations: for h averaged over z and for h evaluated at the outlet.

Mesh convergence study

The impact of the mesh resolution is quantified by comparing the solution obtained on three different meshes with an increasing number of elements, from 65′450 for the coarsest to 421′800 for the finest (see Table 4.3). Convergence is assessed by comparing the averaged temperature and the air velocity at the outlet of the domain obtained on the finest mesh with the solution on the two coarser meshes. More specifically, a relative error is defined as the absolute error between two meshes divided by the maximum variation of the corresponding quantity along the outlet boundary. This provides thus an estimate of the numerical error with respect to the maximum variation of both quantities.

The results are summarized in Table 4.3. The variation between the coarsest and the finest mesh (mesh 1 and mesh 3, respectively) is about 5% for both outlet velocity and mean temperature. On the other hand, the relative error between mesh 2 and mesh 3 decreases to 1.3% for the mean temperature and 1.9% for the outlet velocity, which is of the same order of magnitude as the coupling error discussed previously. The intermediate mesh with $26 \cdot 10^4$ elements is thus chosen as a good compromise between accuracy and cost.

Mesh	♯ nodes	♯ elements	e_T [%]	e_v [%]
Mesh 1	66′456	65′450	4.8	5
Mesh 2	259′235	257′232	1.3	1.9
Mesh 3	424′266	421′800	-	-

Table 4.3: Mesh convergence study for the ambient air flow computation.

4.4 Computation of internal radiation

The solution of the radiative transfer model, governed by Eq. (2.60), provides an estimate of the radiative intensity within the medium. Since the aim is to compute the radiative flux from it, the calculation involves the integration of the intensity over the total solid angle. Numerically, this implies that not only the space, but also the solid angles must be discretized, which adds complexity to the problem. Furthermore, if the medium is non-grey, the integration over the continuous spectrum of wavelengths is required. As described in Chapter 2, the spectrum is divided into bands, in which the coefficient of absorption is constant. The intensity is thus calculated for each band and each direction, and then integrated to obtain the radiative flux. Because this flux impacts the energy balance and thereby the temperature of the medium, the energy and radiative transfer equation are coupled.

Different numerical methods have been developed to solve the radiative transfer equation, such as the spherical harmonics method [65], the zonal method [66] or the Monte-Carlo method [67]. In the present work, internal radiation is solved with the Discrete Ordinate Method (DOM), first proposed by Chandrasekhar [68], and that is available in both ANSYS Polyflow and ANSYS Fluent. However, Polyflow is limited to grey bodies, i.e. where the intensity is considered constant over the entire spectrum of wavelengths. On the other hand, the temperature field cannot be directly imposed in Polyflow so that a full iterative coupling between Polyflow and Fluent, similar to the one used for the air flow model, is not possible. Due to these restrictions, two approaches are taken:

- The full problem, including internal radiation but with the assumption of a grey body, is solved in Polyflow. This approach cannot consider the variation of the absorption coefficient with the wavelength.

- A one-way coupling is used between Polyflow and Fluent. In this case, the solution obtained from the first approach is transferred to Fluent, where the energy equation and internal radiations are solved again, this time assuming a non-grey body.

However, the updated temperature field cannot be transferred back to Polyflow and no iterative process is possible.

The second approach is therefore only used to quantitatively assess the impact of the full internal radiation model on the heat flux compared to an internal radiation model with a grey medium assumption or with only a surface radiation model.

The next sections describe the discrete ordinate method, the angular discretization and the spatial integration. Then, Section 4.4.4 discusses the convergence for the angular discretization in both Polyflow and Fluent.

4.4.1 Discrete Ordinate Method

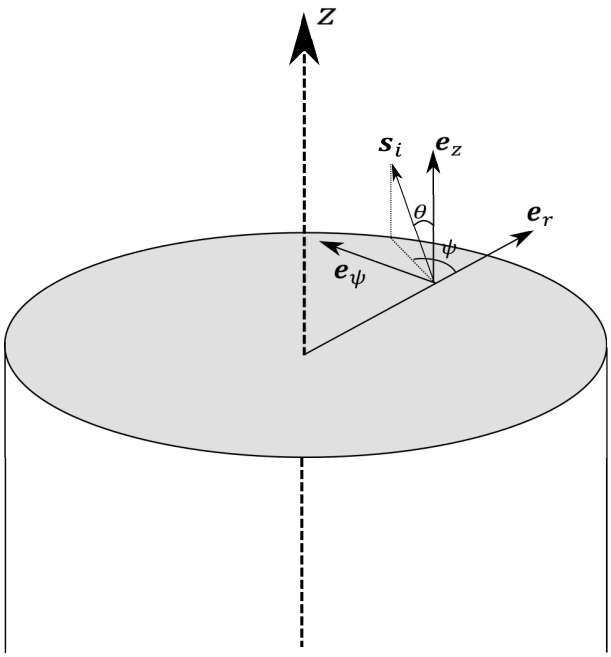

Figure 4.8: Schematics of the axysimmetric coordinates used in the formulation of the RTE (Eq. (4.19)) for the Discrete Ordinate Method.

In the Discrete Ordinate Method, the total solid angle is discretized into N different directions $\mathbf{s}_i$, where i denotes the direction considered. In cylindrical coordinates, Eq. (2.60), is rewritten for each direction $\mathbf{s}_i$ as [69]

$$\frac{\mu_i}{r}\frac{\partial\left(rI_{\lambda,i}\right)}{\partial r} - \frac{1}{r}\frac{\partial\left(\eta_i I_{\lambda,i}\right)}{\partial\psi} + \xi_i\frac{\partial\left(I_{\lambda,i}\right)}{\partial z} = \kappa_\lambda\left[n_\lambda^2 I_{\mathrm{b},\lambda} - I_{\lambda,i}\right], \tag{4.19}$$

where μ_i, η_i and ξ_i are respectively the component along the directions $\mathbf{e}_r$, $\mathbf{e}_\psi$ and $\mathbf{e}_z$ of

$\mathbf{s}_i$ (see Fig. 4.8) given by

$$\mu_i = \sin\theta_i \cos\psi_i, \tag{4.20}$$

$$\eta_i = \sin\theta_i \sin\psi_i, \tag{4.21}$$

$$\xi_i = \cos\theta_i. \tag{4.22}$$

The angular discretization is based on the choice of the directions μ_i, η_i and ξ_i or, equivalently θ_i and ψ_i. The optimal directions are discussed in the next section.

The radiative flux is calculated by integrating the intensity over the total solid angle (Eq. (2.61)). In the DOM method, this integral is approximated by numerical quadratures [51,55] leading to the following expressions for the radiative flux in the r and z directions and wavelength λ,

$$\dot{\mathbf{q}}_{\lambda,r} = \sum_{i=1}^{N} w_i I_{\lambda,i} \mu_i, \tag{4.23}$$

$$\dot{\mathbf{q}}_{\lambda,z} = \sum_{i=1}^{N} w_i I_{\lambda,i} \xi_i. \tag{4.24}$$

where w_i are weights associated to each direction $\mathbf{s}_i$. Since a band model is used for a non-grey medium, the total flux is the sum of the partial fluxes over all bands, such that

$$\dot{\mathbf{q}}_r = \sum_{j=1}^{N_{\text{band}}} q_{\Delta\lambda_j,r}, \tag{4.25}$$

$$\dot{\mathbf{q}}_z = \sum_{j=1}^{N_{\text{band}}} q_{\Delta\lambda_j,z}, \tag{4.26}$$

where $\Delta\lambda_j$ denotes the bandwidth and N_{band} is the total number of bands.

4.4.2 Angular discretization

The directions $\mathbf{s}_i$ can be chosen arbitrarily [70], but some choices lead to a better accuracy. The common approach for the angular discretization is called the S_N-approximation [68] that provides a set of directions according to a set of conditions. However, both Fluent and Polyflow are based on the Piecewise Constant Angular quadrature [71] in two dimensions, which is described here.

In the Piecewise Constant Angular method, the angles ψ and θ are uniformly discretized into N_ψ and N_θ elements respectively, such that [71]

$$\psi_m = (m-1)\Delta\psi, \tag{4.27}$$

$$\theta_n = (n-1/2)\Delta\theta, \tag{4.28}$$

where $m = 1, 2, ..., N_\psi$ and, $n = 1, 2, ..., N_\theta$, $\Delta\psi = 2\pi/N_\psi$ and $\Delta\theta = \pi/N_\theta$ in two-dimension. The weights are calculated as

$$w_{m,n} = \int_{\psi_{m-1/2}}^{\psi_{m+1/2}} \int_{\theta_{n-1/2}}^{\theta_{n+1/2}} \sin\theta_n d\theta d\psi. \tag{4.29}$$

4.4.3 Spatial integration

For each given direction, the resolution of the RTE requires the spatial integration of the intensity within the domain. The approach taken here ensuring energy conservation is to discretize the RTE through a finite volume method. By integrating the divergence terms over the volume δV, the volume integrals are transformed into surface integrals through Gauss theorem. The gradient of intensity in Eq. (2.60) is thus rewritten as

$$\int_{\delta V} \mathbf{s} \cdot \nabla I \mathrm{d}V = \int_{\delta V} \nabla \cdot (\mathbf{s}I)\, \mathrm{d}V = \int_S I\mathbf{s} \cdot \mathbf{n}\, \mathrm{d}S, \tag{4.30}$$

leading to

$$\int_{\Omega_i} \int_S I\mathbf{s} \cdot \mathbf{n}\, \mathrm{d}S\mathrm{d}\Omega = \int_{\Omega_i} \int_S \left(\kappa_\lambda I_{\lambda,\mathrm{b}} - \kappa_\lambda I\right)\, \mathrm{d}S\mathrm{d}\Omega, \tag{4.31}$$

where Ω_i is the integrated solid angle. As previously, the intensities within a volume δV and at the cell faces S are considered constant and interpolation schemes can be used to relate them [51]. The system is thus reduced to a set of algebraic equations that can be solved numerically.

4.4.4 Convergence

The solution accuracy depends on both the number of discrete directions $\mathbf{s}_i$ and on the spatial mesh discretization. The convergence of the RTE solution with increasing number of directions is assessed here in both Fluent and Polyflow.

Polyflow

In Polyflow, the total number N_{dir} of directions can be imposed (up to a maximum of 30), but not their respective repartition across the azimuthal and polar directions. Convergence is quantified by comparing the solution with $N_{\mathrm{dir}} = 4, 6, 8, 16$ directions with the solution obtained with $N_{\mathrm{dir}} = 30$ on mesh 1 in Table 4.2. For each case, the relative RMSE (Eq. (4.16)) is computed for the temperature T, intensity I and axial stress τ_{zz} at the free surface. The reference case corresponds to case B in Table 5.1 and the radiative properties are given in Table 2.3 for a grey body. The relative error is 10^{-6} for $N_{\mathrm{dir}} = 4$, and of the order of 10^{-10} for $N_{\mathrm{dir}} = 6$, suggesting that 6 directions are sufficient.

Additionally, the influence of the mesh resolution is quantified for $N_{\text{dir}} = 6$ by performing a mesh convergence study. The relative error on the temperature between the coarsest (mesh 1) and finest mesh (mesh 4) is $1.6 \cdot 10^{-5}$. This accuracy is considered sufficient and mesh 1 is used for all subsequent simulations.

Fluent

Fluent is only used here to investigate the effect of a non-grey model on the temperature. This solver allows to separately choose N_ψ and N_θ so that the total number of directions in two dimensions amounts to $4N_\psi \times N_\theta$. Because the velocity and the stress are obtained from Polyflow, only the temperature is analyzed (see Section 4.3.1). The same case is used as previously (case B in Table 5.1) and the radiative properties are given in Table 2.3 for the four-band model. A reference solution is obtained on mesh 2 in Table 4.3 with a fine angular discretization, i.e., $N_\psi \times N_\theta = 10 \times 10$, which corresponds to 400 directions. The relative error is $2 \cdot 10^{-2}$ % for $N_\psi \times N_\theta = 4 \times 4$ and $7 \cdot 10^{-3}$ % for $N_\psi \times N_\theta = 8 \times 8$. Consequently, a discretization with $N_\psi \times N_\theta = 4 \times 4$ (i.e., 64 directions) is chosen for the angular discretization. Using this value, the relative error between the two coarsest meshes and the reference mesh 3 (see Table 4.3) is $7.6 \cdot 10^{-3}$ and $4.3 \cdot 10^{-4}$, respectively. As for the ambient air flow, the intermediate mesh is considered in the next simulations.

4.5 Summary

This chapter has briefly summarized the numerical approach for solving the mathematical models developed in Chapter 2: *i*) the one-dimensional model for the fiber, *ii*) the two-dimensional axisymmetric model for the fiber, *iii*) the two-dimensional axisymmetric model for the ambient air flow, and *iv*) the semi-transparent model for internal radiation. Additionally, the influence of different numerical parameters (e.g., mesh resolution, iterative convergence criterion) has been quantified to determine their optimal value with respect to accuracy and computational cost. These optimal values are used for all subsequent simulations, unless otherwise specified.

The one-dimensional model is solved with an in-house Matlab code based on a finite difference scheme combined with an iterative procedure. A mesh with $N = 16'000$ points is chosen, while the iterative procedure is considered converged when the relative temperature change between two consecutive iterations is below 10^{-6}.

The standard two-dimensional axisymmetric model for the fiber (i.e., without the ambient air flow model and internal radiation) is solved with the commercial finite-element software ANSYS Polyflow. The mesh deformation imposed by the displacement of the free surface is based on the spine method. Because convergence is often tenuous, a manual

multi-step procedure has been developed for the most challenging cases. All following simulations are performed on mesh 1 in Table 4.2 with approximately 10′000 elements.

The temperature and velocity fields in the ambient air are computed with the finite-volume solver ANSYS Fluent. Because Fluent cannot treat the mesh and free-surface deformation, it is coupled to Polyflow through a sequential iterative procedure. In particular, Polyflow is used to compute the velocity field in the fiber and the position of its free-surface, while Fluent is used to compute the velocity field in the ambient air and the temperature field in both the ambient air and in the fiber. Due to specificities of the two solvers, two different meshes are used for the fiber, which imposes an interpolation step during the transfer of the solution between the two solvers. Mesh convergence study has shown that mesh 1 in Table 4.2 for Polyflow and mesh 2 in Table 4.3 for Fluent provide a good compromise between accuracy and computational cost. Moreover, a number of 5 coupling iterations seems to be adequate.

Finally, the radiative transfer equation of the semi-transparent model for internal radiation is solved with Polyflow if a grey assumption is used, and with Fluent otherwise. In the latter case, only a one-way coupling between Polyflow and Fluent is considered. In both cases, the Discrete Ordinate Method is used with a piecewise constant angular quadrature. As previously, the spatial discretization relies on mesh 1 in Table 4.2 for Polyflow and mesh 2 in Table 4.3 for Fluent. On the other hand, internal radiation computed with Polyflow is based on 4 angular directions and with Fluent on 64 angular directions.

In conclusion, the analysis of the present chapter has demonstrated that sufficiently accurate solutions can be obtained for the different mathematical models. These numerical tools are used in the following chapters to investigate several aspects of the physical modeling and to gain a more detailed understanding of the underlying physics.

Chapter 5

Analysis of the physical models

Before focusing on characterizing the break, it is important to assess the different physical models. In this context, the objectives of the present chapter are to understand the contributions of the different physical processes, to identify the limitations of the different models, and to quantify their sensitivity to process and material parameters. The results of this analysis provide the basis for a further investigation of the process discussed in Chapter 6. In particular, the goal is to determine which approximations or simplifications can be tolerated to still obtain meaningful results in the optimization of the process and the investigation of the fiber break. This is motivated by the large computational cost of a full model that incorporates all details of the physics. The four main models developed in Chapter 2 and solved with the numerical techniques described in Chapter 4 are analyzed in details: *i)* the two-dimensional axisymmetric model of the fiber, *ii)* the one-dimensional model, *iii)* the model of the surrounding air coupled to the fiber and finally*iv)* the internal radiative model added to the two-dimensional model.

The first section focuses on the two-dimensional model. After a validation with experimental data, the general solution for the field variables are presented including a characterization of the uncertainties related to the glass properties. Then, Section 5.2 discusses the accuracy of using a one-dimensional model to describe the process. The influence of the different physical forces and radial variations on the solution is assessed in this section. On the other hand, the results obtained by coupling the fiber and the surrounding air are discussed in Section 5.3. In particular, the accuracy of the correlation for the convective heat transfer coefficient is investigated in some details. Finally, Section 5.4 focuses of the influence of the internal radiation model coupled with the two-dimensional model.

5.1 Two-dimensional solution

The solution of the standard two-dimensional axisymmetric model developed in Section 2.2 and solved with the methodologies described in Section 4.2 is analyzed in this section. First, experimental measurements of the fiber radius along the axial direction are used to validate the model. The overall solution is also reported in details. Then, the sensitivity of the solution to the material properties is discussed, in particular in the light of the measurement errors of these properties (see Section 2.4). Finally, the impact of the viscosity law is assessed by comparing both the Fulcher and MYEGA models.

5.1.1 Experimental validation

The predictions of the two-dimensional computational model have been compared to experimental measurements for two different cases. The first one is taken from the work of Glicksman [4], and corresponds more specifically to his M5 case. The second case (referred to as case A in Table 5.1) is provided by measurements from the dedicated experimental unit described in Chapter 3. The process parameters are summarized in Table 5.1 (case B is closer to industrial production and is used in the next sections).

	Glicksman	Case A	Case B
Glass type	E-glass	Advantex©	Advantex©
Q_0 [mm^3/s]	3.171	0.486	1.67
r_0 [mm]	0.86	0.6	0.6
T_0 [°C]	1227	1325	1300
v_f [m/s]	25.88	1.55	21.3
r_f [μm]	6.2	10	5

Table 5.1: Process parameters and type of glass for the three cases considered in this study: volumetric flow rate Q_0, tip radius r_0, tip temperature T_0, drawing velocity v_f, and corresponding final radius r_f.

The process parameters of case A are slightly different from the ones in Glicksman experiment in order to test a different set of process conditions. In particular, the flow rate and drawing velocity are one order of magnitude lower. In addition, the glass material in case A is Advantex©, while Glicksman used another glass composition. As the compositions are different, the temperature of the melt required to reach the working point is in Glicksman's case lower and closer to a standard E-glass. In case A, the flow

rate is deduced from the measurement of the mass of the glass fibers produced during a 10 minute period. The tip temperature is calculated from the flow rate. Finally, the final diameter is measured on-line with the Keyence laser diffractometer.

It is important to recognize that, by mass conservation, the final fiber radius depends directly on the flow rate and drawing velocity, both of which are used as input parameters for the simulation. The final fiber radius is thus trivially predicted, and consequently does not represent a pertinent quantity for assessing the accuracy of the numerical predictions. The radius attenuation in the vicinity of the tip provides on the other hand a better validation measure. A comparison between measured and predicted values of the radius along the axial coordinate z is shown in Fig. 5.1. As the experimental data for the radius in this region relies on the post-processing of high-resolution images, a margin of error of about $\pm 2.4 \cdot 10^{-5}$ m is inherently present, as depicted by the error bars (case A). A good agreement between predicted and measured values is obtained for both cases. However, some discrepancies of the order of the margin of error can be observed close to the tip. As discussed later, radiative heat transfer dominates in this region. These discrepancies can be explained by the approximation made regarding the effect of the bushing plate, the internal radiation and in particular the value of the surface emissivity, and the inherent uncertainties on the glass properties (as discussed later). Although these results are not fully conclusive, they indicate that the two-dimensional model captures relatively well the radius attenuation in the tip region. Since the cone-shape of the fiber is very sensitive to all physical processes, it can be deduced that the most relevant contributions are rather adequately represented, but that some discrepancies still remain.

5.1.2 General solution

The predictions of the axisymmetric two-dimensional model are analyzed here from a physical point of view. The test case chosen is based on process conditions very similar to the industrial production of 10 μm fibers, referred to as case B in Table 5.1. The flow rate is obtained with a glass height $H = 0.35$ m and a tip radius $r_0 = 0.6$ mm. The glass properties are given in Table 2.2 where the different dependences on temperature have been taken into account. Due to numerical limitations, only a constant density is considered using the reference value at 1300°C. The sensitivity of the solution to the glass properties, and specifically to the density, is further investigated in Section 5.1.3.

The solution profiles for the temperature and the axial velocity at the free surface are shown in Fig. 5.2. The temperature of the fiber drops by more than 500°C over a distance of 8 cm before approaching the glass transition temperature ($T_g \approx 750°$). The heat fluxes responsible for this rapid cooling are represented in Fig. 5.3. Radiation is dominant in a

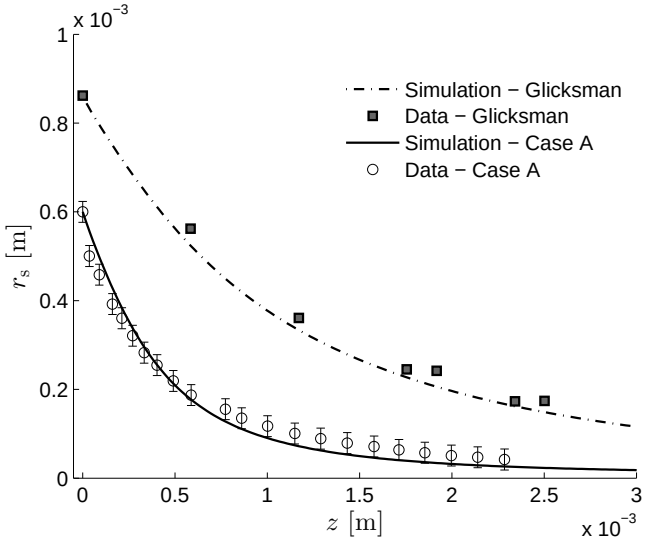

Figure 5.1: Comparison between the prediction of the two-dimensional model and experimental data for the fiber radius $r_s(z)$ as a function of the axial coordinate z in the region very close to the tip. The process parameters of the two cases are summarized in Table 5.1.

small region near the tip where the temperature is the highest and the radius the largest. As the temperature and radius decrease, just a few millimeters away from the tip exit, the convective flux becomes more important and exceeds the radiative flux. This results are consistent with those of Huynh [9] and Purnode [11].

On the other hand, the axial velocity increases rapidly to reach the winder velocity after about 3 cm and remains constant afterward, as the fiber reaches its final diameter (Fig. 5.2(b)). This plateau can easily be explained by considering the one-dimensional model of Section 2.3, and more specifically Eqs. (2.36)-(2.38). The rapid cooling is associated with a large increase in viscosity. As shown by Eq. (2.33), larger values of the viscosity (i.e., further downstream) contribute less and less to the fluidity φ, which then asymptotes to a constant value φ_f as defined by Eq. (2.35). This is illustrated in Fig. 5.4(a). Similarly, Fig. 5.4(b) shows that the axial stress rapidly grows until it reaches a constant value $\tau_{zz,f}$, as predicted by Eq. (2.38). These results demonstrate that the fiber experiences most of its variations (except for the temperature) within the first 3 cm. The practical implication is that this region is critical for controlling the process. Another interesting conclusion is that the one-dimensional model, despite its simplicity, provides an invaluable insight into the physics of the process.

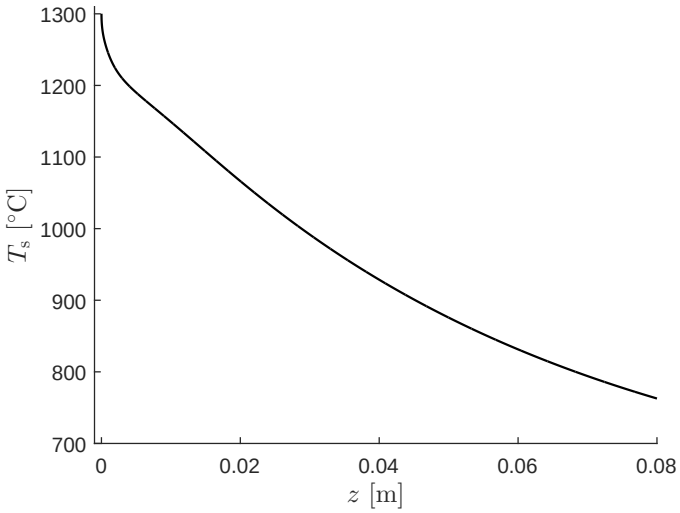

(a)

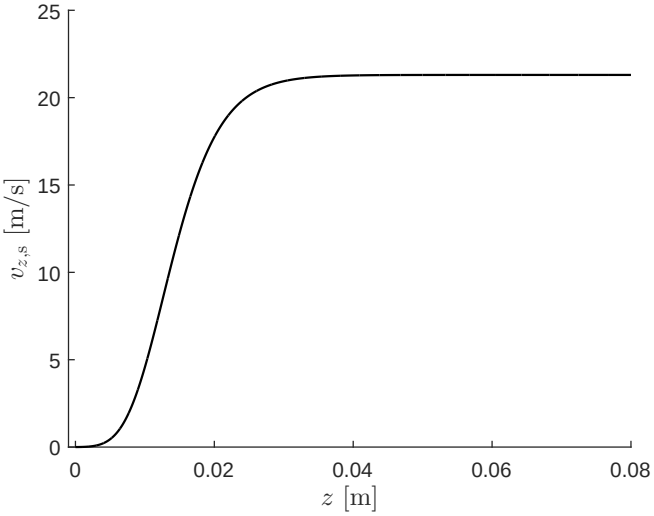

(b)

Figure 5.2: Temperature T_s (a) and axial velocity $v_{z,\mathrm{s}}$ (b) at the free surface as a function of the axial coordinate z obtained with the two-dimensional model for case B (see Table 5.1).

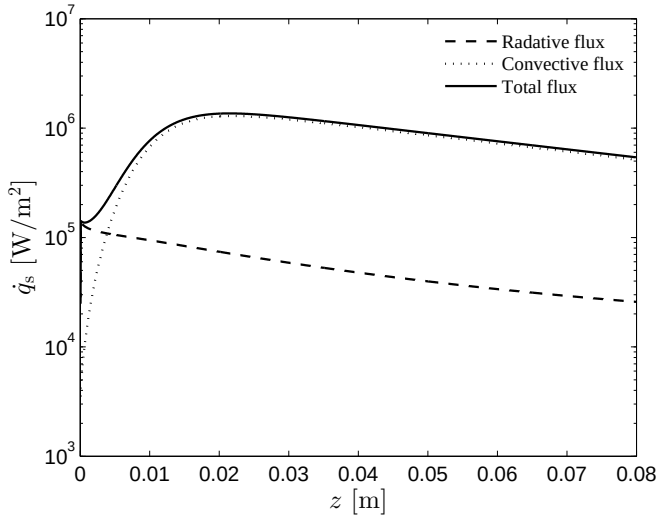

Figure 5.3: Radiative, convective and total heat fluxes at the free surface as a function of the axial coordinate z calculated with the two-dimensional model for case B in Table 5.1.

5.1.3 Sensitivity to glass properties

The model depends on the properties of the glass material (summarized in Table 2.2), which are inevitably affected by measurement errors. The sensitivity of the solution to these errors is investigated here. In addition, the response of the model to temperature-dependent properties compared to isothermal values is also assessed.

Impact of the error measurements

The impact of the material property measurement errors on the results of the physical model is studied independently for each property, where two solutions are calculated in each case by considering the lowest and the highest values of the error bar. The temperature dependence of the material properties is considered for all properties (except for the density and specific heat where the reference value at 1300°C is taken). The relative variation of the solution for each variable field, denoted by Δ, is calculated through the absolute difference between both cases, which is then divided by the maximal variation of the variable over z. As later demonstrated in Section 5.2, the radial variations are very small, so that all quantities are considered at the free surface along z. Since the error bars are different for each property, this study cannot be seen as a sensitivity study of the model to the glass properties, but only to the measurement errors. This specific point is treated in the next chapter.

The results are shown in Fig. 5.5 for the axial velocity, temperature and axial stress, and the impact is summarized as follows:

Density The error on the density measurement leads to a maximal uncertainty of $\sim 0.5\%$

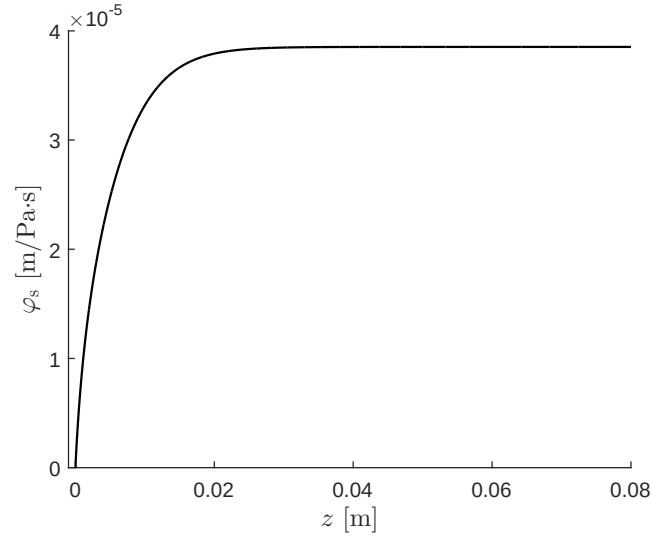

(a)

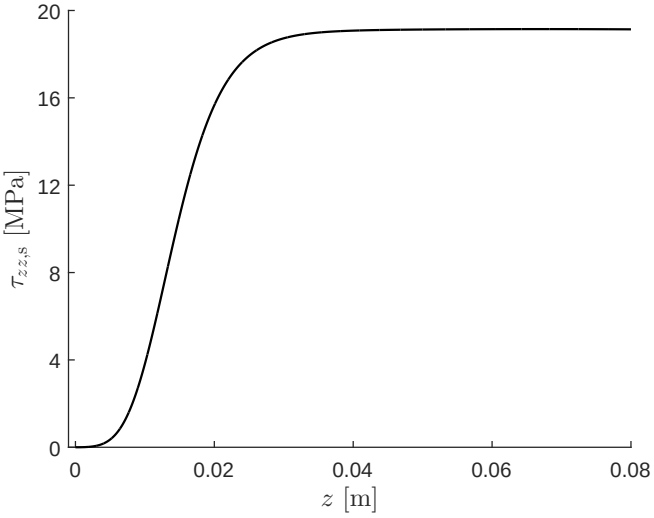

(b)

Figure 5.4: Fluidity φ (a) and axial stress τ_{zz} (b) at the free surface as a function of the axial coordinate z obtained with the two-dimensional model for case B (see Table 5.1).

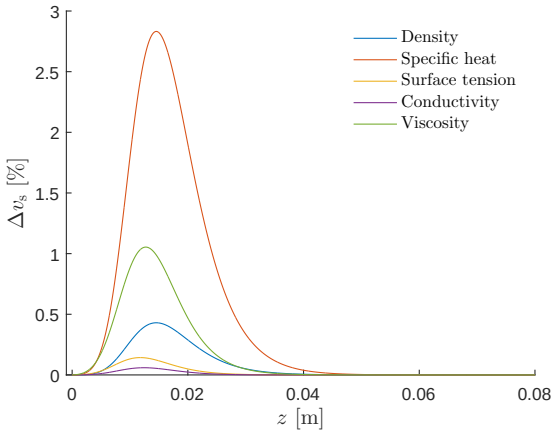

(a)

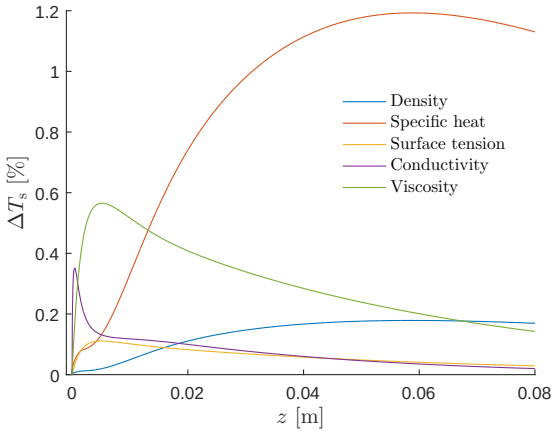

(b)

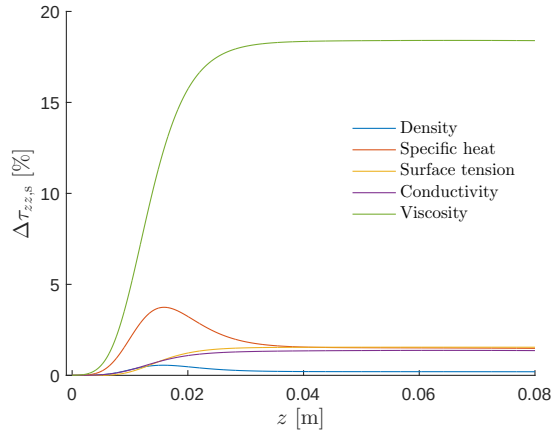

(c)

Figure 5.5: Variability of the axial velocity (a), temperature (b) and axial stress (c) at the free surface as a function of the axial coordinate z due to uncertainties in the glass property measurements. The relative variation Δ denotes the relative difference between simulations using the highest and lowest value of the error bar, divided by the maximum variation over z.

for the axial velocity and 0.2% for both temperature and axial stress.

Specific heat The error bar on the specific heat leads to maximum uncertainties of 3% for the velocity and 1.2% for the temperature. The uncertainty on the stress is also high with 3.5%.

Surface tension The effect of the error on surface tension measurements leads to a maximal variation of less than 0.5% on the velocity and the temperature, while it reaches 1.5% on the axial stress.

Conductivity A similar error magnitude as for surface tension is observed for the conductivity, except for the temperature peak very close to the tip.

Viscosity The difference on the final stress reaches almost 19%. The viscosity strongly depends on the temperature. A variation in the viscosity law leads, in particular, to a different viscosity at the tip for a given temperature. However, this value is the highest contribution in the calculation of the fluidity integral. As the stress is inversely proportional to the fluidity, a large impact is observed. However, this is mainly caused by a variation in the process conditions rather than a real uncertainty. Furthermore, the impact on the temperature and the velocity field are much lower with a maximum of 0.6% and 1%, respectively.

Overall, the impact of uncertainties on material properties is rather small. In particular, a $0-2\%$ uncertainty is observed on the final axial stress, which is the main quantity of interest in the context of fiber breaking.

Impact of the temperature dependence

It has be shown in Section 2.4 that several properties are temperature-dependent in the temperature range of the liquid state above the glass transition. In particular, the conductivity, emissivity, surface tension and density are found to vary linearly with temperature, while the viscosity has a logarithmic dependence. The impact of potentially neglecting this temperature dependence is investigated in this section. However, the viscosity is not included in the analysis since its temperature-dependence is primordial and could not be neglected. Furthermore, the temperature dependence of the emissivity is investigated in Section 5.4, which is dedicated to radiation.

Each property is studied independently from the others by performing two simulations: one with the property constant obtained for a temperature $T = 1300°C$, and one with the temperature dependence. The values used in each case are summarized in Table 2.2. These two solutions are then compared in the same way as previously: the difference of the variables, v_z, T and τ_{zz}, taken at the free surface along z, is calculated and then, divided by the total variation over the computational domain. The results for the surface tension and conductivity are shown in Figs 5.6(a) and 5.6(b), respectively. The temperature dependence of the density cannot be considered due to the solver limitation, but its sensitivity is discussed later. These results demonstrate that the impact is relatively low. Considering τ_{zz}, it amounts to 0.3% and 0.4% for surface tension and conductivity, respectively. These errors on the stress in both cases continue to increase after the end of the domain (for $z = 0.08$ m), although they tend to zero for the two other variables. In comparison with the uncertainties due to the measurements, the error made by considering a constant value for the surface tension and the conductivity over the range of temperature is lower, especially for the axial stress.

The impact of neglecting the dependence of density on temperature is investigated by considering the density value at 800°C (2500 kg/m^3) and at 1300°C (2470 kg/m^3). The error between these two cases is less than 1 % for the temperature, and a maximum of about 1.2% and 1.7% for the velocity and the axial stress, respectively. On the other hand, the variation of the final axial stress $\tau_{zz,\mathrm{f}}$ is approximately 0.6%.

In conclusion, the error introduced by neglecting the temperature dependence of material properties (except for the viscosity) is in general smaller than the uncertainties due to measurement errors. As a consequence, the conductivity, surface tension and density can be approximated as constant over the range of temperature considered here. Note however that this conclusion is not valid around the glass transition, where the variation of the properties with temperature are much larger, or in unsteady conditions where surface tension can play an important role (e.g., Marangoni effect).

5.1.4 Viscosity equation

The viscosity and its temperature dependence play a key role since they directly link the cooling of the fiber to the stress. As described in Section 2.2, the physical model is based on the VFT viscosity law, which is commonly used in numerical simulations of glass forming. Mauro [44] have proposed the MYEGA law for the viscosity of a liquid glass (see Section 2.4.1, Eq. (2.43)), rewritten here for convenience:

$$\log_{10}\eta = \log_{10}\eta_\infty + \frac{K}{T}\exp\left(\frac{C}{T}\right) .$$

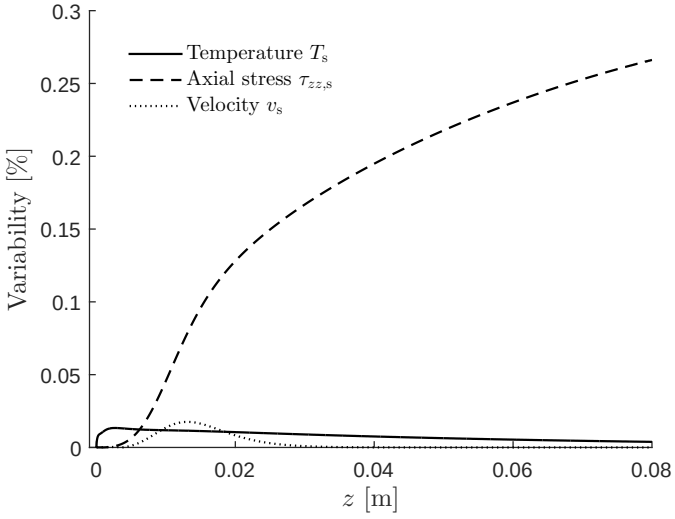

(a)

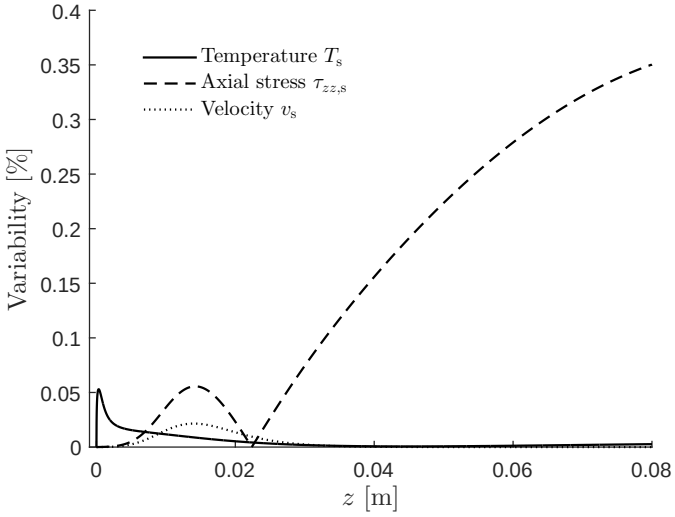

(b)

Figure 5.6: Variability of T, v_s and $\tau_{zz,s}$ between constant properties taken at 1300°C and properties that are function of temperature, as given in Table 2.2, for the surface tension (a) and the conductivity (b).

The influence of the viscosity law is analyzed by comparing predictions obtained with the VFT and the MYEGA formulations. The calibration constants in the two models, Eq. (2.9) and Eq. (2.43), have been obtained by fitting experimental data.

Results for the viscosity and axial stress along the fiber are presented in Fig. 5.7. Figure 5.7(a) shows that the largest viscosity variation is about 17%, in the lower temperature range. On the other hand, almost no variation of the axial stress is observed in Fig. 5.7(b). This is fully coherent with the fact that the axial stress is mostly affected by variations in the lower viscosity range, i.e., at high temperature where both models are very similar. It can be concluded that the choice of the viscosity law, i.e., VFT or MYEGA model, is not as important as an accurate calibration of the model constants, especially around the working point.

5.2 One-dimensional model solution

A one-dimensional model has been derived in Section 2.3, based on following approximations: *i)* the radial variation is neglected and, *ii)* only the viscous force is considered. Besides its simplicity, the advantages of using this model are the reduced calculation time and the semi-analytical form of the solution. This section presents the solution of this model in comparison with that of the two-dimensional model and discusses its limitations. First, the contribution of the different physical forces is presented, the impact of the radial variation is then analyzed.

5.2.1 Contribution of the different physical forces

The one-dimensional model assumes only a viscous force. More specifically, the inertial, gravity, surface tension and drag forces are neglected. The impact of neglecting these forces on the axial stress is investigated here. The influence of each individual force can be estimated with the two-dimensional model by turning off all other forces but the viscous force and the specific force to be investigated. A comparison of the results to those found with only the viscous force leads to the contribution of this specific force.

Figure 5.8 shows the contribution of each individual force to the final axial stress compared to the case where only the viscous force is considered, as in the one-dimensional model. In other words, these individual contributions correspond to an estimate of the error committed by neglecting the corresponding force. It can be seen that both the gravity and the drag force have only a small negative contribution. On the other hand, surface tension leads to the largest contribution, which amounts to about 25% of the total stress shown in Fig. 5.4(b). Finally, the inertial force has a non-negligible effect ($< 10\%$)

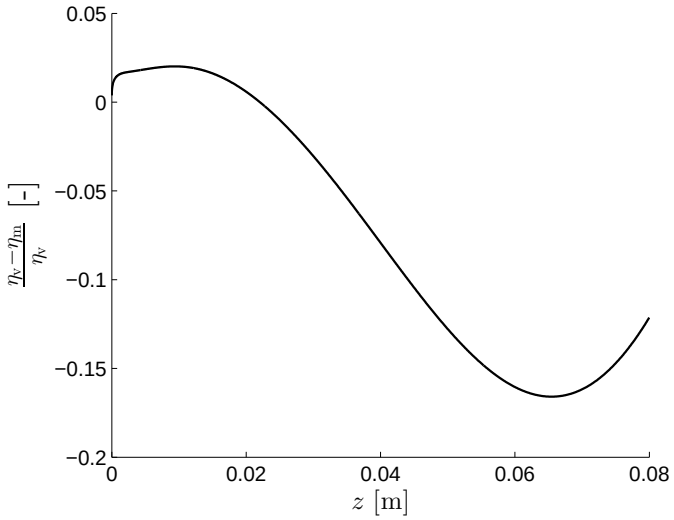

(a)

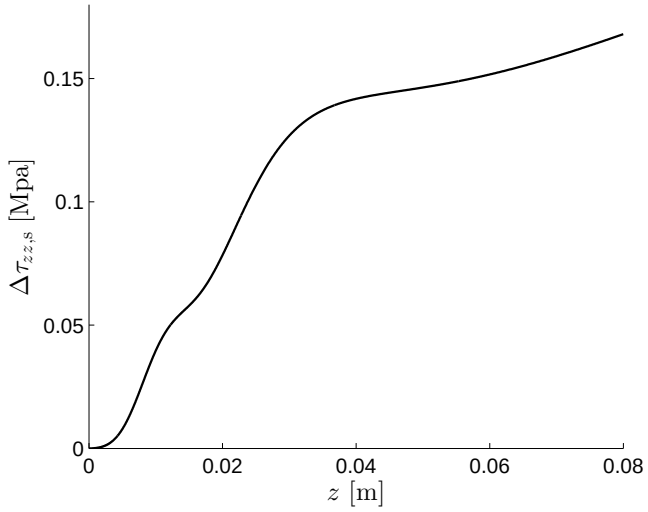

(b)

Figure 5.7: (a) Relative variation of the viscosity between the VFT (η_v) and MYEGA (η_m) models as a function of z. (b) Difference in axial stress obtained with the MYEGA viscosity law compared to a simulation using the VFT law. The reference case is based on case B in Table 5.1 using the two-dimensional model.

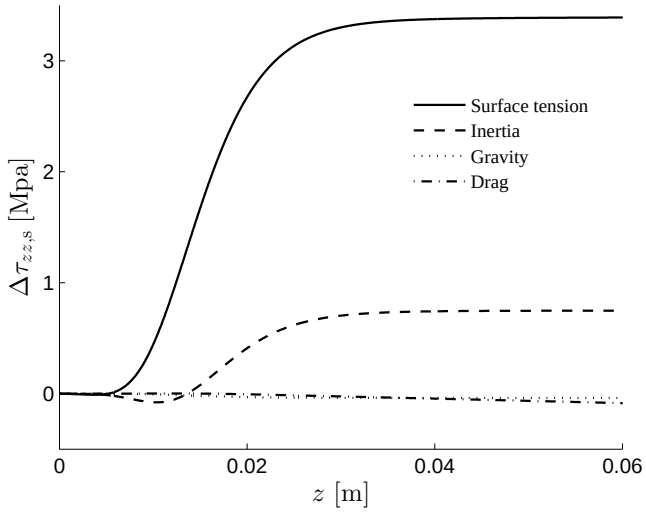

Figure 5.8: Difference in axial stress along the free surface between predictions of the two-dimensional model where only the viscous force is taken into account and the cases where each other individual force is also considered. The solution is based on case B in Table 5.1 using the two-dimensional model.

due to the large velocity gradients along the fiber. It can be shown that the axial velocity is mostly affected by these two forces in the vicinity of the tip exit, which in turn impacts the axial stress along the entire fiber but leaves the temperature field almost unchanged.

These results demonstrate that gravity and air drag can be safely neglected. However, discarding the effects of surface tension and inertia negatively impacts the quantitative prediction of the model.

5.2.2 Radial variations

The radial variations in temperature and axial stress are then analyzed in order to assess the validity of the one-dimensional assumption. To specifically isolate this assumption from the other simplifications on which the model is based, the two-dimensional model is used here with only the viscous force (i.e., neglecting gravity, surface drag, surface tension and inertia) and with constant properties. Results are then compared to the predictions of the one-dimensional model.

The temperature and axial stress profiles are considered both at the symmetry line and at the free surface. Figure 5.9 shows the difference in temperature and axial stress between the centerline and the free surface along the axial direction (continuous line) obtained with the two-dimensional model. The temperature difference reaches a maximum value of 16°C at a distance of 5 mm away from the tip and then decreases to almost zero (see Fig. 5.9(a)). This peak occurs where the radius of the fiber is still relatively large. As the

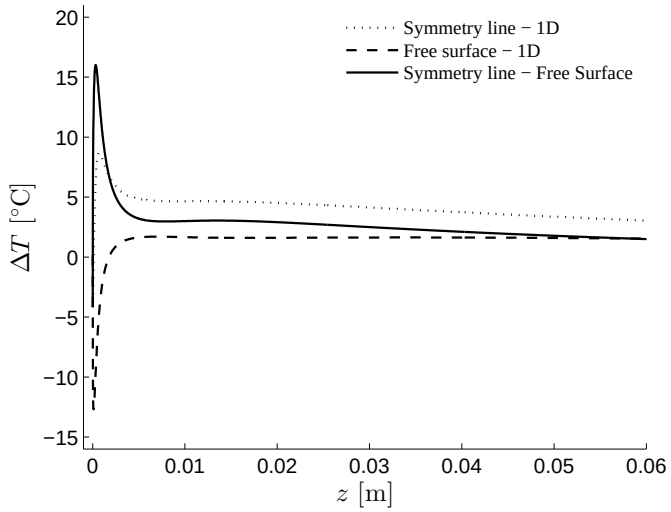

(a)

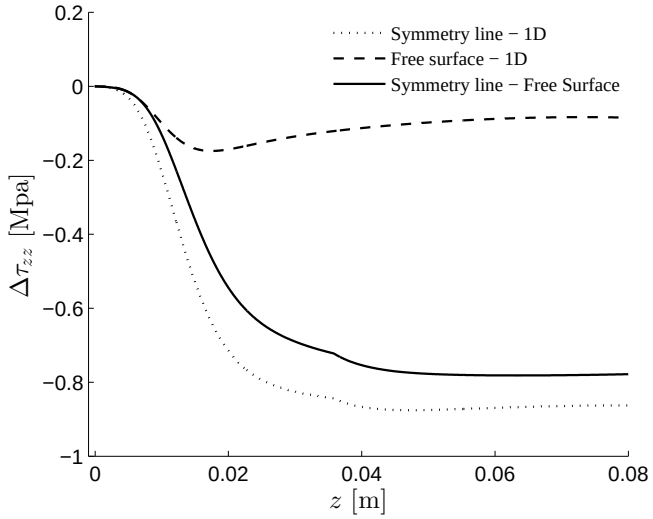

(b)

Figure 5.9: Temperature difference ΔT (a) and axial stress difference $\Delta\tau_{zz}$ (b) between the symmetry line and the free surface as a function of z obtained with the two-dimensional model (continuous line), and between the two-dimensional and the one-dimensional model at the symmetry line (dotted line) and the free surface (dashed line). The solution is based on case B in Table 5.1.

radius decreases, heat diffusion within the fiber is much more effective at homogenizing the temperature, leading to a more oblate radial temperature profile, as illustrated in Fig. 5.10. Note also that the maximum radial temperature variation is small compared to the local temperature, and represents only 3.2% of the 500°C temperature drop along the first 8 cm of the fiber.

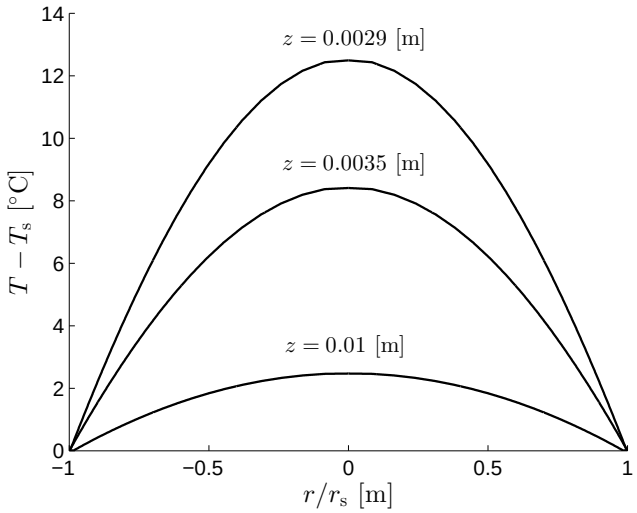

Figure 5.10: Radial distribution of the temperature across the fiber at different axial positions for case B in Table 5.1. T_s and r_s represent the temperature and radius of the free surface, respectively.

Since the viscosity is temperature-dependent (as indicated by Eq. (2.9)), radial temperature variations also induce radial viscosity variations. As a consequence, the axial stress varies also radially, which is illustrated in Fig. 5.9(b). In this case, the difference in axial stress between the centerline and the free surface increases along the fiber until it reaches a constant value at the same location as the axial stress itself reaches its plateau. The radial variation in axial stress remains below 1 MPa, which corresponds to about 6 % of the final axial stress shown in Fig. 5.4(b). Moreover, the maximum axial stress is observed at the free surface and not at the symmetry line.

Figure 5.9 also shows the temperature and stress difference between the two-dimensional and the one-dimensional models at both the symmetry line and free surface. It can be observed that those differences are of the same order of magnitude as the radial variations. Compared to the total temperature drop across the computational domain, the one-dimensional approximation leads to a maximum temperature variation of 2.4% in the vicinity of the tip and much smaller variations further downstream (less than 1%). The stress difference is slightly higher, but still of the same order as its radial variations. Moreover, the difference between the two models is smallest at the free surface, where the stress is maximum, and amounts to about 0.08 MPa (0.8%). As the axial stress plays an

important role in fiber breaking, its maximum value is of key importance. The maximum stress can thus be relatively well predicted by the one-dimensional model.

5.2.3 Conclusion

These results demonstrate that neglecting radial variations is adequate. The main variations in the fiber occur in the axial direction and the problem is almost one-dimensional. However, the other assumptions on which the model is based lead to larger deviations. In particular, neglecting all forces (inertia, gravity, drag and surface tension) but the viscous one results in an underestimation of the axial stress, as discussed in the previous section. This precludes the one-dimensional model from providing accurate quantitative results. Nonetheless, the qualitative behavior is well captured. Moreover, its quasi-analytical solution clearly identifies the dependency between all the parameters. Finally, its numerical resolution is much faster, which is advantageous when a large number of simulations is required.

5.3 Solution of the surrounding air flow model

The solution calculated in the previous sections involved an empirical correlation for the convective heat transfer coefficient. As mentioned previously, the accuracy of this correlation is questionable. In order to investigate the cooling by convection, the surrounding air flow around the fiber is solved numerically. The convective heat flux is then extracted and compared to predictions given by the empirical correlation. More specifically, the surrounding air model developed in Section 2.5 is solved with the numerical approach described in Section 4.3. This requires the manual coupling of both solvers Polyflow and Fluent, which partially limits the investigation of this topic. First, the general solution of the air flow and heat transfer is presented in Section 5.3.1. Then the comparison with the correlation is discussed in Section 5.3.2. Finally, a brief comparison with other correlations found in the literature is provided in Section 5.3.3.

5.3.1 General solution

The general solution of the surrounding air model coupled to the fiber model is first analyzed. The case study chosen is case B in Table 5.1 for the fiber, while the surrounding air temperatures T_{in} (see Fig. 2.17) is set to 20°C to represent a single tip bushing. In addition, the air heating by convection at the bushing plate, assumed to be at the tip temperature T_0, is taken into account. The temperature and velocity fields across the domain are shown in Fig. 5.11 and Fig. 5.12, respectively.

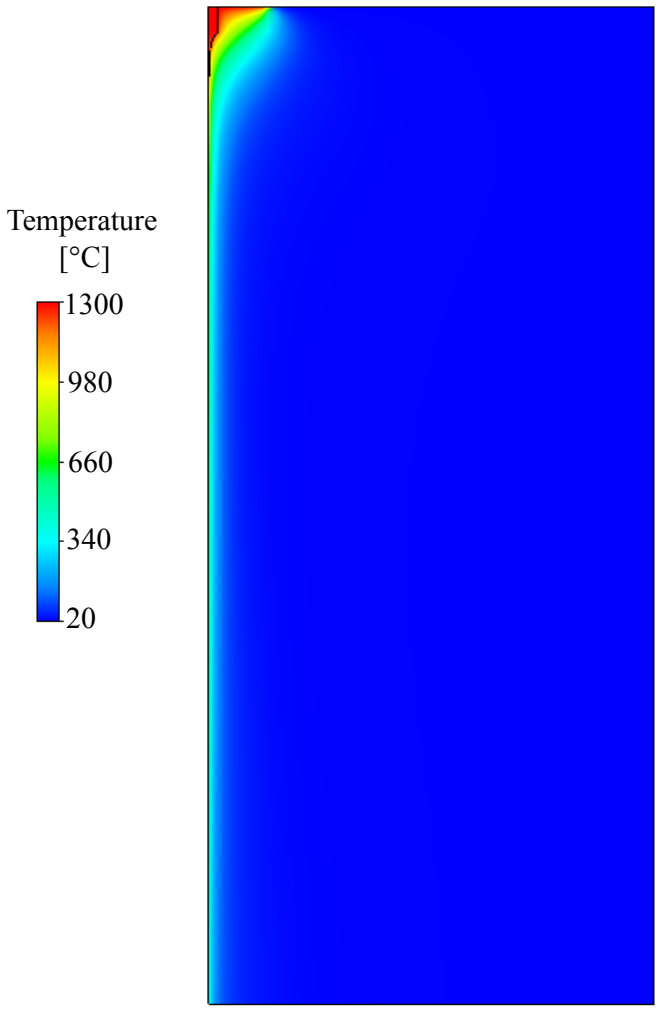

Figure 5.11: Temperature field of both the surrounding air and the fiber.

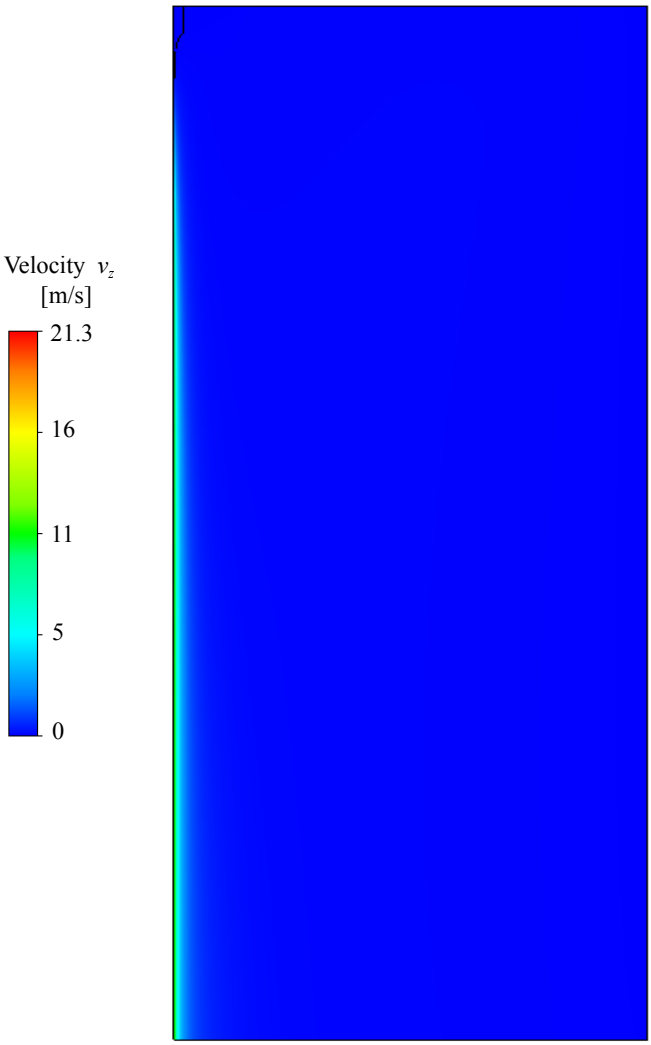

Figure 5.12: Vertical velocity field of both the surrounding air and the fiber.

Because of the no-slip boundary condition at the fiber surface, the air is entrained by the fiber, at the surface of which a boundary layer forms (see Fig. 5.12). The thickness δ_v of this boundary has been calculated and is shown in Fig. 5.13. In this particular case where the surface moves in quiescent air, the thickness δ_v is defined such that $v_z(r - r_\mathrm{s} = \delta_v) = 0.01 v_{z,\mathrm{s}}$, where $v_{z,\mathrm{s}}$ is the free surface axial velocity. As depicted in Fig. 5.13, the thickness increases along z. Note that the final radius of the fiber is reached around $z = 0.04$ m. Very close to the tip, the radius attenuation is large and the bushing plate limits the air displacement in the axial direction, so that the velocity is low compared to its final value. As a result, the boundary layer is extremely thin. The impact of the bushing plate is however limited to the region close to the tip.

Similarly, the temperature difference between the fiber surface and the ambient air, leads to the creation of a thermal boundary layer. The particularity here is that the bushing plate preheats the air surrounding the tip. This impact is very large on the thermal boundary layer thickness δ_T defined as $T_{\delta_T} - T_\mathrm{s} = 0.99(T_{r=\infty} - T_\mathrm{s})$, as shown by the large initial value of δ_T for $z = -0.004$ m to $z = 0.02$ m (see Fig. 5.13).

As there is a difference of 1270°C between the tip and the room temperature, a strong temperature gradient can be observed around the fiber. This gradient decreases along the fiber as the fiber cools down.

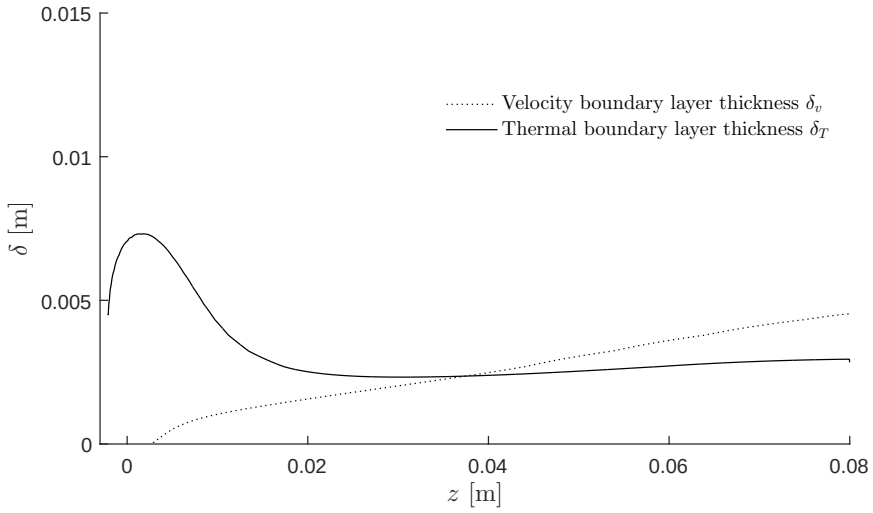

Figure 5.13: Thickness of the velocity and thermal boundary layers along the fiber.

The objective is to analyze the convective heat transfer coefficient,

$$h(z) = \frac{\dot{q}_\mathrm{s} - \dot{q}_{\mathrm{s,rad}}}{T_\mathrm{s} - T_\infty}, \tag{5.1}$$

where $T_\infty = T_\mathrm{in}$. Note that $h(z)$ varies along the fiber. The convective heat transfer

coefficient obtained from the coupled simulation is illustrated in Fig. 5.14. It rapidly increases along the fiber until a plateau is reached. Although the qualitative behavior is the same, a large quantitative discrepancy is observed between the convective heat transfer coefficient obtained from the air flow simulations and that from Kase and Matsuo empirical correlation. This is discussed in more details in the next section.

5.3.2 Comparison with the Kase-Matsuo empirical correlation

Although the Kase and Matsuo empirical correlation [34] is widely used in the literature, it has been developed for conditions that differ from those of the fiber drawing process, as discussed below. The objective here is to compare this correlation with the coefficient h found by numerical simulations of the surrounding air flow. Other empirical correlations are treated in the next section.

The coefficient h given by Eq. (2.23) is calculated using the velocity $v_{z,\mathrm{s}}$ and the radius r_s of the fiber surface. On the other hand, the solution from the coupled fiber - surrounding air flow simulation provides a different value of the convective coefficient. The comparison in Fig. 5.14 shows that the coupled air flow simulation yields a convective heat flux that is half that predicted by the Kase and Matsuo correlation. This reduced cooling leads then to a much higher fiber temperature, as shown by Fig. 5.15.

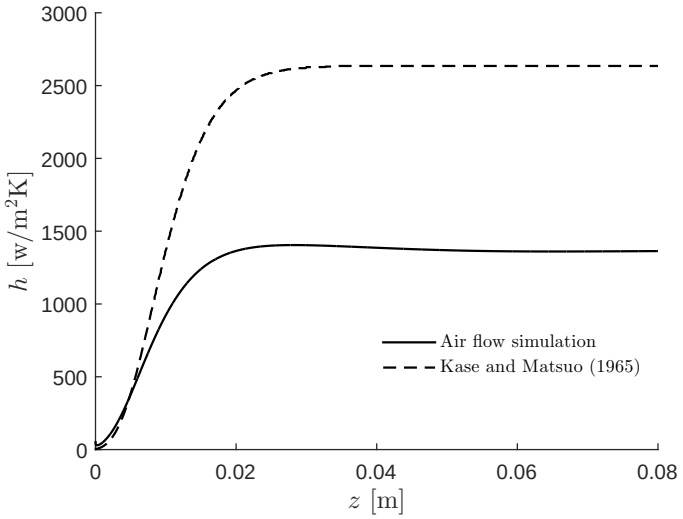

Figure 5.14: Convective heat transfer coefficient $h(z)$ along the fiber from the coupled air-flow simulation and from Kase-Matsuo correlation (Eq. (2.23)).

The Kase-Matsuo correlation was obtained experimentally by recording the cooling of a wire with a constant diameter (0.2 cm) and exposed to an air flow. The cooling behavior of the wire was then expressed as a relationship between the Nusselt and Reynolds numbers. The schematic in Fig. 5.16 illustrates the experiment. Note that the transverse term

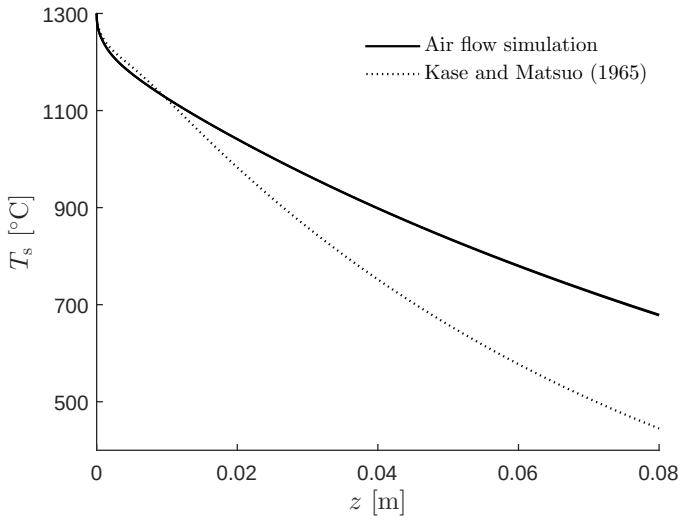

Figure 5.15: Temperature at the free surface as a function of z using Kase-Matsuo and empirical correlation with h calculated by the coupled simulation.

is neglected here as the air velocity is mostly parallel to the fiber. Unfortunately, the

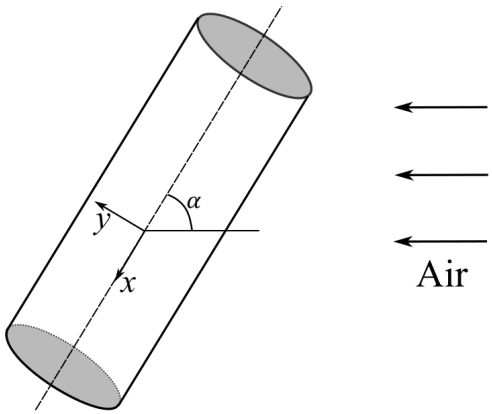

Figure 5.16: Schematic of the experiments of Kase and Matsuo. x and y denote the parallel and transverse directions and α is the angle between the wire axis and the air flow direction.

details of the experimental procedure (such as whether a constant wire temperature or a constant heat flux were imposed, or whether h represents a local or average value) and the methodology to calculate h are not available. Furthermore, the adequacy of this correlation to model the glass fiber drawing process is questionable for several reasons:

- The diameter of the forming fiber continuously decreases over the first centimeters from the tip exit, while the correlation is obtained for a constant diameter of 0.2 cm.

- The fiber entrains the ambient air otherwise at rest, while the correlation is based

on a stationary wire inside a forced air flow.

- The velocity of the forming fiber increases gradually. The air speed in the experiment, which is supposed to represent the fiber velocity, is constant.

- The bushing plate perturbs the flow and preheats the air, while the wire is located in an undisturbed environment at constant ambient temperature (not known).

All these aspects can potentially explain the large discrepancy observed.

5.3.3 Other convective correlations

Beside Kase-Matsuo correlation, others can be found in the literature (see for instance the review of Beyreuther [32]). These correlations have all the form given by Eq. (2.20) and are represented in Fig. 5.17 as a function of the Reynolds number $\mathrm{Re}_{\parallel}$ typically involved in the drawing process. The predicted convective heat transfer coefficient for these different correlations is shown in Fig. 5.18, without changing the others boundary conditions. The correlation from Andrews leads to the largest cooling which is two times larger than the one of Kase-Matsuo. The correlations from Brunig, Copley and Glicksman yield values of h that are closer to that obtained with the coupled fiber-surrounding air flow simulations, but a discrepancy of about 40% is still observed. Further work is thus required to completely elucidate this discrepancy.

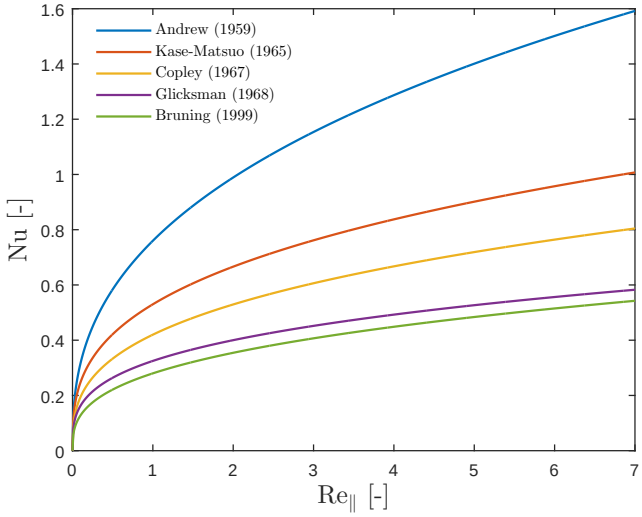

Figure 5.17: Nusselt number as a function of the Reynolds number for several empirical correlations.

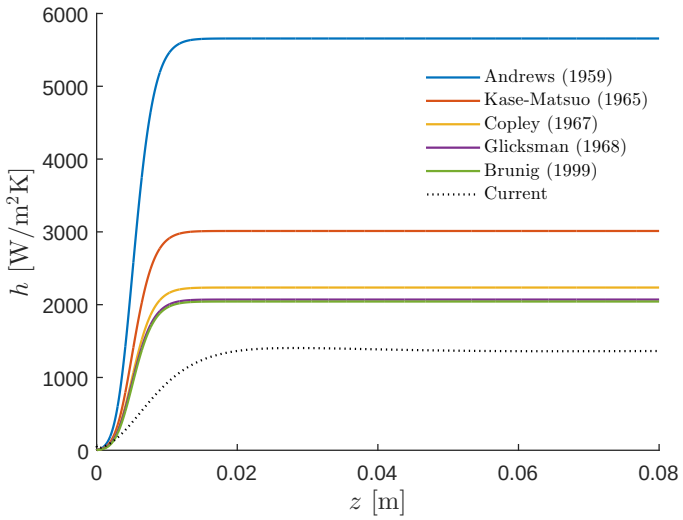

Figure 5.18: Convective heat transfer coefficient h along the fiber for several empirical correlations (case B in Table 5.1).

5.3.4 Conclusion

The surrounding air study demonstrates that the convective coefficient provided by the correlation of Kase and Matsuo is questionable, although it is the most widely used in the literature. The two approaches yield a convective cooling that differ by a factor of two. As the details of the experimental procedure are not available, it is complex to identify the major reason for this discrepancy. A brief comparison with other correlations found in the literature also shows a large difference with respect to the simulations of the surrounding air. Nonetheless, the discrepancy between air flow simulation and Kase-Matsuo is of the same order of magnitude as the discrepancy between some of these other correlations. This indicates that the exact form of the convective coefficient remains an open question and requires a more detailed analysis. Note also that the convective heat transfer coefficient can greatly vary in the case of multi-filament bushing, where the transverse velocity plays a more important role. The precise simulation of the surrounding air flow appears in these conditions as the best adapted approach.

5.4 Solution of the semi-transparent radiation model

Section 5.1-5.2 focused on the solution of the physical models in which internal radiation is neglected. The glass was assumed to be opaque and grey. As a consequence, only the conduction heat flux took part in the energy transfer within the material, while a grey radiative flux was imposed at the surface as a boundary condition. This assumption has been systematically used in the literature and leads to a major simplification

for the resolution of the model. Nonetheless, the energy balance within a glass melt can be significantly impacted by radiative transfer. In particular, it is well known that the radiative flux must be considered in the case of a furnace or in other glass forming processes. Because this effect has never been assessed in the case of the fiber drawing process, the present section focuses on quantifying the contribution of internal radiation on the temperature and stress fields.

The first section deals with the general solution of the grey semi-transparent model where a comparison with the solutions from the previous sections (opaque model) is presented. The semi-transparent band model is then studied in Section 5.4.2. Subsequently, Section 5.4.3 discusses the influence of the radiative properties on the solution. The influence of the effective emissivity depending on the fiber radius and temperature in the case of an opaque grey fiber is analyzed in Section 5.4.4. Finally, conclusions and a discussion on the model limitations are given in Section 5.4.5.

5.4.1 General solution of the grey internal radiation model

The internal radiative flux may be sufficiently high to modify the conservation of energy (Eq. (2.3)) and thereby impact the temperature field. This can in turn lead to a variation of the final value of the axial stress. Neglecting this flux can lead to an error, which is analyzed here. The discussion is based on the comparison between the two-dimensional opaque and semi-transparent models. In the first case, only conduction is considered within the fiber and the radiative flux is imposed through Eq. (2.25). The results of this case have been largely studied in Section 5.1.2. On the other hand, the second model considers a semi-transparent radiative flux in the energy equation including the associated boundary conditions (Eq. (2.74)), as developed in Section 2.6.

This second model has been simulated using the numerical approach presented in Section 4.4. Unless otherwise specified, the results are generated with Polyflow and only a grey body, i.e., independent of the wavelength, is considered in the radiative transfer equations (RTE). Since this is a strong approximation, the effect of a non-grey body is studied in Section 5.4.2. The process parameters are the same as previously (case B in Table 5.1). Table 2.3 provides the radiative properties. The general solution is first analyzed in terms of temperature and then stress.

Temperature analysis

The solution of the radiative model is compared to the solution where the fiber forming is considered as an opaque medium. The temperature profile at the free surface for both solutions is shown in Fig. 5.19.

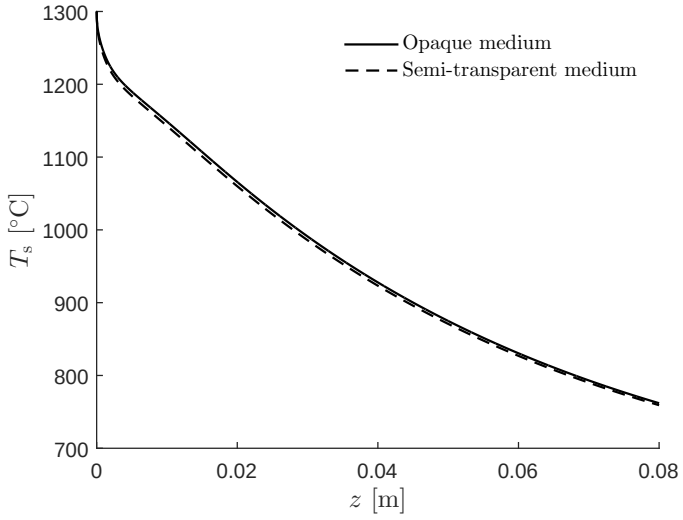

Figure 5.19: Temperature at the free surface as a function of the axial coordinate z obtained with the two-dimensional grey opaque and semi-transparent models for case B in Table 5.1.

As a first observation, considering the fiber as semi-transparent increases slightly the cooling of the fiber at high temperature. The temperature difference between the opaque and the semi-transparent cases is shown in Fig. 5.20(a). The difference increases rapidly in the first millimeters until a maximal variation of about 6°C at $z \approx 2$ cm is reached. It is not surprising that the impact of the internal radiation is the largest at higher temperature in the region near the tip, since the radiative heat transfer dominates the cooling there (see Fig. 5.3). After this maximal variation, the difference between both cases decreases slowly until the overall effect of internal radiation becomes negligible. At these lower temperatures, convective heat transfer dominates the cooling.

The impact of the radiative flux can be also analyzed in the radial direction. Figure 5.20(b) provides the difference between the axial temperature profile at the free surface and at the axis of symmetry. Considering the fiber as a semi-transparent medium leads to a similar radial profile to those for the opaque case. The maximal variation between the center and the surface of the fiber reaches 18.8°C in the opaque case and 19.3°C in the semi-transparent case. This maximum difference occurs in a very narrow peak, the radial non-homogeneity being much lower afterwards. Once again, the impact of the internal radiation is shown to be the largest at higher temperature.

Two effects could be a priori expected from considering internal radiation: the radial temperature distribution should be modified, and the cooling heat flux should increase. Figure 5.20(b) shows that the first effect is negligible, while Fig. 5.20(a) indicates that internal radiation leads to a slightly larger cooling rate, as heat from inside the fiber can escape through radiation.

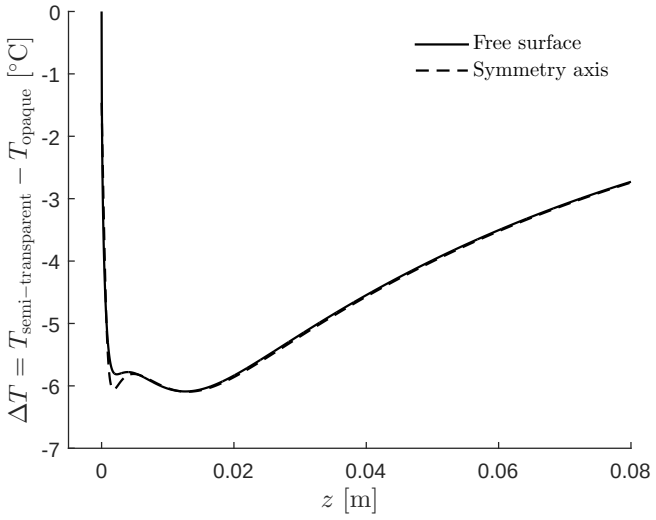

(a)

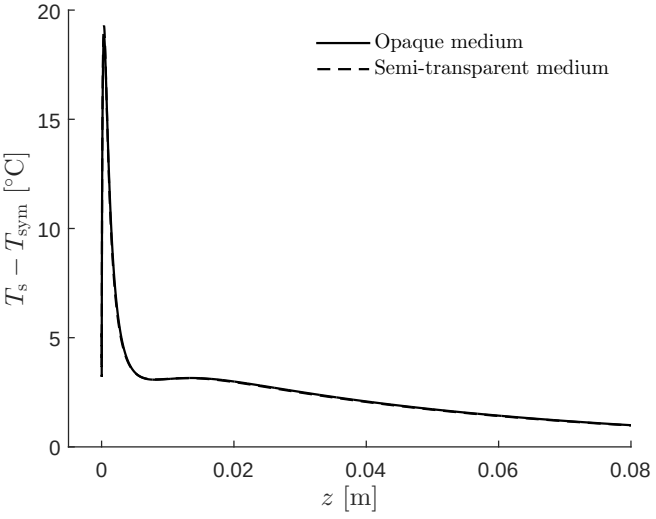

(b)

Figure 5.20: Temperature difference at the free surface and symmetry axis between the two-dimensional semi-transparent and grey opaque case (a), and between the free surface and the axis of symmetry for the two models (b).

Stress analysis

Figure 5.21 shows the axial stress at the free surface for the two models. The semi-transparent model leads to the same qualitative behavior but some quantitative differences can be observed. In particular, the final value of the axial stress $\tau_{zz,\text{f}}$ is larger by about 1.6 MPa (i.e. $\approx 8\%$). This stress increase is directly linked to the larger cooling rate. From Eq. (2.33), the stress is proportional to the inverse of the fluidity. If the cooling rate increases, then the stress also increases. Furthermore, this quantity is more sensitive to

variability at lower viscosity, and thus at higher temperature where radiation dominates.

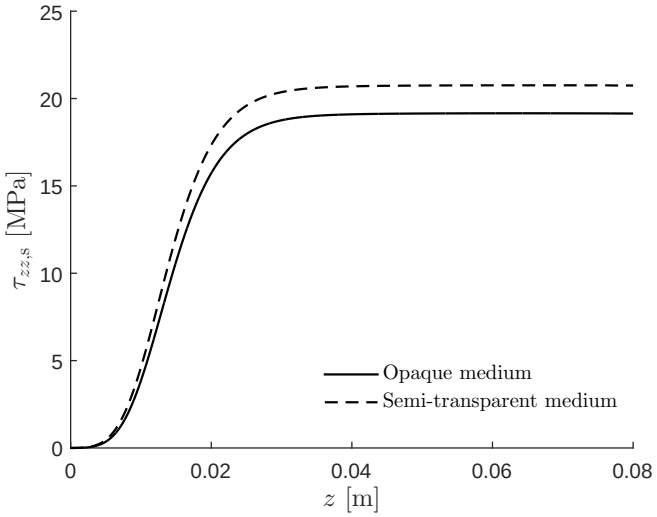

Figure 5.21: Axial stress τ_{zz} at the free surface as a function of the axial coordinate z for the two-dimensional semi-transparent and opaque models.

5.4.2 Impact of a non-grey model

The results in the previous section were calculated using a grey model, i.e. independent of the wavelength, for the radiative transfer equation supplemented with a radiative flux at the free surface representing the opaque contribution of the spectrum[1]. Nevertheless, a grey model can be a strong approximation if one considers the form of the absorption coefficient in the semi-transparent window shown in Fig. 2.18. Furthermore, the model calculates an intensity which is constant for all wavelengths. The impact of a non-grey model compared to a grey model is studied here including the effect of the opaque band. Since Polyflow cannot deal with a non-grey body, Fluent is used to simulate the fiber. Unfortunately, as mentioned in details in Section 4.4, only a one-way coupling from Polyflow to Fluent can be performed. As a consequence, the radiative problem is solved for a fixed geometry of the fiber. Following results are thus more qualitative than quantitative, but they still provide an estimate of the effects of a grey assumption. The process conditions are the same as previously. Additionally, the opaque part of the spectrum is investigated here in more detail. In particular, the influence of this region and the value of the cutting wavelength on the cooling is analyzed.

[1]The denomination opaque can be confusing here: the grey opaque model is the model without internal radiation, while the opaque band denotes the range of wavelengths where the optical thickness $\tau_\lambda \to \infty$.

Influence of the semi-transparent region

First, the impact of a non-grey body is studied only in the semi-transparent region where the opaque band is removed to clearly isolate the effect of the non-grey body. Two different cases are considered:

- The first one solves the RTE only for one band in which $\kappa = 207$ [m^{-1}]. This band is taken from 0.7 to 3.8 μm. The remaining part of the spectrum does not contribute to the radiative transfer.
- The second model solves the RTE using a four-band model within the same range of wavelengths. The bands are given in Table 2.3.

The results are shown in Fig. 5.22 where the absolute free-surface temperature difference between the two cases is represented. The maximal variation is only about 2°C, and occurs again at high temperature. Then, the variation decreases to ~ 1.5°C. This seems to indicate that the spectral variation of the absorption coefficient in the semi-transparent region has a very limited impact on the solution.

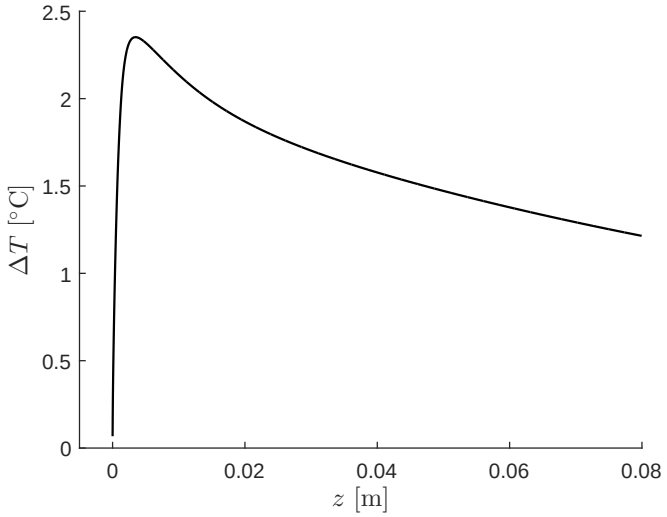

Figure 5.22: Difference of temperature along the free surface for the two-dimensional semi-transparent model between the case where only one band is considered ($\kappa = 207$ m^{-1}) and the case with four bands (given in Table 2.3).

Influence of the opaque region

The opaque part of the spectrum, which corresponds to wavelengths larger than 3.8 μm, is represented by condition (2.74) where the opaque radiative flux is

$$\dot{\mathbf{q}}_{\mathrm{s,op}} = \epsilon_{\mathrm{op}} \left[f_{\mathrm{g}} I_{\mathrm{b}}(T_{\mathrm{s}}) - f_{\mathrm{env}} I_{\mathrm{b}}(T_{\mathrm{env}}) \right],$$

and the ratio f_g and f_{env} are given by

$$f_i = \frac{\int_{\lambda_c}^{\infty} I_{b,\lambda}(T_i)\mathrm{d}\lambda}{\int_0^{\infty} I_{b,\lambda}(T_i)\mathrm{d}\lambda}.$$

Although the emission of a black body at large wavelength is lower than in the semi-transparent range, it can impact the cooling of the fiber. In order to highlight the contribution of this opaque flux, a case study where the opaque radiative flux $\dot{\mathbf{q}}_{s,op}$ is set to zero has been simulated. The result is shown in Fig. 5.23(a). The impact of the opaque flux is very large with a maximal difference of 100°C after 0.02 m. Then, the difference decreases to 60°C at $z = 0.08$ m. For the axial stress, shown in Fig. 5.23(b), the variation is also very important with a difference of 10 MPa for its final value. The main conclusion is that the opaque region represents a major contribution to the cooling of the fiber and cannot be neglected.

On the other hand, $\dot{\mathbf{q}}_{s,op}$ depends on the value of f_g. This parameter is a function of the temperature and the cutting wavelength λ_c. In the reference solution $f_g = 0.47$, which is an average between 1300 and 1000°C, and $\lambda_c = 3.8$ μm. The sensitivity of the solution to f_g is investigated here considering two extreme cases, $f_g = 0.37$ and $f_g = 0.72$. This range corresponds to the variation of temperature between 800°C to 1300°C. The results for the temperature and the stress are presented in Fig. 5.23(a) and Fig. 5.23(b) as the two dotted lines for $f_g = 0.37$ (1300°C) and 0.72 (800°C). Note that the case $\dot{\mathbf{q}}_{s,op} = 0$ corresponds to $f_g = 0$. The axial profile of the temperature shows a variation with the value of f_g. An increase of this value yields a higher cooling of the fiber because of the increased opaque radiative flux. The final axial stress value is largely impacted with an increase of about 8 MPa between the case 1300°C and 800°C. The cooling is thus sensitive to f_g. Nevertheless, the opaque flux $\dot{\mathbf{q}}_{s,op}$ dominates the convective heat transfer for temperatures higher than 1200°C, as shown in Fig. 5.24. Consequently, f_g has been calibrated at a higher temperature, i.e., the average between 1000 and 1300°C.

On the other hand, f_g is also dependent on the cutting wavelength λ_c. This wavelength represents the transition between the semi-transparent and the opaque region where $\kappa \to \infty$. As discussed in Section 2.6, there is no specific physical criterion for defining the value of λ_c and it has thus been chosen arbitrarily to be 3.8 μm. The sensitivity of the solution to the choice of this cutting wavelength is presented in Fig. 5.25. The range of uncertainties on this value is between taken 3.8 μm (i.e. reference case) and 4 μm. Above 4 μm, the measurement of the opaque emissivity can be taken into account. The results are again based on the axial stress and show a variation of 0.75 MPa for the final value $\tau_{zz,s}$. A decrease of the value of λ_c increases the range of wavelengths taken into account in f_g from Eq. (2.75) and leads to a higher opaque flux, a larger cooling, and thus a larger

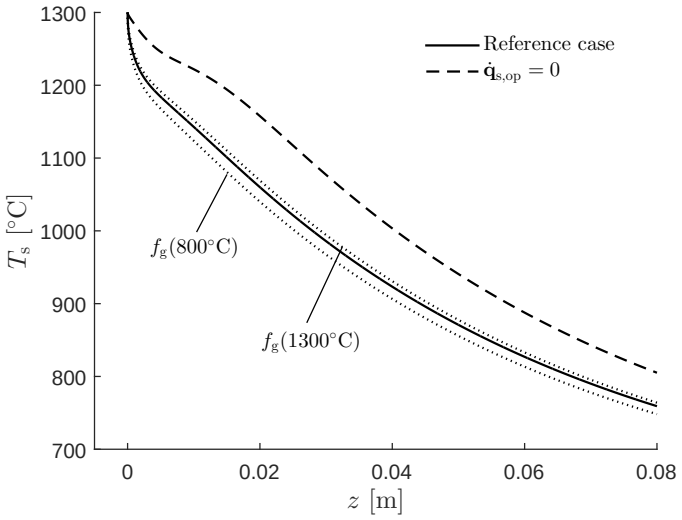

(a)

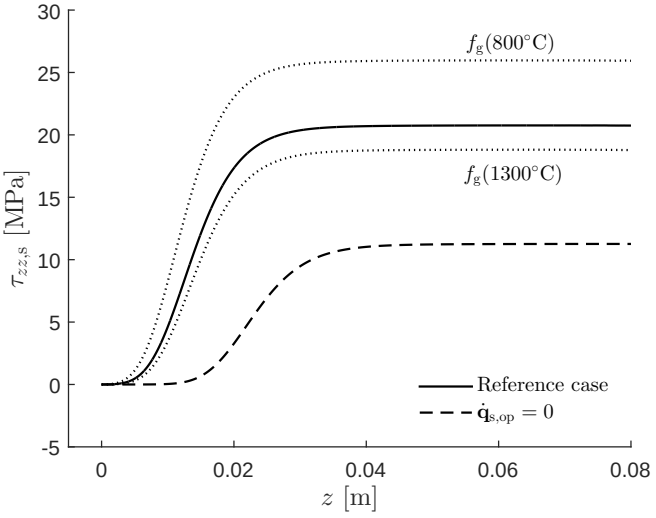

(b)

Figure 5.23: Solution of the two-dimensional semi-transparent model for temperature (a) and axial stress (b) as a function of z considering different values of the opaque band parameters. The reference denotes the semi-transparent case studied in Section 5.4.1 based on the parameters from Table 2.3.

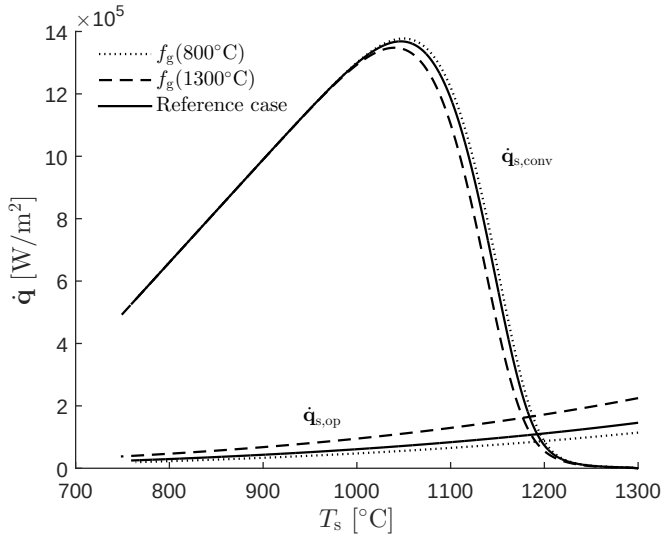

Figure 5.24: Radiative and convective flux as a function of the temperature of the fiber surface T_s for different values of f_g in the two-dimensional semi-transparent model.

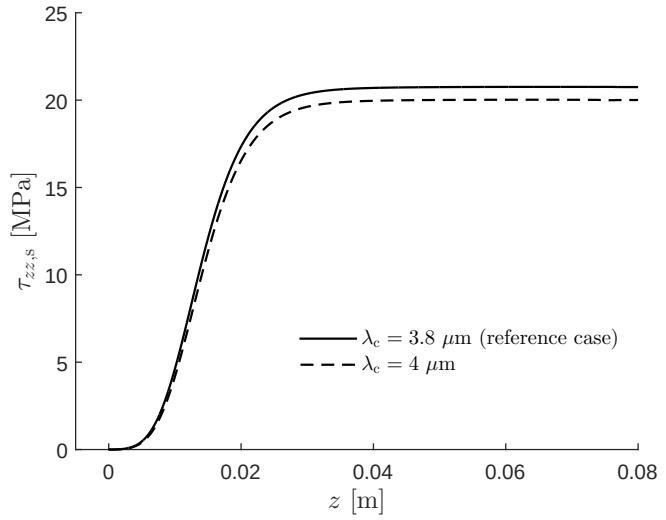

Figure 5.25: Axial stress as a function of z for two different cutting wavelengths.

$\tau_{zz,s}$. However, since the impact is small ($\approx 3\%$), the value of 3.8 μm is kept.

5.4.3 Sensitivity of the radiation model to radiative properties

The radiative model involves two fundamental radiative properties: the absorption coefficient κ_λ and the refractive index of the glass n_g. The first one represents how the radiation is transferred within the medium, while the second is related to the transmission of the radiation intensity through the fiber surface. This section investigates the sensitivity of the grey semi-transparent radiative model to these two properties.

Effect of the absorption coefficient

The variation of the absorption coefficient originates in variations of the level of FeO or OH content in the glass. Since this variability can be critical in the furnace, this section focuses on its impact on the fiber drawing process and the resulting stress. The absorption coefficient varies from $\kappa = 64$ m^{-1} to $\kappa = 866$ m^{-1} within the semi-transparent range, as depicted in Fig. 2.18. The sensitivity analysis is based on the two-dimensional semi-transparent model with the grey assumption. Three values of κ are considered: $\kappa = 866$ m^{-1}, $\kappa = 207$ m^{-1} and $\kappa = 64$ m^{-1}, corresponding to the maximum, mean and minimum values of the absorption coefficient in the semi-transparent range. Figure 5.26 shows the temperature and axial stress difference at the free surface between two solutions using a different value of κ. As expected, the maximum variation is found between the minimum and maximum values of κ. These differences remain rather small so that a mean value of $\kappa = 207$ m^{-1} can be used. When the absorption coefficient increases, the gradient of the radiative flux within the medium is smaller and its contribution to the energy equation becomes lower. The transport of energy is thus lower within the fiber.

Effect of the refractive index

The refractive index of the glass n_g is a property involved in the transmission of the intensity between the glass and the air, as defined in Section 2.6.4 for the semi-transparent boundary conditions. In particular, an increase of n_g leads to a decrease of the quantity of energy transmitted through the fiber surface. This quantity depends on the glass composition. The range of variation is taken from 1.42 (pure silica glass [50]) to 1.56 (Advantex© glass). A similar analysis to that described in the above section is performed. The impact on the temperature profile at the free surface due to the variation of n_g is less than 0.1°C, as shown in Fig. 5.27(a). As expected, the cooling is higher in the case of $n_g = 1.42$ leading to a lower temperature than for the case with $n_g = 1.56$. The impact on the axial stress is also very small with a difference of 0.025 MPa (i.e. $\approx 1\%$).

5.4.4 Comparison with the effective emissivity

The previous sections have highlighted the limited impact of using a radiative transfer model within the glass in the context of the fiber drawing process. As the modification of the radial profile of temperature is negligible when internal radiation is considered, the main impact is observed in the radiative cooling flux. This flux consists of the radiative flux from the glass bulk and the flux from the opaque part of the spectrum at the surface. As a result, the stress is more affected by the cooling of the fiber than the variation of

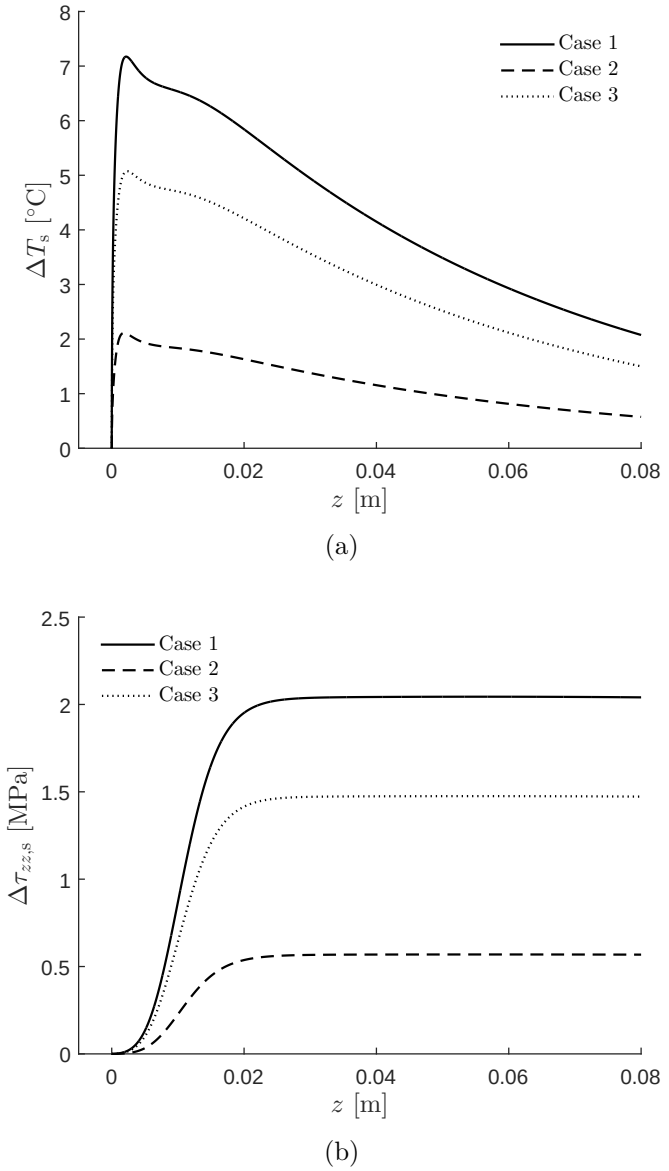

Figure 5.26: Difference in the (a) temperature and (b) the axial stress at the free surface between the reference solution $\kappa = 207$ m^{-1} and the solution with $\kappa = 866$ m^{-1} (case 1), $\kappa = 270$ m^{-1} (case 2), and $\kappa = 64$ m^{-1} (case 3), using the two-dimensional semi-transparent model with the grey assumption.

the radial temperature profile due to the internal radiation. In other words, the radiative heat loss is the most relevant aspect.

The opaque model assumes a constant emissivity that cannot take into account the variability of the flux from the bulk. In Section 2.4.6, an effective emissivity was measured experimentally (Eq. (2.53)), whose value depends on the thickness and the temperature of the surface. This measured effective emissivity includes the contribution to radiation not only from the surface, but also from the bulk. The purpose of this section is to

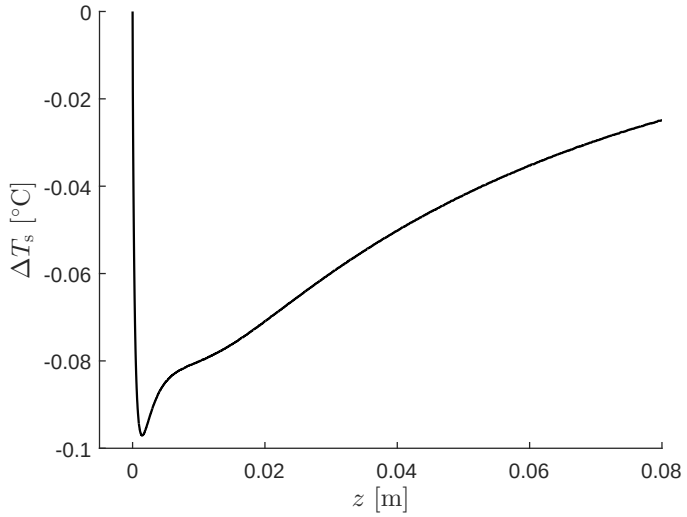

(a)

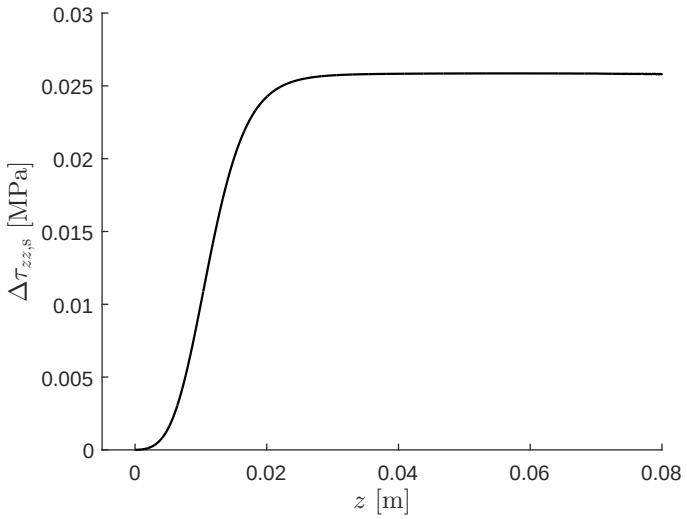

(b)

Figure 5.27: Temperature (a) and axial stress (b) difference at the free surface as a function of z between two solutions computed with $n_g = 1.42$ and $n_g = 1.56$. Results are obtained with the two-dimensional semi-transparent model with the grey assumption.

analyze the adequacy of using an effective emissivity in an opaque grey model compared to a full internal radiative model. The use of an effective emissivity without significant deterioration of the solution accuracy would greatly simplify the modeling of radiation and reduce the computational cost.

In order to analyze the possible use of an effective emissivity, three fiber models are considered:

- The two-dimensional model where the medium is considered as a grey opaque

medium without internal radiation. The emissivity of the surface flux is equal to 0.4 as previously. It corresponds to the reference model analyzed in Section 5.1.

- The two-dimensional model where the medium is also considered as a grey opaque medium without internal radiation, but with an effective emissivity that depends on the fiber radius and surface temperature (see Eq. (2.53)).

- The two-dimensional semi-transparent model with the grey assumption, as discussed in Section 5.4.1.

The temperature and axial stress along the fiber obtained with the three models are shown in Fig. 5.28 and the corresponding differences between the effective emissivity and the two other models are illustrated in Fig. 5.29. The comparison between the effective emissivity approach and the internal radiation model, and between an effective emissivity and a constant emissivity approach shows a maximum temperature difference of 11.5°C and 9.5°C, and an average temperature difference of 5.7°C and 8°C, respectively.

On the other hand, the axial stress profiles given in Figs. 5.28(b) and 5.29(b) show that the final axial stress $\tau_{zz,\mathrm{f}}$ at the free surface is almost the same for the internal radiation and for the effective emissivity model. The main difference is observed in the region very close to the tip. Although temperature differences are larger between the effective emissivity approach and the full internal radiation model, the difference in axial stress is lower.

Finally, Fig. 5.30 represents the difference of temperature and axial stress between the free surface and the symmetry axis for the three radiative models. The use of an effective emissivity leads to very similar profiles of temperature and stress compared to the semi-transparent model. Consequently, the use of this approximation seems to be reasonable.

5.4.5 Discussion

Overall, these results demonstrate that accounting for the details of internal radiation does not significantly modify the solution. The quantitative differences observed are small, especially in light of all other approximations and uncertainties. Moreover, the main impact of including internal radiation is seen in the increased radiative heat flux leaving the fiber surface rather than in the modification of heat transfer within the fiber. It can be concluded that the use of an effective emissivity in the context of a grey opaque radiation model provides an accurate and computationally much less costly alternative to modeling the full internal radiation. Finally, it was also shown that the semi-transparent model is only weakly sensitive to the value of the refraction index, but much more to that

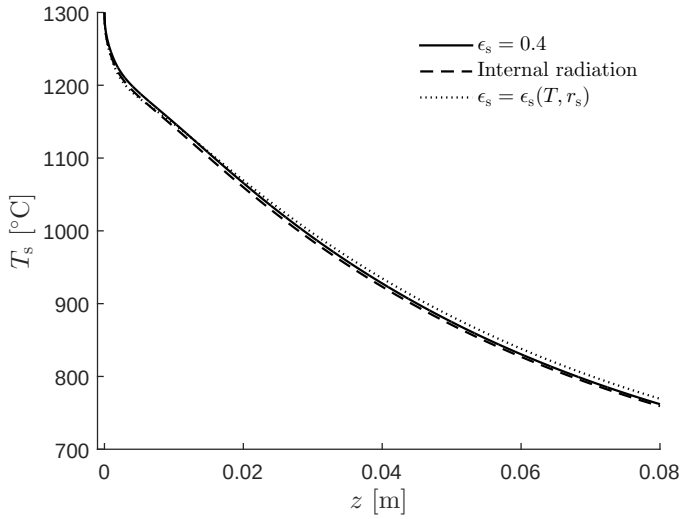

(a)

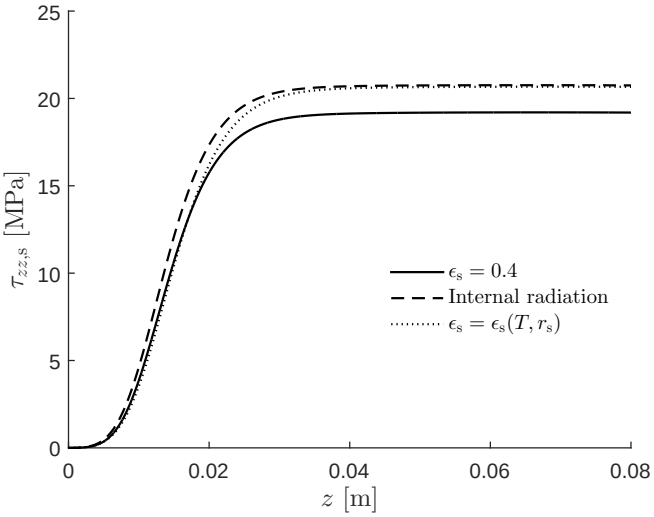

(b)

Figure 5.28: Temperature (a) and axial stress (b) at the free surface as a function of z obtained with three radiative models: *i)* an opaque grey medium with $\epsilon_s = 0.4$, *ii)* an opaque grey medium with ϵ_s that is a function of the fiber surface temperature and radius, and *iii)* a grey semi-transparent medium.

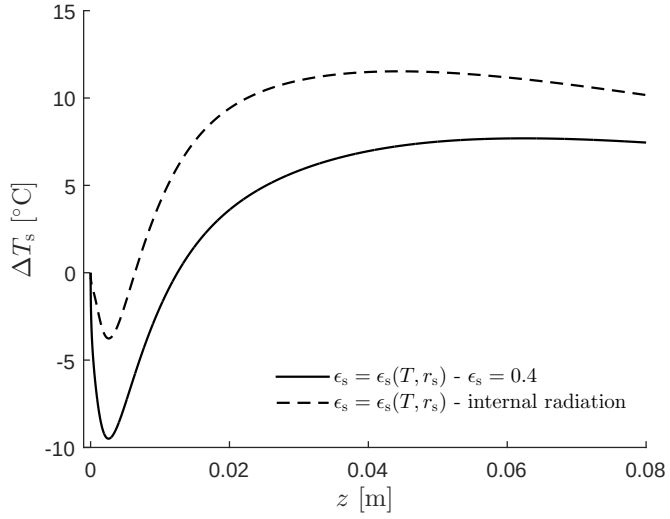

(a)

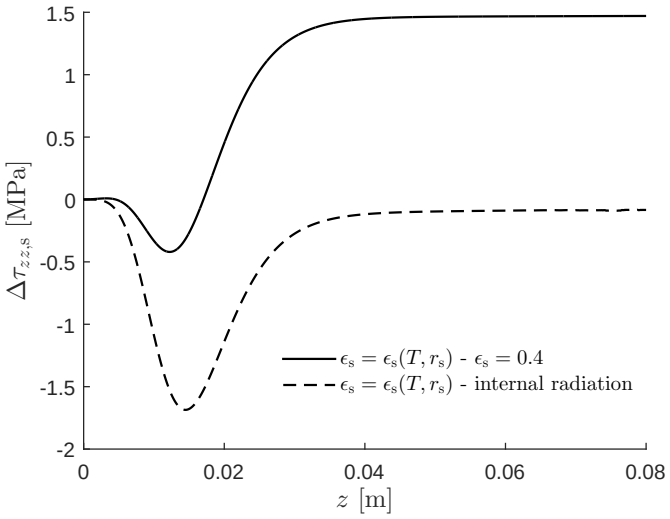

(b)

Figure 5.29: Temperature (a) and axial stress (b) difference at the free surface as a function of z obtained between an effective emissivity and constant emissivity approach, and between an effective emissivity approach and a full semi-transparent model.

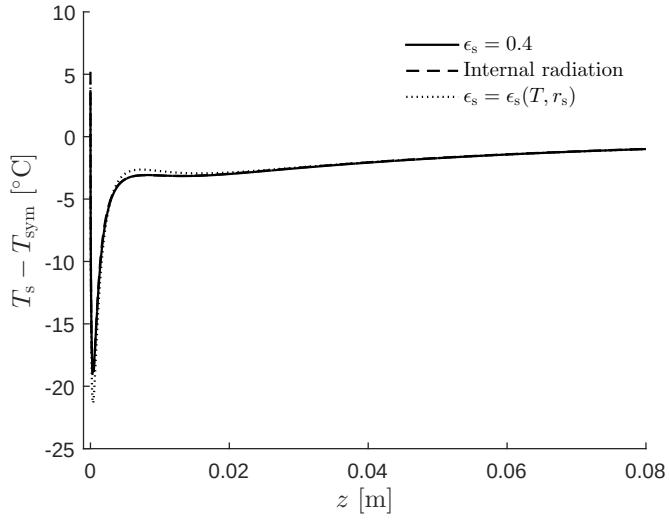

(a)

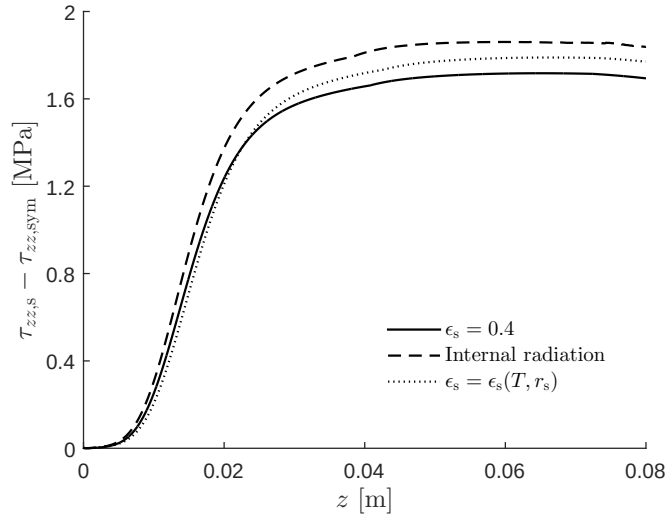

(b)

Figure 5.30: Temperature (a) and axial stress (b) difference between the free surface and the symmetry axis as a function of z for the same three radiative model as in Fig. 5.29.

of the absorption coefficient. In particular, an increase of the absorption coefficient leads to a larger final axial stress.

It should be recalled that the present analysis did not take into account the radiative heat transfer between the bushing plate and the fiber, which could have an important impact on the cooling and thus partly modify these conclusions.

5.5 Summary

This chapter has provided a detailed investigation of the physics involved in the fiber drawing process. In particular, it has presented an analysis of the opaque two-dimensional model and its related one-dimensional approximation. The convective heat transfer coefficient has been studied in more details using a surrounding airflow model coupled with the fiber. Finally, the convective heat transfer coefficient has been studied in more details using a surrounding airflow model coupled with the fiber. In this context, some results were compared with experimental data and the impact of numerous approximations and simplifications has been analyzed with a focus on velocity, temperature, cooling and stress. The main key findings are:

- The radius attenuation is well predicted by the opaque two-dimensional model.
- The maximum uncertainties due to material property measurements amount to about 3%.
- The error introduced by neglecting the temperature dependence of material properties (except for the viscosity) is in general smaller than the uncertainties due to measurement errors. Conductivity, surface tension and density can thus be approximated as constant over the range of temperature considered.
- The use of the more physical MYEGA viscosity law does not improve the results obtained with the empirical Fulcher relation.
- Cooling is critical and strongly impacts the value of the final stress because of the large changes in viscosity with temperature.
- Cooling is dominated by radiation in the vicinity of the tip and by convection further downstream.
- Radial variations are small compared to axial gradients so that the problem is mostly one-dimensional.

- Viscous effects, and to some extent surface tension, are much more important than inertia and gravity.
- Therefore, the one-dimensional model, which only accounts for the viscous force, represents a good approximation of the more complex two-dimensional problem. Moreover, the effect of surface tension on the stress can potentially be added a posteriori.
- The use of an effective emissivity within a grey opaque radiation model provides a good approximation and is computationally much cheaper compared to a complex model that includes internal radiation.
- The empirical correlation of Kase-Matsuo for the convective heat transfer coefficient does not seem to be adequate. A better correlation or a more complex model that includes the flow of the ambient air is required.

It is important to keep in mind that these conclusions are valid within the context of this study. In particular, only the upper part, before glass transition, of a single fiber has been considered. Moreover, the radiative heat transfer between the fiber and the bushing plate and fin shields has been ignored.

While some of these findings have already been discussed in the literature, the present work represents a much more rigorous analysis of the model predictions on numerous parameters. The other important contributions include the development of a semi-analytical one-dimensional model, the extension of the two-dimensional model for internal radiation, and an in-depth assessment of the empirical correlation for convective cooling.

Chapter 6

[CONFIDENTIAL] Application of the single fiber model

The previous chapter focused on assessing the different numerical models and on better understanding the physical phenomena at play in the drawing process of a single fiber. The next step towards characterizing the fiber break is to leverage these physical models in order to identify the key process parameters and the optimal operating window. In particular, the physical models are applied to specific problems related to the industrial production of fibers. The aim of the overall chapter is to define the range of control parameters that lead to an efficient process. More specifically, the operating window is first analyzed, whose objective is to assess the influence of the process parameters on the stress and identify strategies that can be followed to improve the fiber drawing. The stress is again chosen as a key indicator since it is a measure of the robustness of the process. Then, the semi-analytical one-dimensional model is used to quantify the variability of the axial stress across multiple fibers that is caused by temperature inhomogeneities of the bushing plate. Finally, the last part of this chapter is dedicated to the draw resonance, which is an instability that can occur in the process. This instability represents a major limitation to the process efficiency because it constrains the operating window, particularly in terms of temperature. The key results of this chapter can be found in Chapter 8 in Section 8.1.2.

Chapter 7

[CONFIDENTIAL] Break rate prediction

During the drawing, a disturbance or an impurity in the melt can cause a single fiber to break, which generally leads to the failure of all fibers of the bushing position. The objective of this chapter is to develop a preliminary model to predict the failure rate. In the previous chapters, the axial stress was considered as the key performance indicator. Although observations in the production give support to this choice, the stress provides only a partial measure of the process robustness. The aim of this chapter is thus to link this stress to the break rate. More specifically, the proposed break model relates this stress to the probability distribution of the fiber strength. Because the stress is obtained from the physical model derived previously, it would be thereby possible to directly predict the break rate as a function of the process conditions and parameters. Nonetheless, the strength distribution cannot be determined theoretically, so that the distribution parameters must be obtained from experimental measurements. Therefore, an experimental methodology to measure them is proposed and then illustrated for a specific case. The key results of this chapter can be found in Chapter 8 in Section 8.1.3.

Chapter 8

Conclusion

The manufacturing of glass fibers is a complex energy-intensive industrial process that involves fluid and solid dynamics, heat transfer, rheology, chemistry, material science, fracture mechanics... Despite a long practical experience in producing glass fibers, the underlying physics of fiber drawing is still poorly understood. This partly explains why the industrial process has not evolved much during the past decades. There is thus a large potential for improving its efficiency. In particular, reducing the rate of fiber breaks during the drawing process represents one of the main lever for decreasing costs and increasing production throughput.

The overall goal of this research was thus to provide a quantitative understanding of the detailed physics at play, which can then be leveraged for improving the fiber drawing process. As the problem is extremely complex, the scope of this thesis was restricted to a single fiber and to the "liquid" region between the bushing plate and glass transition. Specifically, the main objectives were *i)* to extend the current understanding of the physics involved in the glass fiber drawing process and the fiber break, *ii)* to provide a physical model for the drawing of a single fiber that includes all relevant physics, *iii)* to leverage numerical solutions of this model to suggest strategies for improving the process, and *iv)* to derive a probabilistic model of the break rate that uses inputs from the physical model. The methodology has relied on a combined theoretical, computational and experimental approach. This has included the development of mathematical models, the numerical resolution of these models, and experimental measurements on a dedicated fiberization unit. Simulation results were analyzed to assess the impact of different levels of modeling fidelity and of model parameters and material properties on predictions. The analysis was then extended to assessing the influence of the operating conditions in order to identify new strategies for improving the process efficiency. Finally, a first probabilistic break rate model that exploits these physical models has been proposed.

This chapter first summarizes the key results and discusses their limitations and their

implications for the industrial manufacturing process of glass fibers. It then highlights the main contributions of this thesis, before suggesting several avenues for future work.

8.1 Key results and conclusions

Despite several assumptions and simplifications, this work has provided important results and new findings. The use of different levels of modeling fidelity has allowed to evaluate the relative importance of different physical processes and to isolate the most relevant ones. This knowledge could then be used to analyze the process operating window and identify the corresponding implications for the industrial process. Finally, the physical models have been exploited to obtain a probabilistic description of the break rate.

8.1.1 Physics and modeling of the process

A two-dimensional axisymmetric model that attempts to integrate all relevant physics has been developed in Chapter 2 and measurements for a single fiber have been performed on a dedicated experimental facility as described in Chapter 3. Comparison between the model predictions and these experimental measurements and other measurements from the literature has shown that the radius attenuation is well predicted by the opaque two-dimensional model (Chapter 5). It is however important to emphasize that this result provides only a partial validation, as the measurement uncertainties are relatively large and radius attenuation represents only an indirect quantity. A full validation would require temperature and stress measurements, but such measurements would be extremely difficult to perform, if at all possible.

In Chapter 5, the relative contribution of different forces has been analyzed by individually turning them off in the two-dimensional model. It has been found that the viscous effects, and to some extent surface tension, are much more important than inertia, gravity and air drag. On the other hand, the radial variations are small compared to axial gradients so that the problem is mostly one-dimensional. This provides support to the one-dimensional semi-analytical model derived in Chapter 2. Although this simplified model only accounts for viscous forces and neglects surface tension, inertia, gravity and air drag, it represents a good approximation to the more complex two-dimensional model with a much lower computational cost. It also leads to a more intuitive interpretation of the physics as it explicitly reveals the links between several physical quantities.

Because of the high temperature of the melt and the strong dependence of the viscosity on temperature, heat transfer by conduction, convection and radiation is critical. Overall, it was found that the axial stress and velocity grow first slowly and then rapidly increase

before reaching a plateau upstream of the transition point. On the other hand, the temperature decreases continuously along the fiber. The cooling rate, through the changes in viscosity with temperature, is the most important quantity that controls the axial stress profile and its final value, as explicitly highlighted by the one-dimensional model. The fiber cooling is dominated by radiation in the vicinity of the tip while convection becomes the main heat transfer mode further downstream (see Chapter 5). The one-dimensional model has also highlighted that the region of lower viscosity, i.e., of higher temperature, close to the tip is the most critical in regards to the final axial stress, as it contributes most to the fluidity. Additionally, a more rapid cooling in this region was found to increase the final axial stress and conversely (see Chapter 6). This implies that the region close to the tip is key to control the process.

As the melt is a semi-transparent medium, not only conduction but also internal radiation contributes to heat transfer within the fiber. A semi-transparent model has thus been developed considering only the absorption and emission mechanisms (i.e. neglecting the scattering) in Chapter 2 and then compared to a grey opaque radiative model in Chapter 5. The results have shown that the spectral dependence of the radiative properties is negligible and thus, the grey approximation is still valid. On the other hand, the main impact of internal radiation is to modify the cooling rate. Consequently, the effect of internal radiation could be approximated using an opaque radiative model with an effective emissivity that takes into account the diameter and the temperature of the fiber. Such a model provides good results and allows a large reduction in model complexity and computational cost because it does not require solving the radiation transport equations within the fiber. However, it is important to recall that external radiation assumed a blackbody surrounding at uniform temperature and did not account for the presence of the bushing plate, potential finshields or other fibers in the case of a multi-fiber bushing.

Following the literature, convective heat transfer at the fiber surface was modeled with an empirical correlation (see Chapter 2). However, the use of this correlation is questionable, especially in regards to the non-uniform temperature distribution of the entrained surrounding air observed in practice. The comparison of the cooling rate predicted by this correlation using several constant and an axially-varying surrounding air temperatures has shown that this non-uniformity is important. This result was further emphasized by simulations of the ambient air flow coupled to the fiber physical model that have demonstrated a large discrepancy compared to results obtained with the empirical correlation (Chapter 5). This strongly suggests that a better representation of convective cooling is critical to accurately predict the axial stress. Nonetheless, despite its higher fidelity the coupled air flow model suffers several limitations. First, the assumption of a fully turbulent flow everywhere is questionable. Then, it does not account for the potential presence of an

air conditioning system (HVAC), which is used in production and known to have a major impact on the process. Finally, in the case of a multi-fiber bushing, the presence of other fibers would significantly modify the airflow and should therefore be considered.

Because of the high temperatures, material properties are generally challenging to measure. Moreover, they usually depend on the temperature. Therefore, they represent a major source of uncertainty. The impact of these uncertainties has been assessed in Chapter 6 through sensitivity analysis and was found to amount to less than a few percent. Moreover, the error made by neglecting the temperature dependence of these material properties (except for the viscosity) was shown to be in general smaller than the measurement uncertainties themselves (Chapter 5). Conductivity, surface tension and density could thus be approximated as constant over the range of temperature considered. Furthermore, the use of the physically more accurate MYEGA viscosity law did not improve the results compared to those obtained with the empirical Fulcher law (Chapter 5).

8.1.2 Implications for the industrial manufacturing process

The one-dimensional model has been leveraged in Chapter 6 to investigate the operating window of the process, using the axial stress as an indicator of its robustness. Although this simplified model does not provide fully accurate quantitative predictions, it yields the correct trends. First, the impact of the cooling rate variability, process parameters and glass composition on the stress has been studied for a single fiber, highlighting the importance of the radiative cooling close to the tip and the larger final stress induced by a rapid cooling. In a second step, the impact of temperature inhomogeneity at the bushing plate has been evaluated. It has been found that even a rather narrow distribution of tip temperatures leads to a large distribution of stress, which emphasizes the importance of upstream processes at the bushing. Overall, this analysis has shown that the stress can be minimized through several levers:

Glass composition The temperature-dependence of the viscosity, the surface tension and radiative properties have been demonstrated as the most critical properties. Their impact could potentially be controlled by modifying the chemical composition of the glass.

Bushing process For a given target fiber radius, one could increase the tip temperature while increasing the drawing velocity and flow rate at constant tip radius. The radiative cooling could also be reduced through radiative interaction with the process equipment (e.g., finshields).

Bushing design For a given target fiber radius and flow rate, the tip diameter could

be decreased in conjunction with an increase of the tip temperature during the process manufacturing. In addition, the bushing design could be optimized to reduce temperature inhomogeneities at the bushing plate.

Some of these strategies are however limited by several constraints, such as, for instance, the drawing instability that occurs when the tip temperature becomes too high. The drawing instability has been studied in Chapter 6. A simplified stability map has been constructed by analyzing the time response of the fiber radius to initial temperature perturbations using simulations of the unsteady two-dimensional axisymmetric model. The drawing instability represents a major limit to operating at higher tip temperature. A possible strategy to avoid it could be to decrease the surface tension and/or to increase the convective cooling.

Finally, these conclusions should be taken with great care as Chapter 7 has shown that the strength possibly increases with increasing drawing stress. If the strength is indeed directly and explicitly dependent on the stress, then reducing the stress would not necessarily be the best strategy for improving the drawing process. A better understanding of the break is thus required before defining an optimal strategy.

8.1.3 Probabilistic modeling of the break rate

The aforementioned results have suggested different avenues for reducing the axial stress within the fiber. However, as just mentioned, seeking a lower stress level, although intuitively sensible, might not be the best strategy for reducing the break rate. The final contribution of this thesis, discussed in Chapter 7, is thus a first attempt to quantify the link between stress and strength. In particular, a probabilistic model has been derived to relate the stress to the break rate for endogenous breaks. Based on the weakest-link theory, it models the strength as a random property that follows a Weibull distribution, while the stress itself is deterministic and obtained from the physical model. The main model assumption is that the strength does not depend on the drawing conditions that only enter the model through the stress. The model requires the calibration of two constants related to the Weibull distribution. An experimental methodology has then been proposed for calibrating these model constants. It consists in break tests performed on the fiberization unit. In order to shorten the experiments, the drawing velocity has been linearly increased until a break occurs. Preliminary results support the assumption that the strength follows a Weibull distribution for fixed drawing conditions, despite some outliers observed at low drawing velocity, i.e., at low stress level. Although a definite explanation for these outliers still lacks, it is believed that external factors could be the origin of these breaks, i.e., they were exogenous breaks. On the other hand, additional measurements at a different

tip temperature have demonstrated that the measured strength distribution depends on the drawing conditions, possibly reflecting the known dependence of the strength of solid glass fibers on the drawing stress. This result contradicts the main assumption of the model. As a consequence, the model parameters cannot be considered as constant and universal. A possible approach to integrate into the model this strength dependence on drawing conditions would be to consider Weibull parameters that explicitly depend on these conditions. Nonetheless, this could potentially significantly reduce the generality of the break model. The main challenge in modeling this dependence stems from the limited fundamental physical understanding of the fiber strength and on which parameters it explicitly depends. It is important to emphasize that this model and its calibration is only a very preliminary attempt at predicting the break rate and much more work remains to do. However, a major consequence of these results, if they are definitely confirmed, is that a strategy aiming at simply reducing the drawing stress within the fiber might not be the best approach to optimize the process.

8.2 Summary of the main contributions

Although many questions remain open, this work has confirmed several results from the literature and provided important new findings towards a better understanding of the overall fiber drawing process and the fiber break. In particular, the main contributions of this thesis are:

- the development of a full axisymmetric viscous model that integrates most of the important physics of the fiber drawing process between the tip at the bushing plate and the glass transition point,
- the derivation of a semi-analytical model that has a low computational cost while retaining the important features of the physics, and that provides an intuitive interpretation of the results,
- the quantitative evaluation of the impact of numerous parameters and an exhaustive discussion of the limits of the models,
- the implementation and the quantitative assessment of a full semi-transparent internal radiation model,
- the simulations of the surrounding air flow coupled with the fiber simulations, and the quantitative assessment of the empirical correlation traditionally used to model the convective cooling,

- the numerical study of the unsteady response of the fiber and drawing instability,
- a set of measurement data for validation,
- an overall more detailed description of the physics of the process,
- guidelines for improving the efficiency of the industrial process,
- the derivation of a preliminary probabilistic model for predicting the break and a set of break measurements.

This improved detailed understanding of the drawing process and the tools developed within the frame of this work should serve as basis for assessing new optimization strategies either directly in the design phase of new bushing positions, or in operating existing ones.

8.3 Future work

The project has provided major advances with respect to the state-of-the-art in understanding and modeling the fiber drawing process. Nevertheless, the results presented suffer several limitations, as already highlighted, and additional effort could be devoted to further improve the proposed models. Moreover, the manufacturing of glass fibers involves many other aspects that have not been considered in this thesis but can have a significant impact on the efficiency of the overall process and the fiber break.

8.3.1 Possible further improvements of the proposed models and analysis

The current models could be further improved by including a more detailed description of several key physical processes and more extensive experimental measurements, as described below.

Radiative heat transfer

The assumption of a blackbody surrounding at uniform temperature could be relaxed. In particular, the temperature of the bushing plate is high and its radiation directly impacts the heat transfer at the fiber surface close to the tip, which is the most sensitive region for the stress. Similarly, the purpose of water-cooled finshieds is to modify the cooling of the fiber in this region. As sole mean of precise process control in production, they have a direct impact on the stress and the break. The contribution of the bushing plate and finshields to the radiative heat transfer could be included for instance through the use of

view factors in the definition of the boundary conditions at the fiber surface. Additionally, the spectral properties of their surface should be further investigated. Finally, the spectral model for the internal radiation could be refined, but at the expense of more complex and costly simulations.

Convective heat transfer and surrounding air flow

The coupled air flow simulations could be further improved by considering more geometrical elements that impact the air flow around the fiber. For instance, the airflow around the tips or finshields could lead to some vortex shedding. Additionally, the HVAC could also be included in such simulations as it directly controls the flow and properties (temperature, humidity, etc.) of the surrounding air. These simulations could also be used to investigate the heat transfer at the bushing plate, tip and finshields. However, such coupled iterative simulations are computationally very costly and the use of a correlation for convection could be in many cases beneficial. As the correlations traditionally used are not sufficiently accurate, a better correlation could be developed based on simulations of the ambient air flow for the specific case of fiber drawing. The new correlation should be able to account for the air preheating below the bushing plate, the change in radius of the fiber and the change in temperature of the surrounding air.

Material properties

Material properties represent one of the major sources of uncertainty in the models, as they are often very difficult to measure for liquid glass at high temperature. Obtaining more accurate measurements of these properties and their dependence on temperature and possibly geometry and cooling rate for different melt compositions would reduce the overall uncertainty in the model predictions.

Viscoelastic effects around transition

An important simplification of the model is the assumption that the glass melt behaves like a Newtonian fluid. While this assumption is valid at high temperature, i.e., in the initial region close to the tip, viscoelastic effects can be expected when the temperature decreases and the liquid glass approaches its transition point. In particular, it might impact the overall structure of the glass, and thus, the glass properties and the range of temperature of transition. Unfortunately, the only viscoelastic model for glass has been derived for a low cooling rate and slow deformations, which significantly differs from the typical conditions in the fiber drawing process. The main impact of this simplification is

supposed to be weak as viscoelastic effects would only be seen far downstream from the tip, but could also impact the fiber strength.

Unsteady effects

The unsteady dynamics of the process and the drawing instability have only been superficially investigated. A much more detailed analysis should consider different types of perturbations. First, different forms of temperature perturbations in terms of time evolution could be used. Then, perturbations of other quantities (e.g., flow rate, heat transfer, drawing velocity, etc.) should be considered. Additionally, possible vibrations induced by the winder or the HVAC-induced air flow should be studied. On the other hand, the one-dimensional model should be extended to account for surface tension effects and to treat unsteady cases. The unsteady analysis done with the two-dimensional problem could then be repeated with this simpler one-dimensional model. It could also serve as basis for a formal linear stability analysis in the same spirit as the analysis of the Plateau-Rayleigh instability, but incorporating heat transfer and the impact of cooling. This would provide a much better understanding of the key parameters that control the drawing instability and a more accurate estimate of their corresponding critical value.

Non-axisymmetric effects

As only a single fiber was considered, it has been intuitively assumed that this fiber is perfectly aligned along the tip axis. An axisymmetric assumption could thus be made for the model. However, a realistic bushing includes several thousand fibers that all converge towards the winder. As such, most of the fibers are aligned at an angle with respect to the vertical and to their corresponding tip. On the other hand, the presence of many other fibers alters the heat transfer. There is a radiative interaction between fibers, and the entrained air flow, and thus the convective cooling, is strongly modified. Furthermore, the air flow is in many cases not directly aligned along the fiber, especially close to the tip. A normal air velocity component can lead to a pressure and shear stress distribution that deforms the fiber. The problem is then clearly non-axisymmetric and the impact on the stress of variations around and/or of the contour of the fibers should be analyzed.

Probabilistic break model

As discussed in the previous chapter, the proposed probabilistic break model is only very preliminary and much work remains to do, not only with respect to modeling, but also and foremost in the understanding of the fundamental physics involved. First, the characterization of the strength should be more detailed. In particular, its dependence on external

factors such as the melting conditions, the process parameters including environmental conditions, the glass composition, and many others should be investigated. Then, the break rate model should be further improved to take into account these aspects. A first approach is to have calibration parameters that depend on these external factors. The question is then whether the model retains sufficient generality to be useful: if experiment-based calibration is required for each case of interest, the model looses most of its interest. The model should also be extended to account for external factors and include exogenous breaks. Additionally, one could also consider uncertainties in the stress predictions and represent the stress as another random quantity. Another avenue for future work could model the break from a different point of view, abandoning the underlying weakest-link assumption of the present model. A possible approach is to describe the phenomenon as a stochastic process and represent the break based on a first-hitting-time concept. This process could then be numerically simulated and compared to statistical measurements. Depending on the complexity of the model, an analytical description of the break rate could be derived.

Experimental validation data and break measurements

One of the main challenges of this research is the lack of experimental data to validate the models. This includes measurements of more significant quantities such as the stress and the temperature along the fiber. Such new experiments should also provide a precise characterization of the boundary conditions (e.g., surrounding air flow, geometry, temperature of the bushing plate, winder pulling force, etc.). Considering also different glass compositions and different process conditions, optimally closer to the actual conditions in production, would also be important to validate the models over a larger range of parameters. The characterization of the fiber strength also requires more experiments to identify the extrinsic strength dependence on the process conditions. On the other hand, additional data on the break itself is needed to calibrate and validate the break model. In this respect, preliminary measurements could be greatly improved. This includes among others identifying the vertical position of the break, accurately characterizing the conditions to isolate the effect of the winder speed on the stress, assessing and improving the repeatability of the experiments and quantifying the measurement errors. Finally, a dedicated research effort should focus on improving the precise methodology for both experimental break measurements and the inference of model parameters from these experiments.

8.3.2 Other research directions beyond the scope of this thesis

Several other topics have been left out of the scope of this thesis, but are expected to play an important role with respect to the efficiency of the process and the fiber break.

Wetting effects

A non-negligible wetting of the glass melt on the tip surface is typically observed. This wetting changes depending on the glass composition, the air conditions and the bushing surface material. Its impact on the stress and the break is however unknown and further research is required to better understand the underlying physics and model it.

Glass transition

The current model focuses on the region upstream of the glass transition point, but it is still not clear whether breaks occur mainly before the transition point or also during or after transition. The main challenge in modeling transition is its strong dependence on the material history in terms of deformations and temperature. As already mentioned, the fiber drawing process is characterized by a very rapid cooling and large deformations that both strongly impact the material structure and therefore the material properties after transition. A better understanding of the relation between glass structure and process conditions could help developing a more adapted viscoelastic model and shed light on the extrinsic strength. More specifically, the understanding of the break phenomenon could be further advanced by analyzing this structure using for instance fracture mechanics concepts.

Multi-fibers

This work has focused on a single fiber, but the real process involves several thousands of them, which can all interact with each other. A future research direction should thus consider the extension of the present thesis to multi-filament bushing by including aforementioned elements as non-axisymmetric effects, inter-fiber radiation heat transfer, the impact on the air flow, inhomogeneity of conditions across fibers, etc. As the current model is already computationally expensive, this extension should initially focus on the main trends by only considering a few fibers. The simulation of an entire bushing with thousand tips will probably require lower-order one-dimensional fiber models.

Entire bushing

The proposed physical model covers only the region from the tip to the transition point, and represents the entire bushing above it through an inlet boundary condition. This inlet condition has been shown to have a strong impact on the final stress. On the other hand, temperature inhomogeneity across the bushing plate induces a large distribution of stresses. It would therefore be useful to include the entire bushing into the model, i.e., to also represent the melt in the bushing upstream of the tip. Such simulations should evidently include the heat transfer processes between the bushing and the environment. A more practical approach could be to keep the two models separate, but link them explicitly through appropriate and potentially coupled boundary conditions.

Backend processes

Finally, glass fiber manufacturing also includes backend processes. These processes indirectly impact the fiber drawing process through the melt properties arriving at the bushing. As some breaks can be caused by melt inhomogeneity, a quantitative characterization of the melt would be useful. However, this opens an entire new research direction, that includes modeling the mixing and melting of the batch, and the melt flow through the furnace and the channels up to the frontend, with all corresponding heat transfer and other physical phenomena.

Bibliography

[1] Industry and market environnement of fiberglass. Technical report, 3B - The fibreglass company, 2017.

[2] K.L. Loewenstein. *The Manufacturing Technology of Continuous Glass Fibers*. Elsevier Scientific Publishing Company, New York, 1973.

[3] M. Koch and D. Lupton. Design and manufacture of bushings for glass fibre production. In *HVG-Colloquium, Glasstec*, Düsseldorf, Germany, 2006.

[4] L.R. Glicksman. *An investigation of the shape, temperature distribution and tension of a heated free jet flowing at ultra low reynolds number*. PhD thesis, Massachusetts Institute of Technology, USA, 1964.

[5] L.R. Glicksman. The dynamics of a heated free jet of variable viscosity liquid at low reynolds numbers. *Journal of Basic Engineering*, 90(3):343–354, 1968.

[6] L. R. Glicksman. The cooling of glass fibres. *Glass Technology*, 9(5):131–138, 1968.

[7] G. Manfrè. Rheology on the drawing zone in glass spinning. *Rheologica Acta*, 12(2):349–356, 1973.

[8] M. Stehle and R. Brückner. Grenzen des Glasfaserziehvorganges, Die Einschnür und Oszillationsgrenze. *Glasstechn. Ber.*, 53(5):130–139, 1980.

[9] B.P. Huynh and R.I. Tanner. Study of the non-isothermal glass fibre drawing process. *Rheologica Acta*, 22(5):482–499, 1983.

[10] Y. Y. Perng, A. Agarwal, M. Kadiramangalam, and A. Dutta. Simulation of coupled fiber glass-air flows and drawing of a single glass fiber. In *1st International Colloqium on Modelling of Glass Forming and Tempering*, Valenciennes, France, 1998.

[11] B.A. Purnode and Y. Rubin. Study of the non-isothermal glass fibre drawing process. In *8th International Congress on Glass*, San Fransisco, USA, 1998.

[12] B.A. Purnode. Transient axisymmetric study of glass fiber forming. In *Proceedings of ASME 2000 Fluids Engineering Division Summer Meeting*, Boston, USA, 2000.

[13] B.M. McKeone. Measurement of air temperatures and velocities in the fiber glass forming environment. Master's thesis, Massachusetts Institute of Technology, USA, 1999.

[14] M. Sweetland. Nozzle analysis and heat transfer model for spray cooling of glass fibers. Master's thesis, Massachusetts Institute of Technology, USA, 1998.

[15] R. Von Der Ohe. *Simulation of Glass Fiber Forming Processes.* PhD thesis, Aalborg University, Denmark, 2003.

[16] Lenoble A. *Caractérisation optique et étude de la stabilité d'un procédé de fibrage du verre.* PhD thesis, University of Provence, 2004.

[17] F. Onofri, A. Lenoble, S. Radev, and P. Guering. High resolution monitoring of an unsteady glass fibre drawing process. *Experimental Fluids*, 42:601–610, 2007.

[18] S. Rekhson and P. Sanger. Improvement of performance and yield of continuous glass fiber drawing technology. In *Proceedings of the FY 2003 Glasss*, Golden, USA, 2003.

[19] S. Rekhson, J. Leonard, and P. Sanger. Attenuation and breakage in the continuous glass fiber drawing process. *Ceram. Eng. Sci. Proc.*, 25(1):179–190, 2004.

[20] S. Rekhson. Improvement of performance and yield of continuous glass fiber drawing technology. In *Proceedings of the FY 2005 Glasss*, Chicago, USA, 2005.

[21] S. Rekhson and P. Sanger. Improvement of performance and yield of continuous glass fiber drawing technology. In *Proceedings of the FY 2004 Glasss*, Arlington, USA, 2004.

[22] S. Liu and L.E. Banta. Parametric study of glass fiber drawing process. *Int. Journal of Applied Glass Science*, 1(2):180–187, 2010.

[23] A. K. Varshneya. *Fundamentals of inorganic glass.* Academic Press, Inc., 1994.

[24] S. L. Webb and D. B. Dingwell. The Onset of Non-Newtonian Rheology of Silicate Melts - A Fiber Elongation Study. *Physics and Chemistry of Minerals*, pages 125–132, 1990.

[25] S. Narayanaswamy. A model of structural relaxation in glass. *J. Am. Ceram. Soc.*, 54(10):491–499, 1971.

[26] A. Ziabicki. *Fundamentals of Fibre Formation.* John Wiley and Sons, New York, 1976.

[27] E. Richelle, R. Tasse, and M. L. Rietmuller. Momentum and thermal boundary layer along a slender cylinder in axial flow. *International Journal of Heat and Fluid Flow*, 16:99–105, 1995.

[28] B. C. Sakiadis. Boundary-layer behavior on continuous solid surfaces: iii. the boundary-layer on a continuous cylindrical surface. *AIChE Journal*, 7:467–472, 1961.

[29] R. E. Sayles and B. Caswell. A finite element analysis of the upper jet region of a fiber drawing flow field of a temperature-sensitive material. *International Journal of Heat and Mass Transfer*, 27:57–67, 1984.

[30] S. Kubo. Boundary-layer behavior on continuous solid surfaces: iii. the boundary-layer on a continuous cylindrical surface. In *High Speed Fiber Spinning - Science and Engineering Aspects, A. Ziabicki, and H. Kawai*. Krieger Publishing Company, Malabar, FL, USA, 1991.

[31] C. Miller. Effect of filament drawdown on aerodynamic drag and heat transfer in fiber spinning. *AIChE Journal*, 50:898–905, 2004.

[32] R Beyreuther and H. Brünig. *Dynamics of Fibre Formation and Processing*. Springer, Berlin, 2007.

[33] J. L. White and Y. Ide. Instabilities and Failure in Elongational Flow and Melt Spinning of Fibers. *Journal of Applied Polymer Science*, 22:3057–3074, 1978.

[34] S. Kase and T.J. Matsuo. Studies of melt spinning i, fundamental equations on the dynamics of melt spinning. *Journal of Polymer science, Part A: General papers*, 3(7):2541–2554, 1965.

[35] N. Offermans. Study and modeling of the heat exchanges for a cooling apparatus in a fiberglass forming environment. Master's thesis, University of Liège, Belgium, 2014.

[36] C.A. Angell. Spectroscopy simulation and scattering, and the medium range order problem in glass. *Journal of Non-Crystalline Solids*, 73(1-3):1–17, 1985.

[37] I. Avramov. Viscosity activation energy. *European Journal of Glass Sciences Technology B*, 48(1):61–63, 2007.

[38] J. Schmelzer and I. Gutzow. *Glasses and the glass transition*. Wiley - VCH, 2011.

[39] Q. Zheng, J.C. Mauro, A.J. Ellison, M. Potuzak, and Y. Yue. Universality of the high-temperature viscosity limit of silicate liquids. *Phy. Rev. B*, 83(21):13–15, 2011.

[40] J.C. Mauro, Y. Yue, A.J. Ellison, P.K. Gupta, and D.C. Allan. Viscosity of glass-forming liquids. *Proc. Natl. Acad. Sci. USA*, 106(47):19780–84, 2009.

[41] G. Adam and J.H. Gibbs. On the temperature dependence of cooperative relaxation properties in glass-forming liquids. *Journal of chemical Physic*, 43(1):139–146, 1965.

[42] T. Hecksher, A.I. Nielsen, N.B. Olsen, and J.C. Dyre. Little evidence for dynamic divergences in ultraviscous molecular liquids. *Nature Physics*, 4:737–741, 2008.

[43] F.H. Stillinger. Supercooled liquids, glass transitions, and the kauzmann paradox. *Journal of Chemical Physic*, 88:7818–7825, 1988.

[44] John Mauro, Douglas Allan, and Marcel Potuzak. Nonequilibrium viscosity of glass. *Physical Review B*, 80(9):094204, 2009.

[45] L. D. Pye, A. Montenero, and I. Joseph. *Properties of Glass-Forming Melts*. Taylor and Francis, 2005.

[46] Gardon. The Emissivity of Transparent Materials. *Journal of American Ceramic Society*, 39(8):278–287, 1955.

[47] D. C. Wilcox. *Turbulence Modeling for CFD*. Anaheim: DCW Industries, 1998.

[48] N. Siedow, T. Grosan, D. Lochegnies, and E. Romero. Application of a New Method for Radiative Heat Transfer to Flat Glass Tempering. *Journal of the American Ceramic Society*, 88(8):2181–2187, 2005.

[49] B. Le Corre, L. Bau, Collin A., G. Meshaka, and G. Jeandel. Numerical simulation of glas sagging. In *23rd International Congress on Glass*, Prague, Czech republic, 2013.

[50] C. Chen and Y. Jaluria. Modeling of Radiation Heat Transfer in the Drawing of an Optical Fiber With Multilayer Structure. *Journal of Heat Transfer*, 129(3):342 – 352, 2007.

[51] M. F. Modest. *Radiative Heat Transfer*. Academic Press, Second Edition, USA, 2003.

[52] F. T. Lentes and N. Siedow. Three-dimensional radiative heat transfer in glass cooling processes. *Glastech. Ber. Glass Sciences Technology*, (72):188 – 196, 1999.

[53] A. J. Faber. Optical properties and redox state of silicate glass melts. *Comptes Rendus Chimie*, (5):1 – 8, 2002.

[54] N. Siedow, D. Lochegnies, F. Béchet, P. Moreau, H. Wakatsuki, and N. Inoue. Axisymmetric modeling of the thermal cooling, including radiation, of a circular glass disk. *International Journal of Heat and Mass Transfer*, 89:414–424, 2015.

[55] Z. Wei, K-M. Lee, and S. W. Tchikanda. Effects on Radiative Transfer Modeling on Transient Temperature Distribution in Semitransparent Glass Rod. *Journal of Heat Transfer*, 125:635–643, 2003.

[56] M. K. Choudhary, R. Venuturumilli, and M. R. Hyre. Mathematical Modeling of Flow and Heat Transfer Phenomena in Glass Melting, Delivery, and Forming Processes. *International Journal of Applied Glass Science*, 1(2):188–214, 2010.

[57] S. Rosseland. *Theoretical Astrophysics; Atomic Theory and the Analysis of Stellar Atmospheres and Envelopes*. Clarendon Press, Oxford, 1936.

[58] J. C. Richmond. Radiation of emittance to other optical properties. *Journal of research of the national bureau of standard, Sec. C*, 3(67):217 – 226, 1963.

[59] J. Canny. A computational approach to edge detection. *IEEE Transactions on Pattern Analysis and Machine Intelligence*, 8:679–698, 1986.

[60] M.J. Crochet, R. Keunings, B. Debbaut, and J.M. Marchal. Polyflow: a multipurpose finite element program for continuous polymer flows. *Computer Modeling for Extrusion and Other Continuous Polymer Processes*, pages 25–50, 1992.

[61] J. N. Reddy and D. K. Gartling. *The Finite Element Method in Heat Transfer and Fluid Dynamics, Third Edition*. Third edition edition, April 2010.

[62] O. C. Zienkiewicz, R. L. Taylor, and P. Nithiarasu. *The Finite Element Method for Fluid Dynamics*. Butterworth-Heinemann, 2013.

[63] J. Donea, Huerta A., Ponthot J-Ph, and A. Rodriguez-Ferran. *Arbitrary Lagrangian-Eulerian Methods, Encyclopedia of Computational Mechanic, Volume 1: Fundamentas, Chapter 14*. John Wiley and Sons, 2004.

[64] J. H. Ferziger and M. Peric. *Computational Methods for Fluid Dynamics*. Springer, 2002.

[65] J.H. Jeans. The equations of radiative transfer of energy. *Monthly Notices Royal Astronomical Society*, (78):28–36, 1917.

[66] H. C. Hottel and E. S. Cohen. Radiant heat exchange in a gas-filled enclosure: Allowance for nonuniformity of gas temperature. *AIChE Journal*, 4:3–14, 1958.

[67] J. A. Fleck. The calculation of nonlinear radiation transport by a Monte Carlo method: Statistical physics. *Methods in computational physics*, 1:43–65, 1961.

[68] S. Chandrasekhar. *Radiative transfer*. Dover Publications, 1960.

[69] A. S. Jamaluddin and P. J. Smith. Predicting Radiative Transfer in Axisymmetric Cylindrical Enclosures Using the Discrete Ordinates Method. *Combustion Science and Technology*, 62(4-6):173–186, 1988.

[70] J.S. Truelove. Discrete ordinate solutions of the radiation transport equation. *ASME J. Heat Transfer*, (109):1048–1051, 1987.

[71] H. Koo, R. Vaillon, V. Goutière, V. Le Dez, H. Cha, and T. Song. Comparison of three discrete ordinates methods applied to two-dimensional curved geometries. *International Journal of Thermal Sciences*, 42(4):343–359, 2003.

[72] U.A. Ozden. Numerical simulation of the tip plate temperature gradient in a glass-fiber bushing during production. In *1st International Glass Fiber Symposia*, Aachen, Germany, 2012.

[73] J. Eggers and E. Villermaux. Physics of liquid jets. *Reports on Progress in Physics*, 71(3):036601, 2008.

[74] M. A. Matovich and J. R. A. Pearson. Spinning a Molten Threadline. Steady-State Isothermal Viscous Flows. *Industrial and Engineering Chemistry Fundamentals*, 3(8):512–520, 1969.

[75] J. R. A. Pearson and M. A. Matovich. Spinning a Molten Threadline. Stability. *Industrial and Engineering Chemistry Fundamentals*, 4(8):605–609, 1969.

[76] D. Gelder. The Stability of Fiber Drawing Processes. *Industrial and Engineering Chemistry Fundamentals*, 3(10):534–535, 1971.

[77] Y. T. Shah and J. R. A. Pearson. On the Stability of Nonisothermal Fiber Spinning - General Case. *Industrial and Engineering Chemistry Fundamentals*, 11(2):150–153, 1972.

[78] Y. T. Shah and J. R. A. Pearson. On the Stability of Nonisothermal Fiber Spinning. *Industrial and Engineering Chemistry Fundamentals*, 11(2):145–149, 1972.

[79] G. K. Gupta, W. W. Schultz, E. M. Arruda, and X. Lu. Nonisothermal model of glass fiber drawing stability. *Rheologica Acta*, 35(6):584–596, 1996.

[80] M. Bechert, D. W. Schubert, and B. Scheid. On the stabilizing effects of neck-in, gravity, and inertia in newtonian film casting. *Physics of Fluids*, 28:024109, 2016.

[81] M. D. Lund and Y. Yue. Impact of Drawing Stress on the Tensile Strength of Oxide Glass Fibers. *Journal of the American Ceramic Society*, 93(10):3236–3243, 2010.

[82] C. R. Kurkjian, P. K. Gupta, and R. K. Brow. The Strength of Silicate Glasses: What Do We Know, What Do We Need to Know? *International Journal of Applied Glass Science*, 1(1):27–37, 2010.

[83] M. L. Korwin Edson, D. A. Hofmann, and P. B. McGinnis. Strength of High Performance Glass Reinforcement Fiber. *International Journal of Applied Glass Science*, 3(2):107–121, 2012.

[84] W. H Otto. Relationship of Tensile Strength of Glass Fibers to Diameter. *Journal of The American Ceramic society*, 38(3):122–125, 1955.

[85] W. F. Thomas. An investigation of the factors likely to affect the strength and properties of glass fibres. *Physics and chemistry of glasses*, 1(1), 1960.

[86] Min Ya, Joachim Deubener, and Yuanzheng Yue. Enthalpy and Anisotropy Relaxation of Glass Fibers. *Journal of the American Ceramic Society*, 91(3):745–752, March 2008.

[87] R. A. Fisher and L.H.C. Tippett. Limiting forms of the frequency distribution for reliability of the largest and smallest member of a sample. *Proceedings of the Cambridge Philosophical Society*, 24:180–190, 1928.

[88] P. K. Gupta. *Strength of glass fibers, Fiber fracture*. Elsevier Science, 2002.

[89] S. Klenkenberg and Q. Chouffart. Breakage Rate. Technical report, 3B - The fibreglass company, 2016.

[90] C. Ruwet. Processus de poisson. Master's thesis, University of Liege, Belgium, 2007.

[91] L. H. Crow. Reliability analysis for complex, repairable systems. Technical report, Tech. report, U.S., Army materiel systems analysis, 1975.

[92] H. Rinne. *The Weibull distribution: A handbook*. CRC Press, 2008.

[93] A. Khalili and K. Kromp. Statistical properties of weibull estimators. *Journal of Materials Science*, 26(24):6741–6752, 1991.

[94] K. Boudt, D. Caliskan, and C. Croux. Robust explicit estimators of weibull parameters. *Metrika*, 73(2):187–209, 2011.